Thermodynamics for practical kesterite photovoltaics

Jackson, Adam

Award date:
2016

Awarding institution:
University of Bath

Thermodynamics for practical kesterite photovoltaics

Adam James Jackson

A thesis submitted for the degree of Doctor of Philosophy

University of Bath
Department of Chemistry

February 2016

Contents

List of Figures

List of Tables

Acknowledgements

Firstly I must thank my lovely wife Tamsin. Wedding-planning was a helpful diversion at times, but more important have been her contributions to my self-esteem, well-being and general sanity. Her dedicated proof-reading has also been invaluable. My other close family, housemates and bandmates have also been a good source of encouragement, support and distraction. I may not always show it, but I really do appreciate it.

Admittedly my sample set is limited, but it is difficult to see a way in which Prof. Walsh could have been a better lead supervisor; his willingness to invest time and resources into his students and trust that we will live up to his expectations without any micromanagement is extraordinarily motivating, if occasionally exhausting. My supporting supervisors Darrell Patterson and Laurie Peter have been available and encouraging. I have faith that Darrell's support would have been invaluable had things gone less well than they have. Laurie has kept me embedded in the UK kesterites scene, and has always made things feel part of a larger whole.

Post-graduate students are regarded as less sociable than undergraduates, yet I have not lacked company in the last few years. The Doctoral Training Centre in Sustainable Chemical Technologies has a lot to do with it, and I feel fortunate to have such a talented cohort of peers as well as support from the directors. No administrative question was too daft or problem too irritating for Sheila Apps or Deborah Demathieu; I have no way of knowing how much they have streamlined my experience but suspect that my gratitude is deserved. The other members of the Walsh Materials Design group have been fantastic — in particular Lee Burton, Keith Butler and Jarvist Frost have been patient and supportive. I would also like to acknowledge here the help of David Tompsett; for much of the year preceding my PhD work we shared an office with Lee Burton and a few other students, and he cheerfully assisted my attempts to understand *ab initio* calculations.

During these studies I have also had the privilege of meeting many inspiring PhD students from other universities, and especially note Suhyun Yoo of Yonsei University and Mirjana Dimitrievska of IREC. Our PVTEAM partners have been lovely and Devendra Tiwari's formidable memory for relevant papers has been useful on more than one occasion. The European kesterites research community is passionate and friendly, and I would thank the organisers of the three European Kesterite Workshops I have attended for facilitating an invaluable opportunity for researchers in this field. In particular, Jonathan Scragg, Philip Dale and Susan Schorr have given me their time for useful discussions at multiple conferences.

This project was funded by EPSRC through the Doctoral Training Centre in Sustainable Chemical Technologies (grant no. EP/G03768X/1). It has also relied on high-performance computing (HPC) resources totalling over 1.3 Mcore h. About a third of this was on Blue Joule, an IBM Bluegene/Q system based in the Hartree Centre. The STFC Hartree Centre is a research collaboratory in association with IBM, providing HPC platforms funded by the UK's investment in e-Infrastructure. Due to the architecture of Bluegene/Q systems (low clock speed, many cores), a "core hour" on Blue Joule represents less computational work than a core hour on a more conventional machine — and substantially less energy consumption. The main workhorses have been HECToR and ARCHER, two generations of the UK's national HPC service based at

the University of Edinburgh, accessed via our membership of the UK's HPC Materials Chemistry Consortium, which is funded by EPSRC (grant no. EP/L000202). Some important calculations have made use of the University of Bath's own HPC facilities Aquila and Balena, which have been very serviceable for medium-scale jobs using ~ 100 cores. The remaining computational work was performed using the Walsh Materials Design group system Neon and various Intel-based workstations. For the sake of future amusement I also note here that the majority of the analysis work was performed on the faithful "Nitrogen", a quad-core Sandy Bridge iMac clocked at 2.8 GHz with 12 GB of RAM. Compiling this document took about 10 s, extending to several minutes if all the plots were regenerated.

The production of this thesis and the data analysis involved has relied heavily on open-source software. I am indebted to the work of the Free Software Foundation and the many people who have contributed to the wider Free Software ecosystem, but acknowledge here a few projects that have been particularly critical for this work. The thesis has been typeset with pdfLaTeX, which draws together TeX, LaTeX and pdfTeX, projects initialised by Donald Knuth, Leslie Lamport and Hàn Thế Thành respectively. Data analysis and plotting use Python 2.7 with the Numpy, Scipy and Matplotlib extension projects. Ternary phase diagrams have been built on top of a small Matplotlib extension developed by Richard Otis as part of the Pycalphad project. Prototyping, note-taking and experimentation have benefited greatly from the IPython Notebook (now "Jupyter") with the IPython interpreter. The Atomic Simulation Environment project has prevented a great deal of redundant scripting. The vast majority of work on this project has in some way involved Richard Stallman's GNU Emacs, often with Carsten Dominik's remarkably ambitious *org-mode* extension; spending the required number of hours per day in front of a computer for three years would have been far less appealing if not for their work.

Declaration of material from a previously submitted thesis and of work done in conjunction with others

A flowchart describing DFT optimisations was developed for a previous report which was submitted towards my degree of MRes in Sustainable Chemical Technologies. The figure was subsequently reproduced (with my permission) in the PhD theses of Lee A. Burton and Christopher H. Hendon. A modified version of the flowchart is used in this thesis as Fig. 4.3 on page 65; the main change has been to combine the optimisation of atomic positions and lattice parameters, reflecting the operation of typical quantum chemistry codes.

Thermochemical derivations for the *ab initio* study of systems containing solids and gases were included in a previous report which was submitted towards obtaining my MRes degree in Sustainable Chemical Technologies. This formalism is built on the work of others and has been slightly rearranged for usage in two academic papers, an internal report and this thesis; ultimately, this is my preferred mathematical description of the methodology employed and the scope for variation is limited.

Sulfur allotrope modelling includes results from genetic algorithm calculations which were carried out by Davide Tiana.

Vibrational mode assignment was carried out by Mirjana Dimitrievska based on my calculated eigenvectors. Mirjana also originally proposed the visualisation of eigenmodes as a useful approach for studying Raman data.

Abstract

Copper zinc tin sulfide (CZTS) is a photovoltaic absorber material used in thin-film devices. Research into the kesterite absorbers $Cu_2ZnSn(S_{1-x}Se_x)_4$ has been particularly active in the last decade: this is motivated by the abundance of the constituent elements, which presents a long-term advantage over existing thin-film technologies including CIGS and CdTe. However, the efficiency of CZTS-based devices has been lower than expected and among other factors this is attributed to is the presence of secondary phases. In this thesis, a novel thermochemical model is developed for the mixed sulfur vapour phase that is present during the annealing of CZTS films. Temperature and pressure-dependent phase diagrams are then constructed for the Cu-Zn-Sn-S system from first-principles calculations within density-functional theory. While research-grade CZTS is produced in both low and high-pressure processes, it is found that the phase diagram is similar in both regimes except for the oxidation state of tin sulfide. The dominant ternary phase, of those modelled, is a monoclinic phase of Cu_2SnS_3. A small temperature/pressure envelope appears to exist in which this phase is unstable relative to CZTS and the binary phases. This potentially offers a route to copper-rich CZTS without the presence of ternary phases. Rapid, high-temperature annealing for industrial deployment appears to be feasible without decomposition of the kesterite, provided that an adequately high system pressure is maintained. This work demonstrates that with high-performance computing it is possible to explore the thermodynamic space around a quaternary compound before traditional thermochemical data has been obtained. The methodology developed here is applicable to other multi-component systems.

Publications

The following scientific papers were published over the course of the PhD studies. Publications [4], [6] and [9] contain results used in this thesis, while [5] includes work which emerged from the main investigation but was ultimately not used.

[1] A. Walsh, J. Buckeridge, C. R. A. Catlow, A. J. Jackson, T. W. Keal, M. Miskufova, P. Sherwood, S. A. Shevlin, M. B. Watkins, S. M. Woodley and A. A. Sokol, Limits to doping of wide band gap semiconductors, *Chem. Mater.*, 2013, **25**, 2924–2926.

[2] R. A. Lunt, A. J. Jackson and A. Walsh, Dielectric response of Fe_2O_3 crystals and thin films, *Chem. Phys. Lett.*, 2013, **586**, 67–69.

[3] A. J. Jackson and A. Walsh, Oxidation of GaN: An ab initio thermodynamic approach, *Phys. Rev. B*, 2013, **88**, 165201.

[4] A. J. Jackson and A. Walsh, Ab initio thermodynamic model of Cu_2ZnSnS_4, *J. Mater. Chem. A*, 2014, **2**, 7829.

[5] A. J. Jackson, J. M. Skelton, C. H. Hendon, K. T. Butler and A. Walsh, Crystal structure optimisation using an auxiliary equation of state, *J. Chem. Phys.*, 2015, **143**, 184101.

[6] J. M. Skelton, A. J. Jackson, M. Dimitrievska, S. K. Wallace and A. Walsh, Vibrational spectra and lattice thermal conductivity of kesterite-structured Cu_2ZnSnS_4 and $Cu_2ZnSnSe_4$, *APL Mater.*, 2015, **3**, 041102.

[7] F. Brivio, J. M. Frost, J. M. Skelton, A. J. Jackson, O. J. Weber, M. T. Weller, A. R. Goni, A. M. A. Leguy, P. R. F. Barnes and A. Walsh, Lattice dynamics and vibrational spectra of the orthorhombic, tetragonal, and cubic phases of methylammonium lead iodide, *Phys. Rev. B*, 2015, **92**, 144308.

[8] M. Dimitrievska, H. Xie, A. J. Jackson, X. Fontané, M. Espíndola-Rodríguez, E. Saucedo, A. Pérez-Rodríguez, A. Walsh and V. Izquierdo-Roca, Resonant Raman scattering of ZnS_xSe_{1-x} solid solutions: the role of S and Se electronic states, *Phys. Chem. Chem. Phys.*, 2015, **18**, 7632–7640.

[9] A. J. Jackson, D. Tiana and A. Walsh, A universal chemical potential for sulfur vapours, *Chem. Sci.*, 2016, **7**, 1082–1092.

Notation and symbols

This work draws on concepts in physics, chemistry, engineering and mathematics. Within these fields notation is somewhat inconsistent, and between them there are many clashes. A single notation system is used which draws primarily on engineering and chemistry. A few details are worth noting here:

- Vectors are indicated with **bold** symbols.
- A superscript zero is used to indicate absolute zero temperature and pressure where appropriate, such that $H_i^0 = H_i(T = 0, p_i = 0)$. A superscipt 'plimsoll' ($^{\ominus}$) is used to indicate a non-zero reference state; conventionally this means "standard temperature and pressure", i.e. $H_i^{\ominus} = H_i(T = 298.15\,\mathrm{K}, p_i = 1 \times 10^5\,\mathrm{Pa})$, but this is not mathematically required unless indicated.
- The circumflex $\hat{}$ represents a 'specific' property — an extensive property which is scaled to the quantity of material involved, giving an intensive property. For example, if H denotes the total enthalpy of a finite system, $\hat{H}$ denotes the enthalpy of one unit (typically one mole) of that one system. Likewise, $\hat{V}$ might denote molar volume and $\hat{C}_p$ a molar heat capacity. These variants are not listed in this section and may be considered to exist for all extensive properties. Properties which are always intensive, such as temperature T and chemical potential μ, do not need a circumflex. In some fields the circumflex is commonly used to denote an operator; to avoid such a clash, operators in this work are denoted with a calligraphic script. For example, $\mathscr{H}$ represents the Hamiltonian operator. An exception is the Lagrangian $\mathscr{L}$, which is a function, but is also conventionally denoted with a calligraphic script.
- "Bandgap" is preferred to "band gap" or "band-gap"; while admittedly clumsy on its own, it is required for the compact and unambiguous "wide-bandgap semiconductor".
- A few pieces of standard set-theory notation are used:

$x \in A$	x is a member of the set A
$x \subset A$	x is a proper subset of the set A
$\mathbb{Z}$	The set of all integers $\ldots, -2, -1, 0, 1, 2, \ldots$

- The Hermann-Mauguin notation is used to identify the symmetry of space groups. For example, the kesterite space group $I\bar{4}$ is a body-centered lattice (I) with 4-fold improper rotational symmetry ($\bar{4}$). The Schoenflies notation is used for point groups. For example the ground state of S_4 has C_{2v} symmetry, which consists of a 2-fold rotational axis and two mirror planes.

ASSUMPTION

- Key assumptions and approximations are shown in shaded boxes.
- Approximations in shaded boxes are assumed to be valid.

List of symbols

A	Helmholtz free energy
C_p	Heat capacity at constant pressure $\left(\frac{\partial H}{\partial T}\right)_P$
C_v	Heat capacity at constant volume $\left(\frac{\partial U}{\partial T}\right)_v$
E	Energy of a system
E_0	Ground-state energy
F	Force
G	Gibbs free energy
H	Enthalpy
h	Planck constant $\sim 6.63 \times 10^{-34}\,\mathrm{J\,s}$
$\hbar$	Reduced Planck constant $\frac{h}{2\pi}$
$\mathbf{k}$	Wave vector associated with periodic electronic structure
k_B	Boltzmann constant $\sim 1.38 \times 10^{-23}\,\mathrm{J\,K^{-1}}$
m	Mass
n_i	Quantity of i (e.g. in mol)
P	Total/system pressure
p_i	Partial pressure of component i
$\mathbf{q}$	Wave vector associated with lattice vibrations
Q	Partition function of a system
q	Partition function of some element (e.g. a molecule)
$\mathbf{R}$	Bravais lattice points
$\mathbf{r}$	Position vector
r_{Bohr}	Bohr radius (a fundamental constant, $r_{\mathrm{Bohr}} \approx 0.53\,\text{Å}$)
S	Entropy
t	Time
V	Volume
V_{OC}	Open-circuit voltage; potential difference across device when no current is drawn.
Γ	Label given to wave vector at the origin of reciprocal lattice (i.e. $\mathbf{k}$ or $\mathbf{q} = (0,0,0)$)
$\delta_{i,j}$	Kronecker delta function: $\delta_{i,j} = \begin{cases} 1, & \text{if } i = j \\ 0, & \text{otherwise} \end{cases}$
ϵ	Energy of a state
Λ	Thermal de Broglie wavelength $\Lambda = \sqrt{\frac{2\pi\hbar^2}{mk_BT}}$
$\boldsymbol{\lambda}$	Vector of Lagrangian multipliers λ_i (parameters used in solution of constrained minimisation problem)
μ	Chemical potential (change in Gibbs free energy with quantity, $\left(\frac{\partial G}{\partial n_i}\right)_{n_{j\neq i},T,P}$)

ν	(Vibrational) frequency
ρ	(Electron) density
σ	Rotational symmetry number (i.e. number of equivalent structures by rotation)
$\mathbf{\Phi}$	Matrix of one-electron wavefunctions described using a basis set
ϕ	One-electron wavefunction, approximately described using a basis set
Ψ	Wavefunction of whole (possibly many-electron) system
ψ	One-electron wavefunction
ω	Angular frequency ($\omega = 2\pi\nu$)
$\mathscr{H}$	Hamiltonian operator
$\mathscr{h}$	One-electron Hamiltonian operator
$\mathscr{L}$	Lagrangian function (for constrained optimisation)
$\mathscr{U}$	Potential energy operator (component of Hamiltonian $\mathscr{H}$)

List of abbreviations

B3LYP 3-parameter hybrid exchange-correlation functional. p. 60

BFGS Broyden-Fletcher-Goldfarb-Shanno algorithm, a quasi-Newtonian method for optimisation problems.

CZTS Copper zinc tin sulfide (any phase/composition)

CZTSe Copper zinc tin selenide (any phase/composition)

CZTSSe Copper zinc tin sulfide/selenide alloy (any phase/composition)

CTS Copper tin sulfide (any phase/composition)

DFT Density-functional theory

DOS Density of states

FU Formula units (i.e. unit of a compound as given in its conventional formula. One FU of water consists of two H atoms and one O atom.)

GGA Generalised gradient approximation; commonly used to label DFT functionals formed under this approximation. p. 59

HF Hartree–Fock; wavefunction-based *ab initio* calculation method with exact exchange and no electron correlation.

HSE Heyd–Scuseria–Ernzerhof screened hybrid DFT functional. HSE06 refers the the recommended implementation, with the screening parameter $\omega = 0.11\, {r_{\mathrm{Bohr}}}^{-1}$. p. 60

LDA, LSDA Local (spin-)density approximation; commonly used to label DFT functionals formed under this approximation.

PBE, PBEsol Perdew–Burke–Ernzerhof parameter-free XC-functionals; PBEsol restores the density gradient expansion and is recommended for solids. p. 59

PBE0 Single-parameter hybrid exchange correlation functional based on PBE. p. 60

PV Photovoltaics (or “photovoltaic” where used as an adjective).

SCF Self-consistent field; iterative method used to solve electronic structure in DFT and HF calculations.

VWN Vosko–Wilk–Nusair parameterisation of ideal electron gas (jellium) calculations for use in XC functionals. p. 59

XC Exchange-correlation (i.e. taking account of both electron exchange and correlation effects)

XRD X-ray diffraction

Part I

Introduction

Chapter 1

Motivation

1.1 The energy crisis

The scope of human achievement is such that we are able to substantially rearrange and impact the world around us. Over the last few centuries this has led to remarkable achievements in terms of increased lifespans and comfort levels. The use of automation has not led to increased leisure time as predicted by the likes of Keynes;[1] instead competition has driven people to be increasingly ambitious with their activity. There have been clear social benefits to this such as increasingly equal gender representation in the workplace. In addition, the remarkable progress in the arts and fundamental sciences suggests that humanity's creativity has not been too restricted.

This industrial progress has primarily been driven by the consumption of non-renewable resources, and is associated with long-term environmental changes including loss of biodiversity,[2] the production (and mandated curation) of radioactive waste[3] and, most threateningly, elevated levels of greenhouse gases in the atmosphere.

There is a biological imperative to act in the long-term interest of humanity, and concern that industrialised society was under-performing in this regard became prominent in the 1970s and 1980s. Following an urgent call by the United Nations, a thoughtful consensus was expressed through the publication of *Our Common Future* by the World Commission of Environment and Development in 1987.[4] This work formalised the principle of "sustainable development":

> Humanity has the ability to make development sustainable to ensure that it meets the needs of the present without compromising the ability of future generations to meet their own needs. The concept of sustainable development does imply limits – not absolute limits but limitations imposed by the present state of technology and social organization on environmental resources and by the ability of the biosphere to absorb the effects of human activities. But technology and social organization can be both managed and improved to make way for a new era of economic growth. The Commission believes that widespread poverty is no longer inevitable. Poverty is not only an evil in itself, but sustainable development requires meeting the basic needs of all and extending to all the opportunity to fulfil their aspirations for a better life. A world in which poverty is endemic will always be prone to ecological and other catastrophes.

This principle has held up well over time, suggesting an obligation to improve quality of life for all while recognising the danger in trying to achieve this improvement too quickly. In practice sustainable development is widely held to have three aspects: ecology, society and economy. These "pillars" are occasionally misrepresented; many businesses appear to believe that economic sustainability is satisfied by the health of their own accounts, disregarding their

impact on the global economy.

One pressing "need of the present" is energy in the form of fuels, electricity and reactive feedstocks for industrial processes. This demand is expected to continue increasing, driven by population growth and improved standards of living in the developing world. The correlation between energy usage and standard of living (as quantified by Human Development Index) is interesting; an analysis based on 1997 figures concluded that 4000 kW h is required *per capita* for the highest levels of Human Development.[5] There is statistical evidence that energy consumption can cause economic growth, rather than *vice versa*, but also that this varies from country to country and applies more to the developed world than the developing world.[6] Restricting the energy usage of developing economies is politically difficult as it risks undermining social development.

Interest in electrification appears to be growing in areas traditionally dominated by fossil fuels; for example, the UK Department of Energy and Climate Change supports the usage of electric ground-source heat pumps as a way of de-carbonising domestic heating.[7] Electric vehicles have inherently simple mechanical designs and a low fire risk compared to combustion engines; the main barriers to adoption are cost and range anxiety, which can both be addressed by capital investment. While the efficiency savings are attractive, the great promise of electrification is to reduce our dependence on fossil fuels.

The uncertain supply and volatile prices of fossil fuels are seen as an incentive to move to renewable energy sources. This is comforting as it suggests that "peak oil" will lead free-market economies to adopt renewable energy on an appropriate timescale. However, if we intend to develop sustainably then this is a dangerous irrelevance; the same market factors will drive us to use more fossil fuels when they are abundant. Greenhouse-gas-driven climate change presents an existential threat to our way of life.[8–10] While attempts have been made to assign specific economic and human costs, the basic injustice and epic scale of its effects in both time and distance leave existing legal and economic systems poorly equipped to incentivise optimal behaviour.[11] *Limits to Growth* (1972) was an influential early study of possible outcomes, using mathematical models of systems containing positive and negative feedback loops.[12] The authors found that in many scenarios there was an "overshoot" effect where, following the reduction of emissions, the environment would stabilise in a different state from its initial equilibrium. The degree of overshoot is related to the speed and extent of changes which are made. Revisiting their work in subsequent decades the authors found that their predictions matched climate data more closely than expected, and there is evidence that we are already in a state of overshoot.[13]

The main legislative response to this threat has been to develop international treaties with binding targets and economic penalties; in order to meet these targets states have invested heavily in low-carbon technologies, alternative energy sources and "offsetting" schemes. Fossil fuel production has continued as normal, with the forecasts of major petrochemical companies suggesting that they do not expect climate concerns to truly disrupt to their core business in the coming decades.[14;15] The corresponding scenarios in *Limits to growth* are not optimistic.

1.2 The case for earth-abundant photovoltaics

Solar energy in general possesses several desirable attributes. It cannot be depleted: the Sun is expected to change gradually on a scale of 100–1000 million years, while human history covers a period of the order 10–100 thousand years. More importantly, there is no inherent link between solar energy and atmospheric pollution, although the impact of production and deployment must be considered. The theoretical power available for capture, which is around 120 000 TW, dwarfs human consumption of the order 15–20 TW.[16]

Progress appears to be good: adoption rates are rising, research output is high and the efficiency of devices is increasing.[17] A wide range of photovoltaic (PV) technologies are actively being researched, with organic and inorganic technologies vying to replace the successful and still-improving silicon technologies.[18;19] There has recently been a surge of interest in hybrid organic-inorganic solar cells based on materials with the perovskite crystal structure.[20]

In a closer analysis, solar PV in the UK would require significant load-balancing infrastructure in order to provide more than 6 per cent of the nation's electricity, due to its intermittent nature.[16] A hydrogen-based energy economy is also of interest, and visions of this may leave a significant role for photovoltaic generation (with electricity used for water-splitting reactions) or attempt to bypass it entirely in favour of photocatalysis.

It is helpful to relate energy usage and supply to specific land areas: Mackay (2013) calculated an average UK consumption of 1.25 W m^{-2}. In his words:[16]

> *"This areal power density is uncomfortably similar to the average power density that could by supplied by many renewables..."*

Providing renewable energy on this scale requires what Mackay dubs "country-sized" generation facilities. Any operation on such a scale would be among mankind's most ambitious undertakings. An estimate of the required resources for a modest target of 500 GW suggests that the area covered by solar cells of moderate efficiency (10 %) would be approximately equal to the size of Belgium, using 3×10^5 m^3 of material.[21] The estimate is based on a 10 μm-thick light-absorbing layer; this is generous for a "thin-film" technology but too thin for a silicon-based device. Technological breakthroughs will be needed to minimise per-area cost and avoid dependence on supply-limited materials; examination of our resources raises concerns about otherwise-promising technologies, most notably the CdTe and Cu(InGa)Se_2 (CIGS) technologies which otherwise are performing well.[22]

Silicon-based cells do not suffer from material shortages, but are accompanied by specialised and energy-intensive processes which restrict the cost and scaling. There is active research into thinner (100 μm and less) silicon absorbers for this reason.[17]

1.3 Considerations for manufacture of TW-scale photovoltaics

While solar cells may use thin active layers of the order 1–10 μm, they still require a robust substrate for mechanical support. It is established that module and installation costs are substantial relative to the cost of the absorber layer, and also that photovoltaic technology, once installed, adds to the value of a site. *Building-integrated photovoltaics* is therefore an attractive industrial model; large quantities of flat steel and glass sheets are already produced for the building industry. If these materials can be made functional with a modest amount of additional processing time and equipment, then substantial cost savings can be achieved by eliminating the redundant substrate and sharing the transport and installation costs. Building-integrated photovoltaics have the potential to significantly reduce the energy consumption of buildings; a recent study has suggested that such installations would be economical across much of Europe if the installed cost is less than €4 W^{-1}.[23] The SPECIFIC consortium in the UK is an academic/industrial partnership, including a doctoral training centre and pilot facilities, which aims to develop this technology and other building-integrated systems. Press releases by SPECIFIC have suggested that their partner TATA steel produces around 100 Mm^2 $year^{-1}$ of building cladding; this is plausible given that steel production by TATA alone is approaching 10 Mt $year^{-1}$, while global production for 2015 is estimated at over 1.6 Gt $year^{-1}$.[24] Given that the energy output of a typical PV installation is around 100 W m^{-2}, we see that roughly 10 Mm^2 of functional cladding would be needed per GW of energy. This is not a technology that will unlock terawatts of solar energy overnight, but it would bring that goal significantly closer.

The key requirement for such processes is that they can be operated continuously in a "roll-to-roll" fashion, producing long sheets for the building industry. Roll-to-roll processes need to be rapid, as the size of equipment is proportional to the residence time of a processing step. Long annealing stages of minutes to hours are infeasible as they would require ovens which span over kilometres. An alternative approach which has already been demonstrated is rapid heat treatment with halogen lamps.[25;26]

Operation at elevated and reduced pressures is also problematic. It is possible to design "air-to-air" vacuum systems in which a roll is passed through slots into chambers of successively lower pressure, but it is not a trivial design problem.[27] For the rapid deployment of building-integrated photovoltaics, it would be very helpful if new equipment could fit into existing production lines.

Bibliography

[1] J. M. Keynes, in *Essays in Persuasion*, Macmillan, London, 1931, ch. V.2.

[2] Millenium Ecosystem Assessment, *Ecosystems and human well-being: Biodiversity Synthesis*, World Resources Institute, Washington DC, 2005.

[3] *The Long Term Storage of Radioactive Waste: Safety and Sustainability*, International Atomic Energy Agency, Vienna, 2003.

[4] World Commission of Environment and Development, *Our Common Future*, Oxford University Press, Oxford, 1987.

[5] A. D. Pasternak, *Global Energy Futures and Human Development: A Framework for Analysis*, U. S. Dept. of Energy, California, 2000.

[6] J. Chontanawat, L. C. Hunt and R. Pierse, *Journal of Policy Modeling*, 2008, **30**, 209–220.

[7] *The Future of Heating: Meeting the challenge*, Department of Energy and Climate Change, London, 2013.

[8] N. Oreskes, *Science (New York, N.Y.)*, 2004, **306**, 1686.

[9] W. R. L. Anderegg, J. W. Prall, J. Harold and S. H. Schneider, *Proc. Natl. Acad. Sci. U. S. A.*, 2010, **107**, 12107–9.

[10] *Climate Change 2014 Synthesis Report*, ed. R. K. Pachauri and L. Meyer, IPCC, Geneva, Switzerland, 2014.

[11] DARA and the Climate Vulnerable Forum, *Climate vulnerability monitor: a guide to the cold calculus of a hot planet*, Fundación DARA Internacional, Madrid, 2nd edn., 2012.

[12] D. H. Meadows, D. L. Meadows, J. r. Randers and W. W. I. Behrens, *Limits to Growth*, Universe Books, 1972.

[13] Comments on the long-term accuracy of these models and possible inferences are found in later editions of *Limits to Growth*.

[14] BP p.l.c., *BP Energy Outlook 2035*, 2015, `http://www.bp.com/content/dam/bp/pdf/Energy-economics/energy-outlook-2015/Energy_Outlook_2035_booklet.pdf`, [Accessed: 2015-09-21].

[15] Exxon Mobil Corp., *The Outlook for Energy: A View to 2040*, 2015, `http://cdn.exxonmobil.com/~/media/global/reports/outlook-for-energy/2015/2015-outlook-for-energy_print-resolution.pdf`, [Accessed: 2015-09-21].

[16] D. J. C. Mackay, *Philos. Trans. R. Soc., A*, 2013, **371**, 20110431.

[17] S. de Iuliis, *Thematic Research Summary: Photovoltaics*, Energy Research Knowledge Centre, 2014.

[18] A. Le Donne, A. Scaccabarozzi, S. Tombolato, S. Marchionna, P. Garattini, B. Vodopivec, M. Acciarri and S. Binetti, *ISRN Renewable Energy*, 2013, **2013**, 1–8.

[19] O. A. Abdulrazzaq, V. Saini, S. Bourdo, E. Dervishi and A. S. Biris, *Part. Sci. Technol.*, 2013, **31**, 427–442.

[20] X. Liu, W. Zhao, H. Cui, Y. Y. Xie, Y. Wang, T. Xu and F. Q. Huang, *Inorg. Chem. Front.*, 2015, **2**, 315–335.

[21] I. Forbes and L. M. Peter, in *Materials for a sustainable future*, ed. T. M. Letcher and J. L. Scott, Royal Society of Chemistry, Cambridge, 2012, ch. 17, pp. 558–591.

[22] C. Wadia, A. P. Alivisatos and D. M. Kammen, *Environ. Sci. Technol.*, 2009, **43**, 2072–7.

[23] A. Kylili and P. A. Fokaides, *Indoor Built Environ.*, 2014, **23**, 92–106.

[24] *TATA Steel 108th Annual Report*, 2015.

[25] M. Cherrington, T. C. Claypole, D. Deganello, I. Mabbett, T. Watson and D. Worsley, *J. Mater. Chem.*, 2011, **21**, 7562.

[26] C. Charbonneau, K. Hooper, M. Carnie, J. Searle, B. Philip, D. Wragg, T. Watson and D. Worsley, *Prog. Photovoltaics*, 2014, **22**, 1267–1272.

[27] C. A. Bishop, in *Vacuum Deposition onto Webs, Films and Foils*, William Andrew, Oxford, 2nd edn., 2011, ch. 29, pp. 469–480.

Chapter 2

Photovoltaics

> *While there has been significant progress in the development of new photovoltaic systems in the last decade, J. Nelson's* The Physics of Solar Cells *(2003) remains an excellent introduction to photovoltaics.*[1]

2.1 History

The first reported solar cell was constructed by Becquerel in 1839, consisting of platinum plates in an acidic electrolyte.[2] The performance was found to vary depending on different light colours (with green light being optimal), and was also affected by silver halide coatings on the platinum plates; both of these observations allude to important design considerations in the design of modern photovoltaic materials. While researchers subsequently experimented with a variety of systems, it took over a hundred years for a commercially viable solar cell architecture to be developed in the form of a heavily-doped silicon p–n junction — with a short letter from the Bell Telephone Laboratories, the published record efficiency η jumped from 0.5 % to ~ 6 %.[3]

Until recently, photovoltaic installations were typically decentralised as part of "off-grid" self-sustaining systems or, more commonly, supplementing power from national infrastructure. Since 2007 there has been a rapid rise in the use of photovoltaics as part of centralised power networks, and this now makes up over half of installed photovoltaic generation.[4] Overall growth has been close to exponential for two decades; data for the last 15 years is presented in Fig. 2.1 on the next page. While growth has recently dropped in Europe, possibly driven by economic troubles, China's PV installation is rapidly expanding and set to exceed the rest of the Asia-pacific region.

2.2 Operating principles and design

A photovoltaic cell generates an electric current by absorbing light. In the absorber material, incoming photons are used to excite electrons from the highest occupied ("valence") band of electronic states to the lowest unoccupied ("conduction") band, leaving a positively-charged "hole". An efficient device will be designed such that the electrons and holes tend to migrate towards different contacts, creating a potential difference between them. A generic single-junction schematic is given in Fig. 2.2. This is usually achieved with a p–n junction; regions which have been doped to easily "donate" or "accept" electrons (Fig. 2.3) form a diode when brought together, blocking current flow in one direction (Fig. 2.4). When the contacts are connected by an electrical circuit, the flow of current counteracts the build-up of electrons and holes.

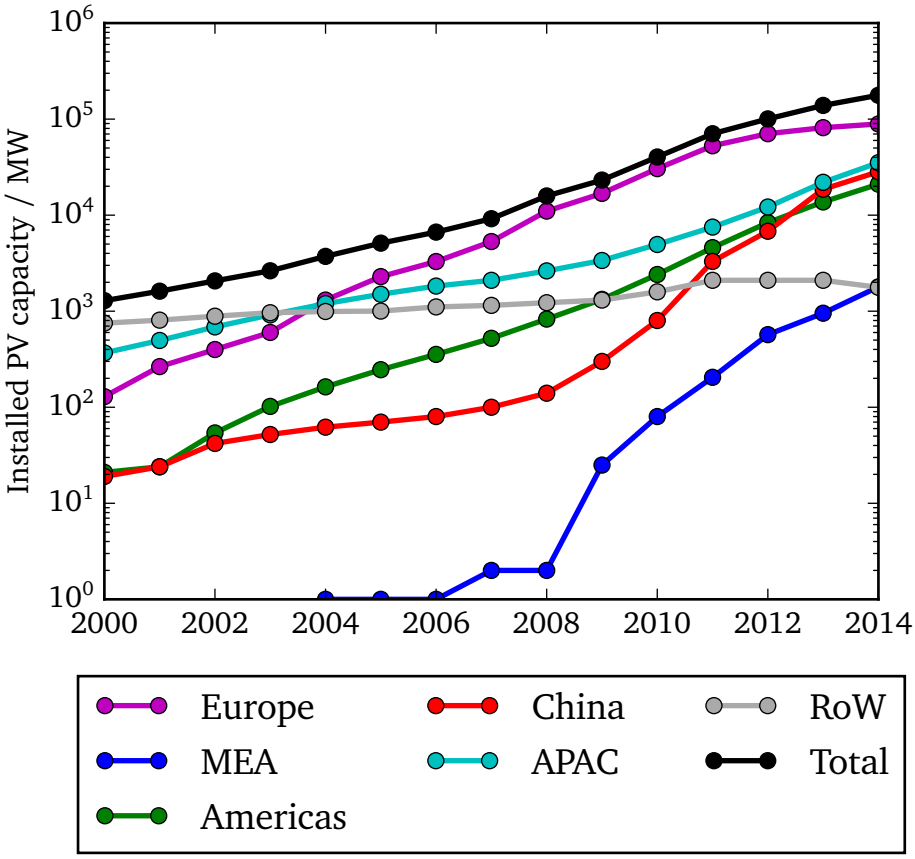

Figure 2.1 – Cumulative PV installation by region: MEA is Middle East and Africa; APAC is Asia-Pacific region except for China which is plotted separately; RoW is "rest of world". Estimates from European Photovoltaic Association (2000–2013) and International Energy Agency (2014).[4;5]

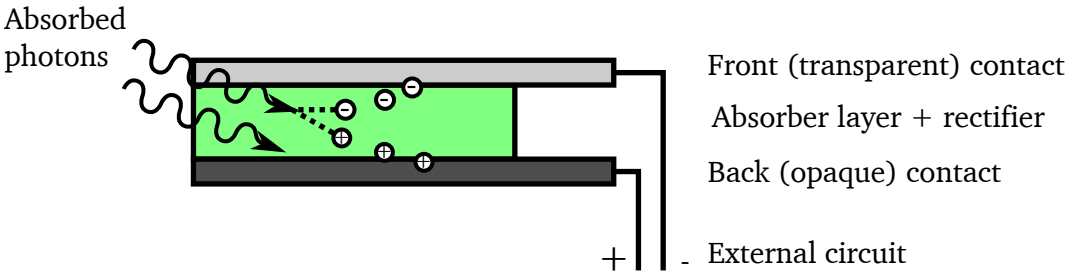

Figure 2.2 – A generic schematic for a single-junction solar cell. Electron-hole pairs are formed by the absorption of photons, and tend to drift to opposite contacts due to the asymmetric design of this region. Typically this is a p–n junction or similar architecture which blocks current flow in one direction (i.e. a rectifier).

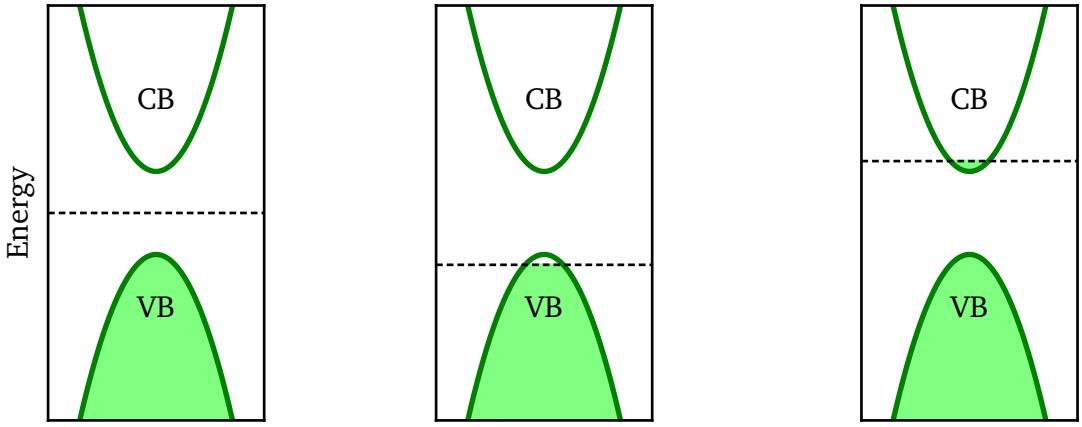

(a) intrinsic **(b)** p-type **(c)** n-type

Figure 2.3 – Simplified schematic of electronic structure in semiconductors. In an intrinsic semiconductor at the ground state (a) the valence band (VB) is fully occupied and the conduction band (CB) is empty. Thermal and optical excitations can promote electrons from the VB to the CB, leaving a "hole" at the valence band maximum (VBM) and adding an electron at the conduction band minimum (CBM) energy. The Fermi level, indicated with a dashed line, is the average energy to add or remove an electron and so lies in the middle of the energy gap. In a p-type semiconductor (b) the VB is slightly electron-poor, shifting the Fermi level near to the VBM while in an n-type semiconductor (c) a small concentration of electrons lies in the CB and the Fermi level lies near the CBM. In a p–n junction the potential difference between electrons in each of these materials drives electrons towards the p-type semiconductor while holes migrate in the opposite direction.

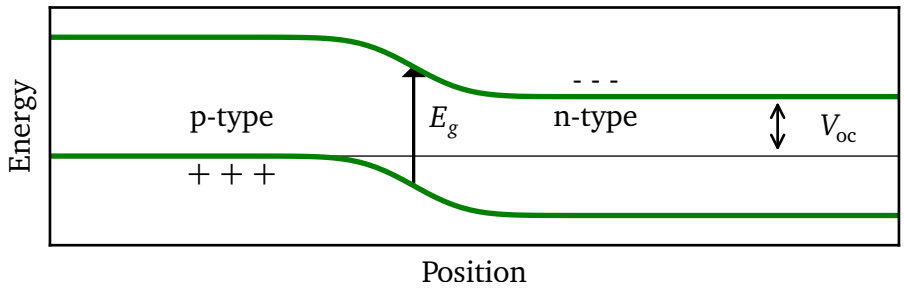

Figure 2.4 – Simplified electronic structure of a p–n junction. Free electrons tend to migrate into the n-type material, following the potential gradient, while positively-charged holes migrate in the opposite direction. This behaviour effectively blocks current flow in one direction, forming a rectifier. When the material is a PV absorber, excitation events take place between energy levels at the interface (arrow), adding an electron to the conduction band (CB) and a hole to the valence band (VB). When these drift apart a potential difference, indicated here as V_{OC}, is created. Note that this open-circuit voltage across the p–n junction depends on both the fundamental energy gap (E_g) and the band offset between the n- and p-type materials.

The key properties of a photovoltaic device as outlined by Nelson are:

- Energy gap
- Light absorption
- Charge separation (asymmetry)
- Electron/hole transport
- Load resistance

The "energy gap" or bandgap E_g is the energy taken to generate an electron-hole pair; this is usually taken to be the energy difference between the minimum energy state in the conduction band (CBM) and the maximum energy state in the valence band (VBM). E_g is directly related to a theoretical maximum efficiency for a single-junction solar cell, around 30 %, known as the "Shockley–Queisser limit".[6] As the solar cell is exposed to a spectrum of photons with different energies, photons with energy equal to E_g can be absorbed and create an electron-hole pair with the corresponding energy. If a photon with energy greater than E_g is absorbed, an electron is excited higher into the conduction band but will quickly relax to the band edge, losing the difference in energy as heat. If the photon energy is less than E_g, no excitation is possible and the energy of that photon is unavailable. The result is that

> photons with energy greater than $[E_g]$ produce precisely the same effect as photons of energy $[E_g]$, while photons of lower energy will produce no effect.[6]

To maximise power, a trade-off is made between the higher voltage obtained by increasing E_g and the higher current generated by the increased rate of excitation events at low E_g. The optimal point depends on the distribution of photon energies; a number of solar spectrum models have been employed but in general the optimum lies in a relatively flat region $E_g = 1$–$1.5\,\mathrm{eV}$. Higher efficiencies are possible for a *multi-junction* cell in which photons are absorbed by several layers with differing E_g. The theoretical limit is over 85 % for an infinite series of layers, dropping to around 55 % for four layers and 50 % for three layers.[7] Given the additional complexity of such devices, they are developed for specialist applications where space and weight are at a premium (e.g. space programs).

"Thin film" solar cells are the category of solar cells which use absorber layers with very high absorption coefficients. This distinguishes them from crystalline silicon (x-Si) cells, which have an order of magnitude lower absorption coefficient; as a result, thin-film absorber layers are of the order 1–100 µm in thickness, whereas x-Si absorbers are of the order 1 mm in thickness. As well as reducing the material requirement and weight, thinner absorber layers lead to a reduced distance between charge carriers and terminals which should lead to low recombination. In practice, achieving low recombination in thin-film devices can be quite difficult and depends heavily on the device design and grain structure. The grain boundaries between regions of a polycrystalline absorber often act as recombination sites.

While the device physics of solar cells is not directly related to the work in this thesis, it is necessary to introduce here the basic single-diode device model (Fig. 2.5), as the terminology is widely used in discussions of material performance. The p–n junction is treated as a current generator in parallel with a diode; the rectifying properties of the diode regulate the voltage resulting from the current generation. Current generation is proportional to incident light; under no load this is the *short-circuit current*, J_{SC}. At infinite load, the voltage across the circuit is the *open-circuit voltage*, V_{OC}. Under no illumination, the device acts as a simple diode, passing a *dark current* J_{dark} in response to a bias voltage. Various parasitic processes are approximated by two resistors; one in series R_{s} and one in parallel R_{sh}. The *series resistance* reduces the voltage across the external circuit (and hence available power) at high current conditions, while the *shunt resistance* R_{sh} represents voltage loss due to alternative paths between the contacts. These values can be estimated by fitting current-voltage data to the model, providing insight into the quality and limitations of a device.

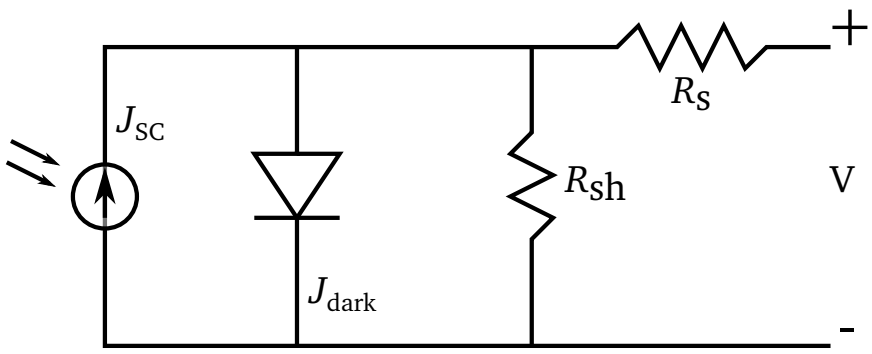

Figure 2.5 – Single-diode equivalent circuit diagram for a solar cell. Current generator (far left) produces current proportional to incident light (short-circuit current, J_{SC}), with voltage regulated by a diode. The dark current J_{dark} is passed when the current generator is inactive. Two resistors represent series (R_s) and parallel "shunt" (R_{sh}) losses.

Bibliography

[1] J. Nelson, *The physics of solar cells*, Imperial College Press, London, 2003.

[2] E. Becquerel, *C. R. Hebd. Seances Acad. Sci.*, 1839, **9**, 561.

[3] D. M. Chapin, C. S. Fuller and G. L. Pearson, *J. Appl. Phys.*, 1954, **25**, 676–677.

[4] IEA Photovoltaic Power Systems Programme, *Trends 2015 in Photovoltaic Applications*, International Energy Agency Technical Report IEA-PVPS T1-27:2015, 2015.

[5] G. Masson, S. Orlandi and M. Rekinger, *Global market outlook for photovoltaics 2014-2018*, European Photovoltaic Industry Association, 2014.

[6] W. Shockley and H. J. Queisser, *J. Appl. Phys.*, 1961, **32**, 510.

[7] A. Martí and G. L. Araújo, *Sol. Energy Mater. Sol. Cells*, 1996, **43**, 203–222.

Chapter 3

Kesterite photovoltaics

3.1 The structure and properties of CZTS

3.1.1 Structure

Cu_2ZnSnS_4 (CZTS) was introduced as a semiconductor by Ito and Nakazawa in 1988, with absorption coefficients greater than $10^4 cm^{-1}$, p-type conductivity and a bandgap of 1.45 eV.[1] Thin ($< 1\,\mu m$) films were produced by sputtering from a quaternary target, which was prepared by annealing and grinding a mixture of the elements. Their work followed an initial demonstration of the stability of CZTS as part of a systematic study which had formed 13 different quaternary $A^I_2B^{II}C^{IV}X^{VI}_4$ compounds by iodine vapour transport.[2] Interest was revived in the late 1990s by Katagiri *et al.*[3] with a study which confirmed these properties after forming a thin film by annealing electron-beam-evaporated metal layers in hydrogen sulfide.[3] While all three of these groups initially assigned the stannite crystal structure (space group $I\bar{4}2m$) to their samples, there is now a consensus that the kesterite structure (space group $I\bar{4}$) is the ground-state arrangement for Cu_2ZnSnS_4in the absence of impurities. This has been informed by neutron diffraction experiments and theoretical calculations.[4–8] The names "kesterite" and "stannite" are derived from natural minerals with the nominal stoichiometry $Cu_2(Zn_xFe_{1-x}SnS_4)$; Hall *et al.* examined a kesterite sample with $x = 0.73$ and a stannite sample with $x = 0.18$, also finding traces of cadmium in both.[9] Since then, experiments and theoretical calculations suggest that a mixed kesterite-stannite phase is favourable at intermediate Zn:Fe ratios, with Cu_2ZnSnS_4 being strictly kesterite and Cu_2FeSnS_4 being strictly stannite.[10;11] Both structures are related to the cubic zinc blende (or "sphalerite") structure, with each S anion tetrahedrally coordinated to four metal cations and *vice versa*. The symmetry is lowered due to the variety of cations (Cu, Zn, Sn as opposed to just Zn), leading to tetragonal unit cells (Figs. 3.1a and 3.1b) with different cation arrangements. Hexagonal analogues also exist, with similar layering to the kesterite and stannite arrangements on a different fundamental lattice (Figs. 3.1c and 3.1d).[12] The presence of cation disorder may have contributed to the early assignment of a stannite phase, as disordered kesterite can have the same $I\bar{4}2m$ space group. (Cation disorder is discussed further in Section 3.2.2 on page 42.) It is also possible to substitute S for Se, and the highest-performing kesterite-based photovoltaic devices have been Se-rich sulfo-selenides.[13–17] The full range of S:Se ratios has been explored and the lattice parameters appear to vary smoothly between the known kesterite structures for CZTS and CZTSe, although the presence of secondary phases is possible.[18;19] This thesis focuses on sulfides.

In addition to the incorporation of other elements including Fe and Cd, there is some compositional flexibility in the form of vacancies and lattice substitutions. The single-crystal investigation by Choubrac *et al.*[20] used a combination of XRD and calibrated elemental analysis with wavelength dispersion spectrometry to confirm that two samples, one close to the

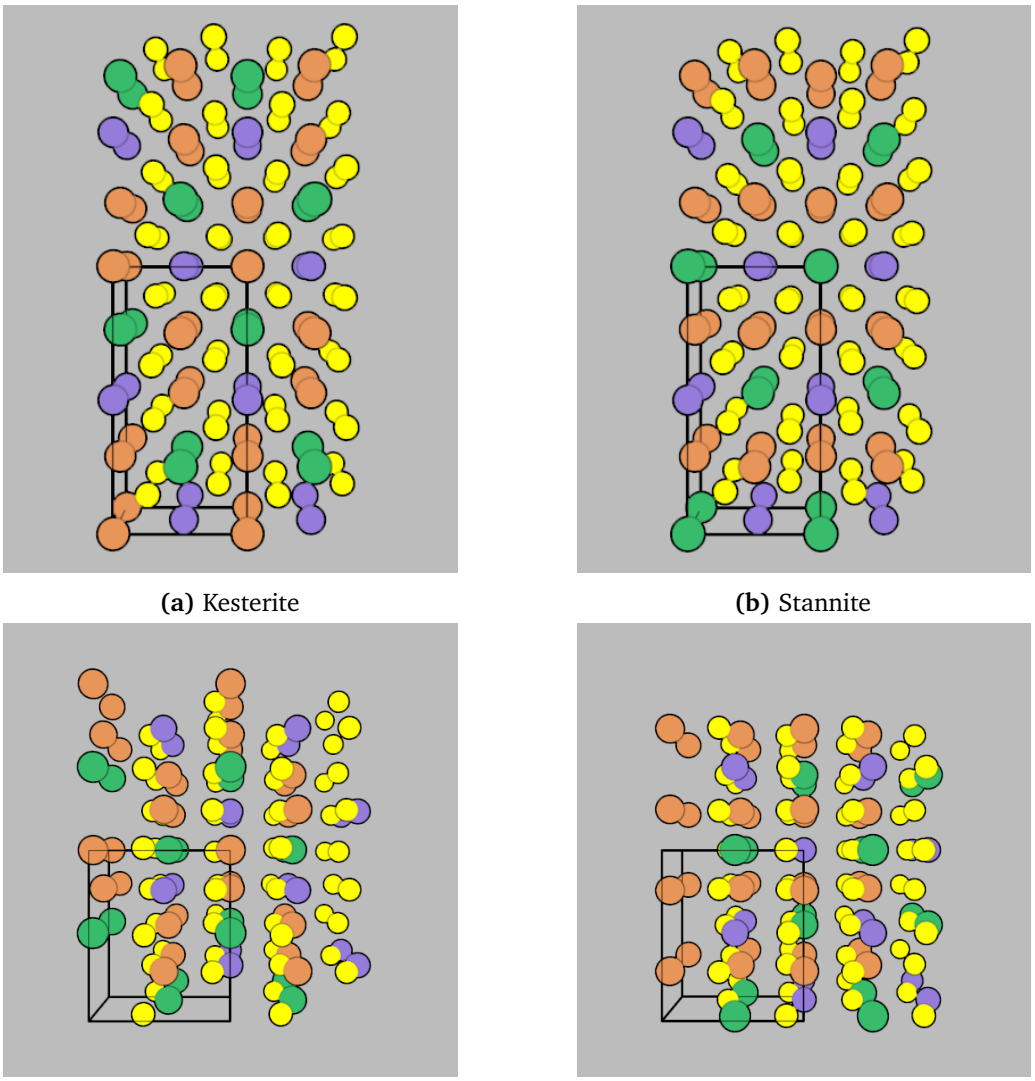

(a) Kesterite **(b)** Stannite

(c) Wurtzite-kesterite **(d)** Wurtzite-stannite

Figure 3.1 – Illustrated crystal structures of (a) kesterite ($I\bar{4}$) and (b) stannite ($I\bar{4}2m$) structures of Cu_2ZnSnS_4, with their (c) wurtzite-kesterite (Pc) and (d) wurtzite-stannite ($Pmn2_1$) analogues. The conventional unit cells are indicated with black lines. Colour scheme: ● Cu; ● Zn; ● Sn; ● S. Note that in the kesterite structure, all Cu atoms are linked by a network of Cu–S–Cu second-nearest neighbours while in the higher-symmetry stannite structure Cu layers are separated by layers of the other cations. The wurtzite-derived analogues show comparable cation ordering along a different lattice.

Table 3.1 – Bandgap estimates for CZTS and CZTSe from key *ab initio* studies, in kesterite and stannite phases where available. Two sets of values are provided from calculations with screened hybrid DFT (HSE06): in the first, the lattice parameters were optimised to minimise the total energy; in the second, the experimental lattice parameters were used. All values are in eV.

	CZTS		CZTSe		References
	Kesterite	Stannite	Kesterite	Stannite	
LDA	1.2		0.9		24
GGA+U	1.56	1.42	1.05	0.89	7
$HSE06_{Opt}$	1.487	1.295			5
$HSE06_{Expt}$	1.50		0.96		6

ideal stoichiometry and one "copper-poor" sample with stoichiometry $Cu_{1.71}Zn_{1.18}Sn_{0.99}S_4$, both belonged to the space group $I\bar{4}$.[20] The ability to maintain Cu vacancies may in fact be an essential property of CZTS and the origin of its p-type conductivity, in which case a trade-off is made between the ideal crystallinity of a sample and its electron/hole transport properties.[21]

3.1.2 Electronic properties

Some of the terminology for ab initio *calculations used here is explained in Chapter 4.*

The range in bandgap between sulfide and selenide kesterites allows the bandgap to be "tuned", and record efficiencies have tended to involve such S–Se alloys. There is little serious suggestion that this is related to the Shockley–Queisser limit however. The full bandgap range lies around the optimal region, while the correlation between device efficiency and S:Se ratio is weak.[22;23]

The first *ab initio* study of CZTS was as late as 2005 by Raulot *et al.*, using electronic structure calculations to examine the bandgaps and formation energies of several chalcopyrites.[24] The shortcomings of the Local Density Approximation (LDA) limited the predictive power of the work, but it was a significant proof-of-concept nonetheless and yielded useful estimates of the bandgaps of CZTS and CZTSe.* These are shown with computed bandgap estimates from a selection of other publications in Table 3.1, and in general the computed values fall within the experimentally observed range. The first study with high-level calculations came a few years later in 2009, employing the HSE06 hybrid DFT functional and the G_0W_0 method (a non-self-consistent post-Hartree Fock refinement of eigenvalues, in this case from HSE).[5] The orbital-projected density of states (pDOS) calculations in that work do appear to show hybridisation between the S-3*p* and Cu-3*d*, dominating the valence band while the first conduction band is assigned as an anti-bonding combination of Sn-5*s* and S-3*p* orbitals. As a result of the Sn-5*s*/S-3*p* hybridisation the authors proposed formal charges of +3 and -1.75 for Sn and S respectively. Agreement was fairly strong between HSE06 with and without the G_0W_0 correction. A detailed study of the electronic band structure calculated with the GGA+U method was published at around the same time, noting the relatively flat band structure about the valence and conduction bands.[7]

This property has been linked to the high optical absorption coefficient of CZTS, as it leads to a high density of states in the target frequency range. CZTS and CZTSe slightly out-perform CdTe for absorption in the visible region, with the required thickness of crystalline silicon being 10–100 times greater than the thin film materials.[25;26] The onset of absorption at the bandgap is rapid, but not as "sharp" as other thin-film absorbers including CdTe and GaAs.[25;26]

*Calculations with this type of local functional tend to drastically underestimate the energies of unoccupied states. In this case the effect was reduced by comparing the energies of charged supercells rather than directly using the Kohn–Sham eigenvalues.

3.2 Principles of CZTS devices

3.2.1 Formation of thin films and device fabrication

Device architecture

A typical CZTS device is shown in cross-section in Fig. 3.2. The architecture is heavily influenced by the design of devices with $CuIn_xGa_{(1-x)}Se_2$ (CIGS) absorber layers. Soda-lime glass (SLG) sputtered with Mo is typically used as the back contact; high-quality SLG is almost atomically flat as it sets from a molten liquid which floats on molten metal. The Mo coating is required to create a conductive surface which adheres well to crystalline absorber layers. Typically this is done in two steps, with a dense layer of Mo binding to the glass and a second layer increasing the thickness; a subtle seam between the layers is usually visible in cross-section micrographs such as Fig. 3.2. Fluorine-doped tin oxide has been demonstrated as an alternative to Mo for a glass-supported contact.[27] Thin steel sheets are a commercially attractive alternative substrate, and there have been some experiments with these. The key challenge is the diffusion of Fe into the absorber layer, which impairs performance. In experiments with CZTSe, barrier layers of Cr and Mo have been found to block this diffusion.[28] So far, record efficiencies on steel are lagging behind those on glass with a recent record of 6.1 % achieved by incorporating Na into the Mo layer.[29]

The CZTS absorber layer is deposited by a variety of methods as outlined in the next section. The thickness is typically $\sim 1\,\mu m$ and in almost all cases the film is annealed following initial deposition in order to improve the crystallinity. A noted exception is the "monograin" method of Crystalsol in which individual, non-contacting, grains of CZTS are embedded in a polymer layer separating the front and back contacts.[30]

CZTS absorber layers are "p-type", favouring the presence of holes. In order to form a p–n junction, a thin "buffer layer" of n-type material is deposited. In high-performing CZT(S,Se) devices this is always CdS. The chemical bath deposition of CdS is well established — a recent review included 34 recipes from the literature.[31] High-performing CZTS cells have been produced by photovoltaics researchers with experience in the CIGS field, who adapted CIGS device fabrication methods including the CdS buffer deposition.[32;33] The cadmium content of CdS undermines the sustainability credentials of CZTS in the long run, but it is not technically a requirement for a CZTS device and there has been some experimentation with cadmium-free kesterite devices.[34;35]

A transparent conducting oxide (TCO) layer helps create an electrical contact at the front of device. As a "window layer" the wide-bandgap TCO has another important role; the high conduction band energy "reflects" minority carriers, reducing the rate of recombination at the front contact.[26] Various combinations of indium tin oxide (ITO), intrinsic Zinc Oxide (i-ZO) and aluminium-doped zinc oxide (AZO) are used in practice. These are deposited by sputtering in vacuum. The current record-holding high efficiency cells use an i-ZO/ITO combination, with an anti-reflective coating of MgF_2.[17] This was based on optical modelling, suggesting that an optimal device would have a minimal buffer layer thickness and 50 nm of TCO in total.

Deposition of CZTS thin films

Table 3.2 on the next page provides a summary of some relevant deposition methods. These may loosely be sorted into "dry" processes and "solvent-based" methods. The sputtering approaches and pulsed laser deposition have similar strengths and weaknesses, in that they offer a good level of control for the production of research samples but require equipment that is expensive, specialised and difficult to scale-up. Nonetheless, the companies Solar Frontier

Table 3.2 – Summary of deposition methods for kesterite absorber layers. References are given for a mixture of sulfide, selenide and mixed chalcogenide preparations, but all methods are assumed to be transferable to the pure sulfide. The papers referred to have been selected on the basis of interest, and are not necessarily the first accounts of these methods being used.

Deposition method	Summary	References
Chemical vapour transport	A volatile transport agent (iodine) is driven by a temperature gradient to form crystals in an evacuated vessel.	37
Electrodeposited metal stacks	Standard electrochemical methods are used to deposit sequential sheets of Cu, Zn and Sn from solution before annealing in a S/Se atmosphere.	38;39
Sputtered metal stacks	Sequential layers of metals are deposited on substrate by magnetron sputtering before annealing in a S/Se atmosphere.	40
Reactive sputtering	CuSn alloy and Zn targets are sputtered simultaneously in a vessel containing a chalcogen source such as H_2S at low pressure.	41
Quaternary target sputtering	A CZTS target is prepared by other means and sputtered to form a thin film on the target substrate.	1
Pulsed laser deposition	A target in a vacuum chamber is evaporated and ablated by intense laser pulses. The resulting jet of material coats the device substrate, in a similar manner to magnetron sputtering.	42
Chemical bath deposition	Precursors are dissolved in hydrazine, or a less aggressive solvent with the aid of ligands. The solution is deposited on the substrate by one of many methods include spin-coating and inkjet printing. Ions in solution form a film as the solvent is evaporated. Successive ionic layer adsorption and reaction (SILAR) is a variation in which atomic layers of each precursor (which may be a binary or ternary compound) are deposited in ~ 100 successive steps.	13;43–45
Slurry deposition	Solid CZTS or precursors are finely ground and suspended in a solvent to form an “ink”. This ink is deposited and evaporated to leave a layer of precursors; a crystalline thin film is formed by annealing in S/Se.	46;47

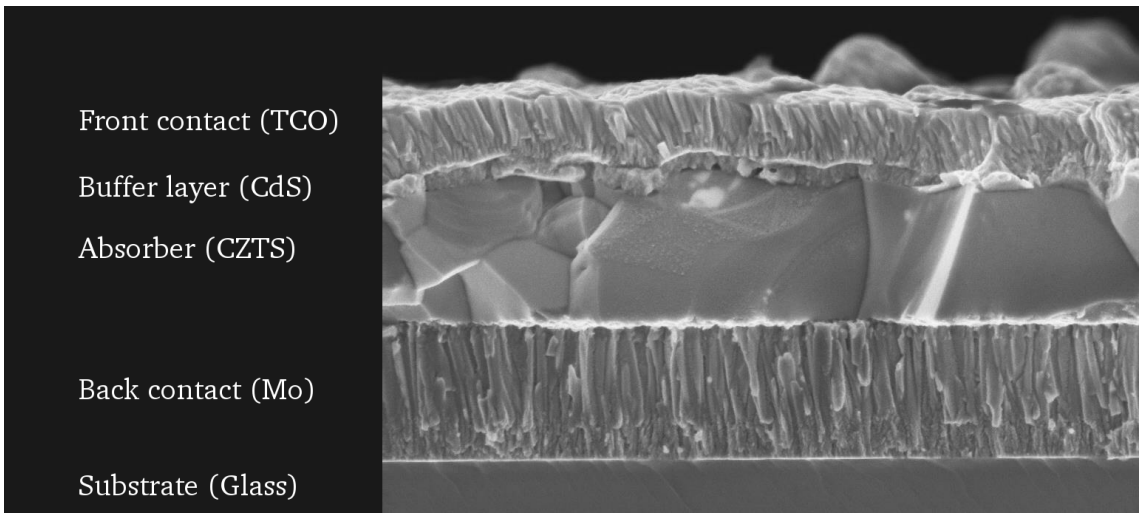

Figure 3.2 – Cross-section of a typical CZTS device. The top contact is a transparent conducting oxide (TCO) such as AZO or ITO (see main text); a thin ($\sim 100\,\text{nm}$) CdS buffer layer forms the p–n junction with CZTS absorber ($\sim 1\,\mu\text{m}$). A Mo back contact is typically sputtered in two stages onto soda-lime glass (SLG). Electron micrograph reproduced with permission from a conference poster by researchers at DTU (Technical University of Denmark).[36]

and FirstSolar are currently producing CIGS and CdTe cells respectively and hold intellectual property relating to large-scale roll-to-roll sputtering processes.[48;49]

Solution processing holds a strong industrial appeal, as it implies readily-scaleable technology with inexpensive equipment. Chemical bath deposition (CBD), in which ions in solution directly form a compound precipitate on a surface, is established for the deposition of many metal chalcogenides including CdS and ZnS.[31] However, it has proven challenging to solubilise the precursors for CZTS. A series of record efficiencies were set by researchers at IBM, using hydrazine as a solvent; this is problematic as hydrazine is quite hazardous.[13–17] Successes in ethanol and DMSO have involved more complex precursors such as thiourea, but are amenable to a wider range of processing methods. For several years, hydrazine-derived devices held a strong lead in terms of solar conversion efficiency and only recently have other approaches begun to catch up. Researchers have used extrinsic dopants including sodium to achieve 'hydrazine-like' efficiencies, close to 10 %, by solution processing in DMSO with thiourea.[50]

Large crystals of CZTS may be produced in a slow solid-state/melt reaction; these are sometimes used as a precursor for deposition, as well as for reference measurements.[4;10] As an alternative, many research groups have focused on the production of CZTS nanoparticles.[51] The metal species are solubilised in an organic solvent by the addition of appropriate ligands. CZTS nanoparticles precipitate following the hot injection of a sulfur source into this solution. The size and composition of these nanoparticles is tuned by experimenting with different solvents, sulfur sources and ligands. The precipitate is deposited onto a substrate and annealed to form a crystalline film.[52]

3.2.2 Defects and disorder

The early theoretical study by Raulot *et al.*[24] considered Cu vacancies in CZTS and CZTSe, finding formation energies of 0.90 and 0.49 eV respectively.[24] Subsequent *ab initio* studies also examined defect formation energies, finding the Cu'_{Zn}, V'_{Cu} and Zn''_{Sn} defects to have especially low formation energies, as well as the defect clusters $\text{V}'_{\text{Cu}} + \text{Zn}^{\bullet}_{\text{Cu}}$ and $\text{Cu}'_{\text{Zn}} + \text{Zn}^{\bullet}_{\text{Cu}}$.[21;53] (The Kröger-Vink notation for defects is explained in the box on the facing page). Changes in the bandgap in the order of 0.1 eV have been predicted through supercell calculations, noting that while the copper vacancy cluster $\text{V}'_{\text{Cu}} + \text{Zn}^{\bullet}_{\text{Cu}}$ acts to increase the bandgap it is counteracted by

KRÖGER-VINK NOTATION is used to describe particular sites on an assumed regular lattice. The notation for species A on a site normally occupied by species B is A_B. In addition, the charge is noted relative to the nominal charge of the site; relative charges of +1, +2, +3… are indicated $A_B^{\bullet}$, $A_B^{\bullet\bullet}$, $A_B^{\bullet\bullet\bullet}$…, while relative charges of -1, -2, -3… are indicated A_B', A_B'', A_B'''… For example, on a NaCl lattice the charge associated with a Na site is typically +1; if occupied by a Cl^- anion the site would become Cl_{Na}''. A neutral charge is declared with a cross: $A_B^{\times}$.

As well as chemical species, it is useful to declare a vacancy (i.e. the absence of a species on a lattice site) with the letter "V", and interstitial sites may be denoted "i". An unfilled lattice interstitial, while generally unremarkable, may thus be notated $V_i^{\times}$.

Informal variations exist; the charge notation may be omitted and left to the reader's interpretation of the system. This is common in CZTS-related literature, possibly due to the covalent nature of the lattice; using the Kröger-Vink notation implies an ionic character that often only exists as a model. The charge notation may be replaced with the more familiar + and − characters; this is ambiguous however and may represent the *overall* charge on a site.

the $Cu_{Zn}' + Zn_{Cu}^{\bullet}$ disorder which has the opposite effect.[54]

It has been noted that alternative arrangements of the Cu and Zn cations in the conventional kesterite cell can lead to $P\bar{4}2c$, $P\bar{4}2_1m$ and $P2$ structures.[8] The disordered kesterite structure with space group $I\bar{4}2m$ was eventually refined using resonant X-ray diffraction, a technique which is not available in standard laboratories.[55] Raman spectroscopy (described on on page 46) is more widespread, and while observations have been linked to kesterite lattice disorder some ambiguity remains.[56;57] Near-resonant Raman data has been used in a Vineyard model to identify a critical order-disorder transition temperature of $(533 \pm 10)\,K$.[57] (These studies are discussed in more detail in Section 7.2.1 on page 115.) Cu-Zn disorder was observed directly with aberration-corrected scanning transmission electron microscopy (STM).[58]

3.3 Challenges in the development of CZTS devices

3.3.1 V_{OC} deficit

Current-voltage measurements are routinely used to characterise photovoltaic devices, with the results interpreted through simple models such as the equivalent circuit introduced in the previous chapter (Fig. 2.5 on page 35). In practice, the open-circuit voltage V_{OC} is always less than that associated with the measured bandgap. This difference is known as the *V_{OC} deficit* and contributes to the low efficiency of even the highest-performing devices. V_{OC} deficits have also been noted in CIGS, but while record-efficiency CIGS devices have a deficit of around 0.4 V, the best CZTSSe devices are under-performing by over 0.6 V.[59] The deficit appears to be fairly consistent across high-performing devices (Fig. 3.3). The *fill factor* (FF) is a ratio between the product $J_{SC} \times V_{OC}$ and the actual maximum power, and can be taken as another measure of how "ideal" the circuit is, incorporating parasitic effects. As also seen in Fig. 3.3, this varies significantly between devices and is correlated with the efficiency, suggesting that these parasitic effects play quite a significant role.

A number of mechanisms have been proposed which might contribute to the V_{OC} deficit. Most investigations suggest that a combination of these processes is at work, as the voltage loss associated with individual mechanisms is only a fraction of the total V_{OC} deficit.

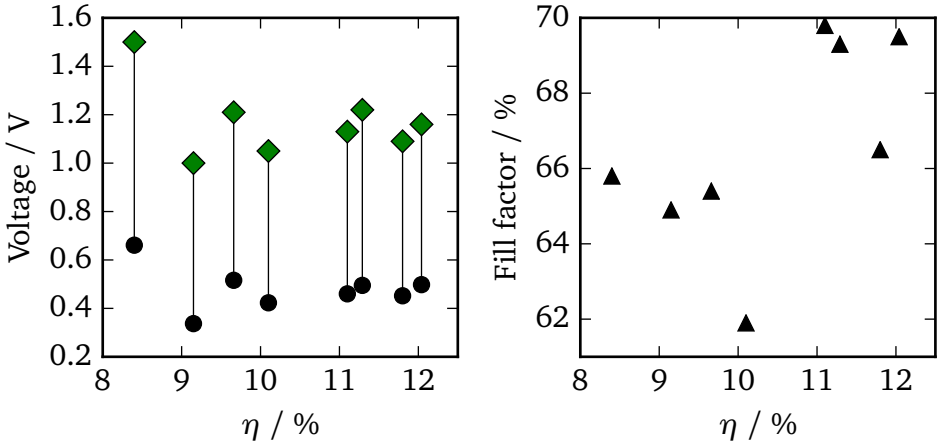

Figure 3.3 – V_{OC} deficit and fill factor in high-performing devices. Data is drawn from a paper comparing several new high-performing devices with previous record-holders.[16] The optical bandgap E_g (green diamonds at corresponding voltage), measured V_{OC} (black circles) and calculated fill-factors (black triangles) are given for a selection of CZTSSe devices, plotted against the energy conversion efficiency η of each device. The difference in voltage between each corresponding E_g and V_{OC} measurement is the *V_{OC} deficit*, and appears to be fairly consistent. A broad positive correlation is noted between the fill factor (FF) and η, with a couple of outliers.

Electron–hole recombination As the current is reduced on one side of the p–n junction, the electron–hole equilibrium shifts and the potential difference across the junction drops. Grain boundaries are a likely site for recombination, suggesting that samples with poor crystallinity and interface matching would be particularly vulnerable to this mechanism. A low minority carrier (i.e. electron) lifetime has been measured in CZTSe, linked to a shortfall of 0.03–0.05 V in the V_{OC}.[60] A device-model-led study of a CZTS device formed using reactive sputtering has attributed larger shortfalls to recombination, both in the bulk and at interfaces.[61]

Low conductivity Where conductivity is poor for the majority carrier (i.e. holes), the low hole current would distort the p–n junction as in the case of electron–hole recombination. Device modelling and analysis of high-performing devices suggests that carrier mobility is low in CZTSSe compared to CIGS, but not low enough to explain the large V_{OC} deficit observed in practice.[59]

Tail states and "deep traps" The presence of defects and secondary phases can lead to the existence of mid-bandgap states. Some of these have been specifically identified, and data is available from *ab initio* calculations for the band alignment of defects and defect clusters in CZTS.[62] Such states can have the effect of "pinning" the Fermi level, limiting the available voltage at high light intensities. The most problematic "deep" states, which cut the effective bandgap by almost half, are associated with vacant or out-of-place Sn atoms. These have a relatively high formation energy compared to defects on the (Cu,Zn) sub-lattice which lead to shifts of the order 0.1 eV. Sulfur vacancies are also associated with a deep state. In a low-temperature photoluminescence study of samples cooled at different rates, radiative recombination was attributed to disorder on the cation sub-lattice in highly disordered samples and to deep acceptor defects in the most ordered samples.[63] A recent experimental study demonstrated a strong correlation between the degree of ordering in a sample and the photoluminescence peak energy. This was supported by theoretical calculations using hybrid DFT to show a reduction in the bandgap of over 250 meV at a high level of disorder.[64] There are two proposed mechanisms for V_{OC} deficit associated with spatial inhomogeneity: Fluctuations in the bandgap lead to inconsistent absorption and losses to sub-bandgap radiative recombination events. Fluctuations in the electrostatic potential can create "traps" which localise charge carriers and create favourable sites for recombination.

Non-ohmic contact The equivalent circuit model of a photovoltaic device includes a series resistance, representing simple resistive losses through the device and at interfaces. However, it is possible that this is an over-simplification of the processes involved. In the study of high-performance cells under extreme (> 100 suns) light intensities, a non-ohmic back contact modelled as an additional diode and parallel resistance was used to explain the "band bending" phenomenon in which the voltage was observed to drop under very high light intensities.[59]

3.3.2 Effects of secondary phases

ZnS is commonly found in CZTS devices near the back contact.[65] Due to its large bandgap, it is not thought to directly contribute to the V_{OC} deficit by adding mid-gap states. However, the presence of a secondary phase at interfaces is still undesirable as the grain boundaries are potential recombination sites. In a series of X-ray absorption measurements, increased ZnS content was strongly correlated with reduced V_{OC} and cell efficiency.[66] In addition, the high series resistance observed in CZTSSe devices has been attributed to blocking at the back contact.[67;68]

Copper sulfide phases are anticipated when CZTS is formed in copper-rich conditions, and a KCN etching procedure has been inherited from work with CIGS.[69] Copper chalcogenides are concerning secondary phases as they are associated with high hole transport — and hence a low shunt resistance.[70;71] The conductivity is around $20\,\mathrm{S\,cm^{-1}}$, an order of magnitude higher than CZTS.[72]

Ternary phases consisting of Cu, Sn, (S,Se) are suspected to contribute to the V_{OC} deficit due to their lower bandgap.[65] There has been little investigation of the band offsets between CZTS and ternary phases, but the low bandgap of these phases is assumed to be detrimental.

The sulfides of tin (SnS, Sn_2S_3 and SnS_2) are semiconductors; while the measured bandgaps occupy a wide range, the values computed with hybrid DFT for SnS and Sn_2S_3 are both suitable for photovoltaics at around 1.1 eV.[73] In contrast to these p-type materials, SnS_2 is n-type and has a larger bandgap. While there is some interest in the use of these materials as PV absorbers in their own right, they have poor band alignment with CZTS. The valence band maxima (VBM) of SnS and Sn_2S_3 lie in the middle of the CZTS bandgap, as does the conduction band minimum (CBM) of SnS_2. As a result of this their presence is expected to lower the efficiency of a CZTS device. It has been demonstrated in CZTSSe devices that selective etching with $(NH_4)_2S$ can lower the Sn(S,Se) content, and that this is associated with an increase in efficiency.[74]

The decomposition of CZTS to release SnS vapours when annealed in a vacuum was of particular interest in 2010–2011, and led to general advice to supply excess tin and sulfur when annealing in vacuum.[75–77] This has not been followed by all researchers however, with many apparently relying on the kinetics of the system to prevent this decomposition pathway. The local pressure in the graphite boxes used in many annealing arrangements may also inhibit the process.

3.3.3 Detection of secondary phases

The identification of secondary phases in a sample is an important aspect of characterisation which can give insights into the quality of formation and possible problems. A selection of methods is discussed below.

X-ray diffraction Crystallographic structures are typically identified and studied using X-ray diffraction (XRD); single-crystal samples may be analysed over a specific range of orientations,

Table 3.3 – Reported lattice parameters in Å from XRD study of tetrahedrally-coordinated metal chalcogenides. Low-temperature values used where available.

Stoich.	space group	*a*	*b*	*c*
Cu_2ZnSnS_4	$I\bar{4}$	5.427,[9] 5.434,[20] 5.430[20]		10.871,[9] 10.838,[20] 10.822[20]
Cu_2ZnSnS_4	$I\bar{4}2m$	5.449,[9] 5.426,[3] 5.428[4]		10.757,[9] 10.864,[4] 10.81[3]
Cu_2SnS_3	$I\bar{4}2m$	5.412[79]		10.810[79]
Cu_2SnS_3	$F\bar{4}3m$	5.434[79]		
Cu_2SnS_3	Cc	6.653[80]	11.537[80]	6.665[80]
ZnS	$F\bar{4}3m$	5.4053[81]		

while powdered samples provide data for all orientations simultaneously. XRD relies on the elastic scattering of X-rays by electrons; the periodic electronic structure of crystals leads to constructive and destructive interference patterns which contain information about the lattice spacing and symmetry. XRD is an extraordinarily precise technique, able to provide a resolution of 10^{-3} Å with standard equipment. However, it is poorly-suited for the study of CZTS phase equilibria for two reasons:

1. The lattice parameters of the tetrahedrally coordinated sulfides ZnS, CTS and CZTS are very similar, and overlap given the differences between samples in practice; examples are given in Table 3.3.

2. The electronic structures of Cu and Zn are almost indistinguishable by XRD as they differ only in the lower-lying *s* shell; this can make symmetry assignment and the observation of multiple coexisting phases difficult.

As a result, researchers using XRD have reported difficulty in definitively assigning phases based on XRD patterns alone.[78] It is possible to refine XRD data by carrying out additional neutron diffraction experiments; Cu and Zn nuclei cause neutrons to scatter quite differently, allowing them to be distinguished. This work has been carried out for kesterite CZTS and a range of iron-containing compositions (associated with a shift to the stannite structure), but the technique is not practical for routine characterisation work due to the need for access to a neutron source.[4] In addition, the technique is not applicable to thin-film samples.

Raman spectroscopy For these reasons, the preferred method of "routine" sample characterisation for CZTS absorber layers is Raman spectroscopy, which is often used to complement data from XRD. In Raman spectroscopy, a monochromatic light source is scattered by the changing electron density of a set of vibrating atoms; this results in a set of measurable frequency shifts about the incident frequency. Changes in the Raman spectrum therefore correspond to changes in the bonding environment. In molecules, these frequencies correspond to a subset of the normal vibrational modes, while in a periodic lattice, the observable frequencies form a subset of the Γ-point phonon modes. (The nature and notation of vibrational modes is outlined in Sections 5.2.3 and 5.3.) An overall change in the polarisability is required for the Raman effect to occur, which is why off-Γ modes and some high-symmetry modes are not observed. With *ab initio* methods or forcefield models, it is possible to calculate the vibrational modes of a model system. In practice, the characteristic frequencies of particular materials are typically identified empirically, and the symmetry information and relative frequencies of models can be used to estimate the corresponding atomic movements.

In CZTS it has been found that exciting the system with several different laser frequencies is required in order to identify and rule out certain secondary phases.[19] This is not available in many laboratories and limits the confidence that can be achieved by "standard" Raman measurements. The situation is complicated by the fact that Raman spectroscopy is surface-sensitive, with a penetration depth of ∼100 nm — secondary phases are likely to form at

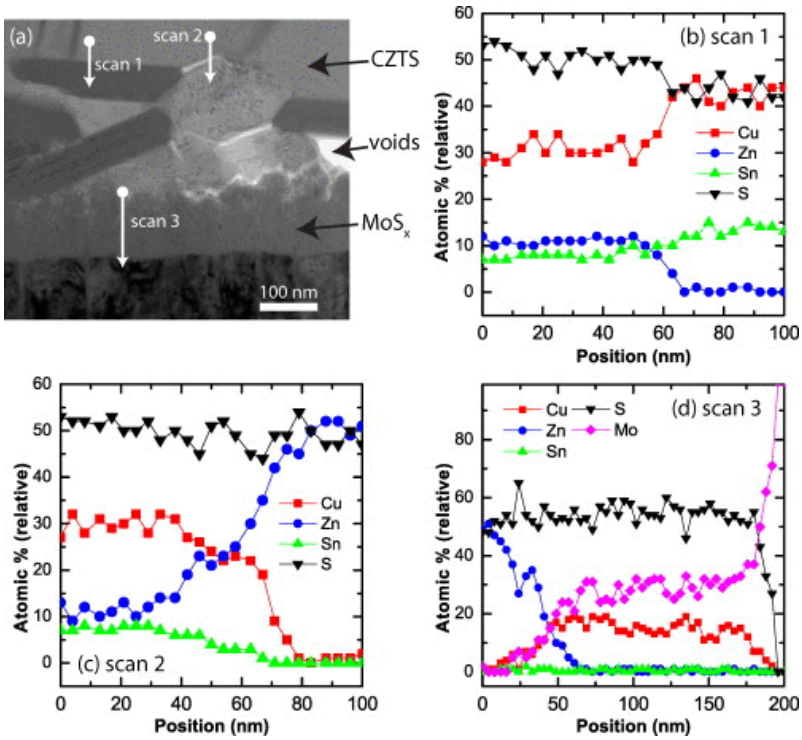

Figure 3.4 – Energy-dispersive spectroscopic (EDS) analysis of grain boundaries in Cu_2ZnSnS_4 deposited on Mo-coated soda-lime glass; Wang *et al.* (2011).[65] Original caption: "(a) Bright field image of CZTS/MoS interface. [(b)-(d)] The EDS elements analysis for three scans at different positions."

interfaces due to the presence of compositional gradients, in which case they will be over-represented in the Raman data.

Compositional analysis Several techniques are used which give information about the overall elemental composition of a region. This can be used to infer information about the constituent phases, but also possesses some ambiguity; for example, a 1 : 1 mixture of Cu_2SnS_3 and ZnS would have exactly the same elemental composition as Cu_2ZnSnS_4. In practice the presence of spatial variation would give away the presence of more than one phase. Detailed analysis with energy-dispersive spectroscopy (EDS) has been carried out for high-quality samples by researchers at IBM, identifying increases in Cu concentration at grain boundaries, as well as separation into ZnS and Cu_2SnS_3 at the Mo back contact (Fig. 3.4).[65] A 100 nm film was visible at this interface, rich in Cu, Mo and S. Compositional inhomogeneity has been noted in CZTSSe films from nanoparticles, characterised with electron microscopy and EDS.[82] In that study the effect of annealing was also interesting, leading to an *increase* in standard deviation of Cu/Zn content over different grains, while the deviation in Sn content rose and fell.

Atom probe tomography Results obtained by atom probe tomography (APT) are particularly concerning. This destructive technique samples a large fraction of atoms as they are evaporated from the surface in layers, providing near-atomic resolution. APT has not yet been applied to the sulfide CZTS, but the analysis of a small sample of CZTSe revealed intermixed, connected domains of several compositions with dimensions of the order 10 nm.[83] Behaviour at this length-scale would be invisible to more conventional analysis methods, making it difficult to determine whether these domains were a characteristic of this single sample or of kesterites in general. However those analysis methods such as EDS have also shown inhomogeneity on a larger length scale than that explored with a typical APT study; if typical samples are

inhomogeneous at multiple length scales then a complete characterisation will require multiple measurements.

Bibliography

[1] K. Ito and T. Nakazawa, *Jpn. J. Appl. Phys.*, 1988, **27**, 2094–2097.

[2] R. Nitsche, D. Sargent and P. Wild, *J. Cryst. Growth*, 1967, **1**, 52–53.

[3] H. Katagiri, N. Sasaguchi, S. Hando, S. Hoshino, J. Ohashi and T. Yokota, *Sol. Energy Mater. Sol. Cells*, 1997, **49**, 407–414.

[4] S. Schorr, H.-J. Hoebler and M. Tovar, *Eur. J. Mineral.*, 2007, **19**, 65–73.

[5] J. Paier, R. Asahi, A. Nagoya and G. Kresse, *Phys. Rev. B*, 2009, **79**, 1–8.

[6] S. Chen, X. G. Gong, A. Walsh and S.-H. Wei, *Appl. Phys. Lett.*, 2009, **94**, 041903.

[7] C. Persson, *J. Appl. Phys.*, 2010, **107**, 053710.

[8] S. Schorr, *Sol. Energy Mater. Sol. Cells*, 2011, **95**, 1482–1488.

[9] S. Hall, J. Szymanski and J. Stewart, *Can. Mineral.*, 1978, **16**, 131–137.

[10] G. P. Bernardini, P. Bonazzi, M. Corazza, F. Corsini, G. Mazzetti, L. Poggi and G. Tanelli, *Eur. J. Mineral.*, 1990, **2**, 219–226.

[11] T. Shibuya, Y. Goto, Y. Kamihara, M. Matoba, K. Yasuoka, L. A. Burton and A. Walsh, *Appl. Phys. Lett.*, 2014, **104**, 021912.

[12] S. Chen, A. Walsh, Y. Luo, J.-H. Yang, X. G. Gong and S.-H. Wei, *Phys. Rev. B*, 2010, **82**, 195203.

[13] T. K. Todorov, K. B. Reuter and D. B. Mitzi, *Adv. Mat.*, 2010, **22**, E156–9.

[14] D. A. R. Barkhouse, O. Gunawan, T. Gokmen, T. K. Todorov and D. B. Mitzi, *Prog. Photovoltaics*, 2012, **20**, 6–11.

[15] S. Bag, O. Gunawan, T. Gokmen, Y. Zhu, T. K. Todorov and D. B. Mitzi, *Energy Environ. Sci.*, 2012, **5**, 7060.

[16] M. T. Winkler, W. Wang, O. Gunawan, H. J. Hovel, T. K. Todorov and D. B. Mitzi, *Energy Environ. Sci.*, 2014, **7**, 1029–1036.

[17] W. Wang, M. T. Winkler, O. Gunawan, T. Gokmen, T. K. Todorov, Y. Zhu and D. B. Mitzi, *Adv. Energy Mater.*, 2014, **4**, 1–5.

[18] M. Moynihan, G. Zoppi, R. Miles and I. Forbes, 26th European Photovoltaic Solar Energy Conference and Exhibition, 2011, pp. 2916–2921.

[19] M. Dimitrievska, H. Xie, A. Fairbrother, X. Fontané, G. Gurieva, E. Saucedo, A. Pérez-Rodríguez, S. Schorr and V. Izquierdo-Roca, *Appl. Phys. Lett.*, 2014, **105**, 031913.

[20] L. Choubrac, A. Lafond, C. Guillot-Deudon, Y. Moëlo and S. Jobic, *Inorg. Chem.*, 2012, **51**, 3346–3348.

[21] S. Chen, X. G. Gong, A. Walsh and S.-H. Wei, *Appl. Phys. Lett.*, 2010, **96**, 021902.

[22] J. He, L. Sun, S. Chen, Y. Chen, P. Yang and J. Chu, *J. Alloys Compd.*, 2012, **511**, 129–132.

[23] A. Fairbrother, X. Fontané, V. Izquierdo-Roca, M. Espindola-Rodriguez, S. López-Marino, M. Placidi, J. López-García, A. Pérez-Rodríguez and E. Saucedo, *ChemPhysChem*, 2013, **14**, 1836–1843.

[24] J. M. Raulot, C. Domain and J. F. Guillemoles, *J. Phys. Chem. Solids*, 2005, **66**, 2019–2023.

[25] S. Adachi, in *Copper zinc tin sulphide-based thin film solar cells*, ed. K. Ito, John Wiley & Sons, Chichester, UK, 2015, ch. 7, pp. 149–179.

[26] J. Nelson, *The physics of solar cells*, Imperial College Press, London, 2003.

[27] P. K. Sarswat and M. L. Free, *J. Electron. Mater.*, 2012, **41**, 2210–2215.

[28] S. López-Marino, M. Neuschitzer, Y. Sánchez, A. Fairbrother, M. Espindola-Rodriguez, J. López-García, M. Placidi, L. Calvo-Barrio, A. Pérez-Rodríguez and E. Saucedo, *Sol. Energy Mater. Sol. Cells*, 2014, **130**, 347–353.

[29] S. López-Marino, Y. Sánchez, M. Espíndola-Rodríguez, X. Alcobé, H. Xie, M. Neuschitzer, I. Becerril, S. Giraldo, M. Dimitrievska, M. Placidi, L. Fourdrinier, V. Izquierdo-Roca, A. Pérez-Rodríguez and E. Saucedo, *J. Mater. Chem. A*, 2016.

[30] D. Meissner, *WO Pat.*, WO 2010000581 A2, 2010, Application PCT/EP2009/057,127.

[31] R. Mane and C. Lokhande, *Mater. Chem. Phys.*, 2000, **65**, 1–31.

[32] K. Wang, O. Gunawan, T. Todorov, B. Shin, S. J. Chey, N. A. Bojarczuk, D. Mitzi and S. Guha, *Appl. Phys. Lett.*, 2010, **97**, 95–98.

[33] D. B. Mitzi, M. Yuan, W. Liu, A. J. Kellock, S. J. Chey, L. Gignac and A. G. Schrott, *Thin Solid Films*, 2009, **517**, 2158–2162.

[34] M. T. Htay, Y. Hashimoto, N. Momose, K. Sasaki, H. Ishiguchi, S. Igarashi, K. Sakurai and K. Ito, *Jpn. J. Appl. Phys*, 2011, **50**, 132301.

[35] N. Sakai, H. Hiroi and H. Sugimoto, 2011 37th IEEE Photovoltaic Specialists Conference, 2011, pp. 003654–003657.

[36] A. Crovetto and A. Cazzaniga, *Pure-sulfide CZTS solar cells by pulsed laser deposition*, 2015, `http://orbit.dtu.dk/files/118850854/ancro_Poster_kesterites_2015_andcan_ancro.pdf`.

[37] D. Colombara, S. Delsante, G. Borzone, J. Mitchels, K. Molloy, L. Thomas, B. Mendis, C. Cummings, F. Marken and L. Peter, *J. Cryst. Growth*, 2013, **364**, 101–110.

[38] J. J. Scragg, P. J. Dale and L. M. Peter, *Electrochem. Commun.*, 2008, **10**, 639–642.

[39] S. Ahmed, K. B. Reuter, O. Gunawan, L. Guo, L. T. Romankiw and H. Deligianni, *Adv. Energy Mater.*, 2012, **2**, 253–259.

[40] P. A. Fernandes, P. M. P. Salomé and A. F. da Cunha, *Thin Solid Films*, 2009, **517**, 2519–2523.

[41] T. Ericson, T. Kubart, J. J. Scragg and C. Platzer-Björkman, *Thin Solid Films*, 2012, **520**, 7093–7099.

[42] A. Crovetto, A. Cazzaniga, R. B. Ettlinger, J. Schou and O. Hansen, *Thin Solid Films*, 2015, **582**, 203–207.

[43] N. Shinde, C. Lokhande, J. Kim and J. Moon, *J. Photochem. Photobiol., A*, 2012, **235**, 14–20.

[44] X. Lin, J. Kavalakkatt, M. C. Lux-Steiner and A. Ennaoui, *Adv. Sci.*, 2015, **2**, 1500028.

[45] Z. Su, C. Yan, K. Sun, Z. Han, F. Liu, J. Liu, Y. Lai, J. Li and Y. Liu, *Appl. Surf. Sci.*, 2012, **258**, 7678–7682.

[46] Q. Guo, H. W. Hillhouse and R. Agrawal, *J. Am. Chem. Soc.*, 2009, **131**, 11672–3.

[47] Q. Guo, G. M. Ford, W.-C. Yang, B. C. Walker, E. a. Stach, H. W. Hillhouse and R. Agrawal, *J. Am. Chem. Soc.*, 2010, 17384–17386.

[48] K. Kushiya, M. Tachiyuki and T. Kase, *US Pat.*, US6048442 A, 2000.

[49] S. Feldman-Peabody, S. Black, R. Gossman and P. O'keefe, *US Pat.*, US20140238849 A1, 2014, Application US 13/775,613.

[50] A. D. Collord, H. Xin and H. W. Hillhouse, *IEEE J. Photovolt.*, 2015, **5**, 288–298.

[51] H.-P. Zhou, W.-C. Hsu, H.-S. Duan, B. Bob, W. Yang, T.-b. Song, C.-J. Hsu and Y. Yang, *Energy Environ. Sci.*, 2013, **6**, 2822.

[52] Y. Zou, X. Su and J. Jiang, *J. Am. Chem. Soc.*, 2013, **135**, 18377–18384.

[53] A. Nagoya, R. Asahi, R. Wahl and G. Kresse, *Phys. Rev. B*, 2010, **81**, 113202.

[54] D. Huang and C. Persson, *Thin Solid Films*, 2013, **535**, 265–269.

[55] A. Lafond, L. Choubrac, C. Guillot-Deudon, P. Fertey, M. Evain and S. Jobic, *Acta Crystallogr., Sect. B: Struct. Sci., Cryst. Eng. Mater.*, 2014, **70**, 390–4.

[56] X. Fontané, V. Izquierdo-Roca, E. Saucedo, S. Schorr, V. Yukhymchuk, M. Valakh, A. Pérez-Rodríguez and J. Morante, *J. Alloys Compd.*, 2012, **539**, 190–194.

[57] J. J. S. Scragg, L. Choubrac, A. Lafond, T. Ericson and C. Platzer-Björkman, *Appl. Phys. Lett.*, 2014, **104**, 041911.

[58] B. G. Mendis, M. D. Shannon, M. C. Goodman, J. D. Major, R. Claridge, D. P. Halliday and K. Durose, *Prog. Photovolt: Res. Appl.*, 2014, **22**, 24–34.

[59] O. Gunawan, T. Gokmen and D. B. Mitzi, *J. Appl. Phys.*, 2014, **116**, 084504.

[60] I. L. Repins, H. Moutinho, S. G. Choi, A. Kanevce, D. Kuciauskas, P. Dippo, C. L. Beall, J. Carapella, C. DeHart, B. Huang and S. H. Wei, *J. Appl. Phys.*, 2013, **114**, 084507.

[61] C. Frisk, T. Ericson, S.-Y. Li, P. Szaniawski, J. Olsson and C. Platzer-Björkman, *Sol. Energy Mater. Sol. Cells*, 2015, **144**, 364–370.

[62] S. Chen, J.-H. Yang, X. G. Gong, A. Walsh and S.-H. Wei, *Phys. Rev. B*, 2010, **81**, 245204.

[63] M. Grossberg, J. Krustok, T. Raadik, M. Kauk-Kuusik and J. Raudoja, *Curr. Appl. Phys.*, 2014, **14**, 1424–1427.

[64] J. J. S. Scragg, J. K. Larsen, M. Kumar, C. Persson, J. Sendler, S. Siebentritt and C. Platzer Björkman, *Phys. Status Solidi B*, 2015, [In Press].

[65] K. Wang, B. Shin, K. B. Reuter, T. Todorov, D. B. Mitzi and S. Guha, *Appl. Phys. Lett.*, 2011, **98**, 051912.

[66] J. Just, D. Lützenkirchen-Hecht, R. Frahm, S. Schorr and T. Unold, *Appl. Phys. Lett.*, 2011, **99**, 262105.

[67] A. Redinger, D. M. Berg, P. J. Dale, R. Djemour, L. Gütay, T. Eisenbarth, N. Valle and S. Siebentritt, *IEEE J. Photovolt.*, 2011, **1**, 200–206.

[68] D. B. Mitzi, O. Gunawan, T. K. Todorov, K. Wang and S. Guha, *Sol. Energy Mater. Sol. Cells*, 2011, **95**, 1421–1436.

[69] B.-A. Schubert, B. Marsen, S. Cinque, T. Unold, R. Klenk, S. Schorr and H.-W. Schock, *Prog. Photovolt: Res. Appl.*, 2011, **19**, 93–96.

[70] G. Suresh Babu, Y. B. Kishore Kumar, P. Uday Bhaskar and S. Raja Vanjari, *Sol. Energy Mater. Sol. Cells*, 2010, **94**, 221–226.

[71] T. Tanaka, T. Sueishi, K. Saito, Q. Guo, M. Nishio, K. M. Yu and W. Walukiewicz, *J. Appl. Phys.*, 2012, **111**, 53522–53524.

[72] P. Zawadzki, L. L. Baranowski, H. Peng, E. S. Toberer, D. S. Ginley, W. Tumas, A. Zakutayev and S. Lany, *Appl. Phys. Lett.*, 2013, **103**, 1–6.

[73] L. A. Burton and A. Walsh, *J. Phys. Chem. C*, 2012, **116**, 24262–24267.

[74] H. Xie, Y. Sánchez, S. López-Marino, M. Espíndola-Rodríguez, M. Neuschitzer, D. Sylla, A. Fairbrother, V. Izquierdo-Roca, A. Pérez-Rodríguez and E. Saucedo, *ACS Appl. Mater. Interfaces*, 2014, 12744–12751.

[75] A. Weber, R. Mainz, H. W. Schock and I. I. Experimental, *J. Appl. Phys.*, 2010, **107**, 013516.

[76] A. Redinger, D. M. Berg, P. J. Dale and S. Siebentritt, *J. Am. Chem. Soc.*, 2011, **133**, 3320–3.

[77] J. J. Scragg, T. Ericson, T. Kubart, M. Edoff and C. Platzer-Björkman, *Chem. Mater.*, 2011, **23**, 4625–4633.

[78] C. Zou, L. Zhang, D. Lin, Y. Yang, Q. Li, X. Xu, X. Chen and S. Huang, *CrystEngComm*, 2011, **13**, 3310.

[79] P. A. Fernandes, P. M. P. Salomé and A. F. da Cunha, *J. Phys. D: Appl. Phys.*, 2010, **43**, 215403.

[80] M. Onoda, X.-A. Chen, A. Sato and H. Wada, *Mater. Res. Bull.*, 2000, **35**, 1563–1570.

[81] O. Madelung, *Semiconductors: Data Handbook*, Springer-Verlag, Berlin, 3rd edn., 2004.

[82] K. E. Roelofs, Q. Guo, S. Subramoney and J. V. Caspar, *J. Mater. Chem. A*, 2014, **2**, 13464–13470.

[83] T. Schwarz, O. Cojocaru-Mirédin, P. Choi, M. Mousel, A. Redinger, S. Siebentritt and D. Raabe, *Appl. Phys. Lett.*, 2013, **102**, 042101.

Part II

Theory and methodology

Chapter 4

Density functional theory

Citations in the text refer to specific quotes and papers of historical interest. Many excellent books cover the fundamental equations, methods and details discussed in this section; a selection are recommended as Refs. 1–4.

4.1 *Ab initio* fundamentals: the Hartree–Fock method

Ab initio chemistry attempts to describe chemical systems by working up from fundamental physics, rather than down from experimental measurements. Of foremost significance is the eigenvalue problem presented by the time-independent Schrödinger equation

$$\mathscr{H}\Psi = E\Psi \tag{4.1}$$

where $\mathscr{H}$ is a Hamiltonian operator incorporating kinetic and potential energy terms, Ψ is the system wavefunction and E the system energy.[5;6] Two assumptions are made immediately and widely:

ASSUMPTION

- The reconfiguration of electronic structure is considered to be instantaneous relative to the movements of nuclei. Nuclei are considered to be stationary relative to the movement of electrons.
- Only electronic forces and kinetic energy are of interest; gravity and the strong and weak nuclear forces may be safely neglected.

The first assumption is known as the Born–Oppenheimer approximation and is generally satisfactory given that the mass of a proton is ~ 2000 times the mass of an electron. It allows electrons and nuclei to be treated separately, greatly simplifying the problem. The second assumption may be considered a dividing line between fundamental physics and chemical physics; processes that are observable in chemistry are dominated by electrostatics. It is a welcome simplification, especially given the current absence of a standard model for quantum gravity.

Returning to (4.1), the wavefunction under consideration is therefore that of the system's electrons, and the energy is the total energy of the electrons. In principle it is quite simple to account for the electrostatic forces on an electron; the fundamental interactions are well-understood. However, the quantum mechanical problem becomes a large set of coupled non-linear equations as more electrons are added, and we lack adequate mathematical tools for such systems. This is widely referred to as the "many-body problem".

In order to avoid the many-body problem, many quantum chemistry techniques employ the "Hartree approximation":

ASSUMPTION The multi-electron wavefunction may be approximated as a set of one-electron wavefunctions.

This is the first key approximation behind the Hartree–Fock (HF) method.[7;8] The corresponding model of atomic and molecular orbitals, each occupied by up to two electrons, is widely used to describe and understand chemical bonding. These orbitals are simply degenerate pairs of one-electron wavefunctions. Having made the Hartree approximation, we consider the next key assumption:

ASSUMPTION Each electron responds to an average field of other independent electrons.

This is the "mean field approximation". The one-electron wavefunctions are treated as independent of each other, but all interacting with an average field. Mathematically, this type of problem lends itself well to iterative solution methods. The system is solved when the field generated by the electronic states is equal to the field used to predict those states — a "self-consistent field" (SCF). In order to treat the eigenvalue problem with conventional linear algebra, the one-electron wavefunctions ψ_i are treated as linear combinations of a restricted set of mathematical functions — the *basis set*. While in principle the use of basis functions is a mathematically exact technique, by restricting it to a predefined basis set we make one more assumption:

ASSUMPTION The selected basis set allows for the construction of functions which are sufficiently close to the exact solution.

The symbol $\mathbf{\Phi}$ is used here to represent this basis-set description of the set of one-electron wavefunctions. While we have ruled out the ability to describe the wavefunctions fully (except in the unlikely event that they coincide with our choice of basis set), the technique is still "exact" in that it gives correct expectation values for regions of space defined by the basis set.

Two further constraints are applied to the formation of an acceptable set of wavefunctions: orthonormality and antisymmetry. These are both motivated by fundamental physics. The solution of Eq. (4.1) for the constructed Hamiltonian $\mathscr{H}$ is equivalent to finding the eigenvalues ϵ_i and corresponding eigenvectors Ψ_i of $\mathscr{H}$, which are the energy states available to electrons and their corresponding one-electron wavefunctions. The Hamiltonian must be a Hermitian matrix (due to the way it is constructed), and it is a mathematical property of Hermitian matrices that their eigenfunctions are orthogonal.[†] The Hermitian nature of $\mathscr{H}$ also guarantees that the eigenvalues will be real.

$$(\epsilon_i - \epsilon_j) \int \Psi_i^* \Psi_j \mathrm{d}\mathbf{r} = 0. \tag{4.2}$$

(The * indicates a complex conjugate.) As each state is capable of holding one electron, the overall expectation value should be normalised to 1:

$$\int \left|\Psi_i\right|^2 \mathrm{d}\mathbf{r} = 1. \tag{4.3}$$

[†]A Hermitian matrix is a matrix that is equal to its complex conjugate with the rows and columns exchanged: $A = (A^*)^{\mathrm{T}}$ where $(A^{\mathrm{T}})_{ij} = A_{ji}$.

These conditions are elegantly combined as the condition of orthonormality,

$$\int \Psi_i^* \Psi_j \mathrm{d}\mathbf{r} = \delta_{i,j}, \tag{4.4}$$

where $\delta_{i,j}$ is the Kronecker delta function with respect to i and j. Full multi-electron wavefunctions are antisymmetric with respect to the exchange of two electrons, i.e.

$$\Psi(\dots, \mathbf{r}_1, \mathbf{r}_2, \dots) = -\Psi(\dots, \mathbf{r}_2, \mathbf{r}_1, \dots) \tag{4.5}$$

where $\mathbf{r}_i$ is a vector representing the position and spin of a given electron. This constraint implements the Pauli exclusion principle; if two electrons are described with the same set of quantum numbers then Ψ becomes zero, which fails to satisfy orthonormality. The scheme for implementing this constraint with basis functions was developed by J. C. Slater, taking advantage of the well-known sign-changing property of matrix determinants.[9] The Hartree–Fock method then describes a set of operators acting on the single-electron wavefunction ψ_a,

$$\left[\hbar + \sum_{b \neq a} \mathscr{J}_b - \sum_{b \neq a} \mathscr{X}_b \right] \psi_a = \epsilon_a \psi_a, \tag{4.6}$$

where: $\hbar$ is the one-electron Hamiltonian containing the independent kinetic energy and external potential energy (typically with respect to nuclei); $\mathscr{J}_b$ is the Coulomb operator (electrostatic potential) with respect to another electron b; $\mathscr{X}_b$ is the *exchange* operator with respect to electron b; ϵ_a is the energy associated with this single-electron state. Electron exchange can be thought of as a repulsive effect driven by the Pauli exclusion principle; the expectation value for electrons is reduced near other electrons with the same spin. As the electrostatic potential is based on a probability-weighted volume integral, this manifests itself as a negative correction to the Coulomb energy.

In order to solve the entire system, some approach is needed to solve a set of wavefunctions $\mathbf{\Phi}$ simultaneously. The variational principle is employed to find the best possible set of wavefunctions given the basis set:

$$E_{\mathbf{\Phi}_{\text{trial}}} \geq E_0. \tag{4.7}$$

The actual ground state is the solution with the lowest possible energy E_0, obtained by summing the eigenvalues ϵ of occupied orbitals. By using a number of trial functions $\mathbf{\Phi}_{\text{trial}}$ with a suitable iterative method, we can converge to ever decreasing, and hence increasingly accurate, energies.

4.2 Density-functional theory: principles

The fatal weakness of the pure Hartree–Fock method lies in the mean field approximation. In practice the way electrons contribute to the electrostatic field is not independent: they are *correlated*. An excellent analogy is given by Szabo and Ostlund (1989):[1]

> An example of correlated probabilities is provided by 2 hot potatoes and 2 cold apples in a bucket. The probability of obtaining a hot potato upon randomly withdrawing an object from the bucket (1/2) is not equal to the product of the probability of getting a hot object (1/2) times the probability of getting a potato (1/2), since whether the object is hot is perfectly correlated with whether the object is a potato.

A suitable Hamiltonian for the time-independent Schrödinger equation (4.1) might take the form

$$\mathscr{H}\Psi = \left(-\frac{1}{2}\nabla^2 + \mathscr{U}_{\text{ext}} + \mathscr{U}_{\text{H}} + \mathscr{U}_{\text{X}} + \mathscr{U}_{\text{C}} \right) \Psi, \tag{4.8}$$

where the $\mathscr{U}$ operators give the potential energy contributions of the external potential, Hartree (mean-field) potential, exchange and correlation corrections, respectively. The total energy is commonly divided in an analogous way:

$$E = E_{\text{kinetic}} + E_{\text{ext}} + E_{\text{H}} + E_{\text{X}} + E_{\text{C}}. \tag{4.9}$$

Even though we wish to account for correlation interactions, some kind of analysis in aggregate is essential to avoid the many-body problem. The breakthrough came from Hohenberg and Kohn in 1964: the presence of all the electrons can be treated as an overall field of electron density $\rho(\mathbf{r})$.[10] The electron density is the field of expected electron occupancy, which is equivalent to the sum of the densities of one-electron spin orbitals

$$\rho(\mathbf{r}) = \sum_i \left|\psi_i(\mathbf{r})\right|^2 = \sum_i \left|\phi_i(\mathbf{r})\right|^2 \tag{4.10}$$

where ψ_i represents a fictitious one-electron wavefunction and ϕ_i represents an occupied 'orbital' within the basis set. Every many-body wavefunction Ψ yields a unique electron density field and hence no information is lost by moving to a density-based description. Every ground-state property is therefore solely dependent on the electron density. This does not tell us *how* to compute the density or properties, but it is possible to solve for an 'inhomogeneous electron gas' by numerical (or in rare cases analytical) methods and relate other systems to these known results. This process was built on by Kohn and Sham in 1965, taking the Hartree–Fock format to form a self-consistent expression,[11]

$$\left(-\frac{1}{2}\nabla^2 + \left[\mathscr{U}_{\text{ext}}(\mathbf{r}) + \mathscr{U}_{\text{H}}(\mathbf{r}) + \mathscr{U}_{\text{XC}}(\rho(\mathbf{r}))\right]\right)\phi_i(\mathbf{r}) = \epsilon_i\phi_i(\mathbf{r}), \tag{4.11}$$

for each single-electron wavefunction ϕ_i.

In this context these wavefunctions are referred to as "Kohn–Sham orbitals", and the system may be solved to obtain the ground state by using sets of trial wavefunctions and employing the variational principle as in the Hartree–Fock method. It is important to note that Kohn–Sham orbitals do not need to resemble conventional chemical orbitals; they can be any set of functions that give a satisfactory solution. In calculations on periodic systems, it is common for the basis set to consist of a large number of plane waves; individually these are very abstract, but together they form a computationally efficient basis which returns chemically reasonable density fields when Eq. (4.10) is applied.

The Kohn–Sham method is not purely based on electron density (as Hohenberg and Kohn suggested was possible), but replaces the difficult wavefunction operators $\mathscr{U}_{\text{X}}$ and $\mathscr{U}_{\text{C}}$ with a single "exchange-correlation" functional of the electron density, $\mathscr{U}_{\text{XC}}(\rho(\mathbf{r}))$. This can be approximated by fitting to data or analytically solving for analogous, simplified systems such electron gases. It is the use of such operators which distinguishes "density-functional theory" (DFT) from other *ab initio* methods. While in practice the construction of a suitable exchange-correlation functional is difficult, it remains theoretically possible to construct a perfect exchange-correlation functional. In this case, DFT would be an exact technique and there are no inherent errors that arise from the use of basis sets or the variational principle.

4.3 Density-functional theory: implementation

4.3.1 Exchange-correlation functionals

Assuming well-written computer code, the design of an exchange-correlation (XC) functional is the key factor determining the comparative accuracy, reliability and cost of DFT calculations. In

2001 Perdew proposed a "Jacob's ladder"* of density functionals, stretching from the "Hartree world" of totally non-interacting electrons to "chemical accuracy" (generally considered to be around 1 kcal $\cdot$ mol^{-1} $\sim$ 4 kJ mol^{-1}).[12] Over time some steps have been added or renamed, but the overall analogy and goal have endured, and research continues towards accurate, affordable methods.

The simplest family of XC functionals are those which employ the 'local density approximation' (LDA) or 'local spin-density approximation' (LSDA). These are essentially the same method, applied either to a total density or two separate 'spin densities'; the latter option is needed for spin-polarised systems. In L(S)DA the magnitude of exchange and correlation at a given point $\mathbf{r}$ is based purely on the 'local' density – that is to say the density of electrons at that point. The values are obtained from theoretical models of uniform electron gases; usually these are fitted to Ceperley and Alder's 1980 work.[13] An important review of correlation energy for use with LDA implementations was carried out by Vosko *et al.*, providing a useful parameterisation (VWN) of the Ceperley–Alder data from Monte Carlo calculations.[14] The LDA is most appropriate for systems with slowly varying density and has enjoyed great success when applied to metals, where the conducting electrons are widely distributed.

The next level of accuracy comes from 'gradient-corrected' functionals. These incorporate not only the local density $\rho(\mathbf{r})$, but also the density gradient $\nabla\rho(\mathbf{r})$. These may be formed from first principles, fitting or some combination of both. Functionals which use local gradients with cutoff regions in order to model chemical systems are said to use the "generalised gradient approximation" (GGA). The most demanding level of theory applied in this work is DFT with hybrid XC functionals, which incorporate a portion of HF exchange. While ultimately a form of error cancellation, this approach has led to impressive levels of accuracy at a fraction of the cost of higher-level methods. The GGA functional PBE and hybrid functional B3LYP are used in thousands of scientific papers each year.[15]

Due to the use of fitting in many exchange-correlation functionals, DFT is not considered a truly *ab initio* technique by some purists. This lively debate raises a significant concern around fitting and validity. Nonetheless, in this work the term "*ab initio*" is understood to include DFT, in order to contrast quantum chemical methods with purely fitted analytical potentials or experimental work.

PBE and PBEsol

The Perdew–Burke–Ernzerhof (PBE) functional was introduced by an enticingly-titled paper as the *Generalised Gradient Approximation Made Simple*.[16] The authors rejected the semi-empirical approach of some alternative XC functionals within the GGA, finding that while effective for molecules they behaved poorly when applied to metals. Instead they used a truncated first-principles expansion following the approach of the earlier "PW91" functional, avoiding parameterisation in favour of expressions using fundamental physical constants. The only exception is the LDA contribution, which follows the standard (VWN) parameterisation in most implementations. The resulting functional is smooth as there are no transitions between fitting regions, and highly transferable as the development was not based on fitting to a particular set of systems. PBE addressed some of the concerns about the application of GGAs to periodic systems with delocalised electrons, but was found to somewhat under-bind atoms and hence overestimate bond lengths. In contrast, the LDA tends to over-bind.[17]

PBEsol is a modern (2008) exchange-correlation functional using the generalised gradient approximation (GGA), and is the functional most heavily employed in this work.[17] It is closely related to PBE, and has performed well in 'shoot-out' comparisons of available functionals, offering good accuracy without the scaling difficulties of higher-'rung' functionals such as

*From the original caption: "Any resemblance to the Tower of Babel is purely coincidental."

hybrids.[16;18;19] The nature of PBEsol was, again, captured well by the original article title: *Restoring the Density-Gradient Expansion for Exchange in Solids and Surfaces*. In practice the choice of truncation for PBE was somewhat biased towards the study of atoms and neglected the density gradient contribution to exchange. The term is less problematic in systems with slowly-varying densities (i.e. solids and surfaces) and improves the accuracy of calculations for these systems. This gives the PBEsol XC-functional more 'LDA-like' behaviour, and results tend to fall between those from PBE and LDA-based calculations.

Hybrid DFT

Hybrid functionals mix GGA with a portion of HF exact exchange in order to achieve more accurate total energies, with an arrangement such as

$$E_{\mathrm{XC}}^{\mathrm{Hybrid}} = E_{\mathrm{XC}}^{\mathrm{GGA}} + a(E_{\mathrm{X}}^{\mathrm{HF}} - E_{\mathrm{X}}^{\mathrm{GGA}}). \tag{4.12}$$

For such single-parameter correlations, the value of the parameter a is usually 25 %. PBE0 uses this construction, with the PBE functional as its GGA component.[16;20]

B3LYP is somewhat controversial; the *de facto* standard implementation lies in the closed-source code GAUSSIAN, and comparison with other codes is heavily restricted. Nonetheless, the name and user manual suggest that it employs the exchange part of Becke's 3-parameter functional, with the correlation energy calculations of Lee, Yang and Parr.[21;22] The LDA contribution appears to be drawn from the VWN paper but, rather than use the recommended fit to the Ceperley–Alder data, B3LYP implementations tend to use the parameterisation of deprecated correlation energies from the Random Phase Approximation.

The Heyd–Scuseria–Ernzerhof (HSE) method was introduced in order to reduce the cost of hybrid DFT calculations for solids and large molecules and, after some initial confusion and an erratum, has become a popular approach.[23;24] ("HSE03" is sometimes used to refer to calculations with the parameters reported initially, while "HSE06" refers to the recommended parameters.) The problem approached by HSE is that the exchange energy converges slowly over a long distance. The associated computational cost can be reduced by calculating only the short-range exchange energy with the HF procedure, while an inexpensive GGA functional is employed over the whole calculation region. The Coulomb potential is separated by range

$$\frac{1}{r} = \underbrace{\frac{\mathrm{erfc}(\omega r)}{r}}_{\text{Short-range}} + \underbrace{\frac{\mathrm{erf}(\omega r)}{r}}_{\text{Long-range}} \tag{4.13}$$

$$E_{xc}^{\mathrm{HSE}} = aE_x^{\mathrm{HF,SR}}(\omega) + (1-a)E_x^{\mathrm{PBE,SR}}(\omega) + E_x^{\mathrm{PBE,LR}}(\omega) + E_c^{\mathrm{PBE}}; \tag{4.14}$$

the approximation being made is that

$$E_x^{\mathrm{HF,LR}}(\omega) \approx E_x^{\mathrm{PBE,LR}}(\omega). \tag{4.15}$$

According to the authors, "these terms tend to cancel each other".[23] It can readily be seen that as $\omega \to 0$, the XC functional approaches PBE0, while as $\omega \to \infty$, it approaches PBE. The recommended value of ω is 0.11 ${r_{\mathrm{Bohr}}}^{-1}$, and no claim was made by the authors that HSE06 would give more realistic results than PBE0. A sensitivity analysis suggests that while many properties are quite insensitive to reductions in ω below the recommended value, HSE06 lies close to an a-dependent optimal value of ω which out-performs PBE0 for predicting the bandgaps of semiconductors.[25]

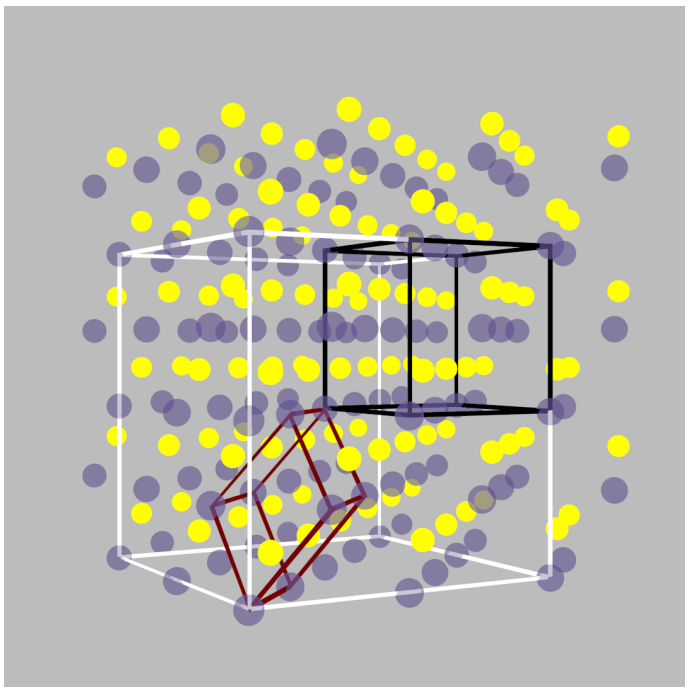

Figure 4.1 – Illustrated region of the periodic structure of zincblende (● Zn; ○ S), showing conventional (black) and primitive (red) unit cells as well as a $2 \times 2 \times 2$ supercell (white).

4.3.2 Periodic boundary conditions

It is not feasible to compute the properties of macroscopic materials through explicit treatment of every electron in the system. In the study of condensed matter, however, we may take advantage of the *crystalline* nature of many interesting materials. Crystalline materials are characterised by a repeating *unit cell* located on the points of a three-dimensional *Bravais lattice*. The geometric arrangement of atoms in a macroscopic solid is therefore approximately described by the positions of atoms in a unit cell, and the set of lattice vectors $\mathbf{a}_i$ describing the Bravais lattice of all periodic images

$$\mathbf{R} = n_1\mathbf{a}_1 + n_2\mathbf{a}_2 + n_3\mathbf{a}_3 \tag{4.16}$$

where $\{n_1, n_2, n_3\} \subset \mathbb{Z}$. The key property of a Bravais lattice is that it is unchanged when translated by the lattice vectors; if the positions of its contents are denoted $\mathbf{r}$ then

$$\mathbf{r} + \mathbf{R}_i = \mathbf{r} \tag{4.17}$$

for any element i of the Bravais lattice. Large unit cells may contain multiple points on the Bravais lattice, and overlap with some of their translated images. This includes arrangements such as the face-centred cubic structure which are important in crystallography. Such cells can however always be reduced to a "primitive cell" which does not overlap with its images. (For an example, see Fig. 4.1.) It is often more computationally efficient to work with primitive cells as they reduce the size of the problem; however, the use of symmetry operations can allow for substantial savings in high-symmetry unit cells.

The periodic boundary model has some limitations in that the system is considered to be infinitely large and defect-free. If interfaces and defects are of interest these may be examined through "slab" and "supercell" models. In "slab" calculations, a wafer consisting of a minimal number of atomic layers is simulated with infinite periodicity in two dimensions. Many electronic structure codes are not capable of disabling periodic effects in the remaining dimension and a large vacuum gap must be inserted in between the layers. An analogous 1-dimensional approach is taken for the study of structures such as nanorods. In "supercell" calculations,

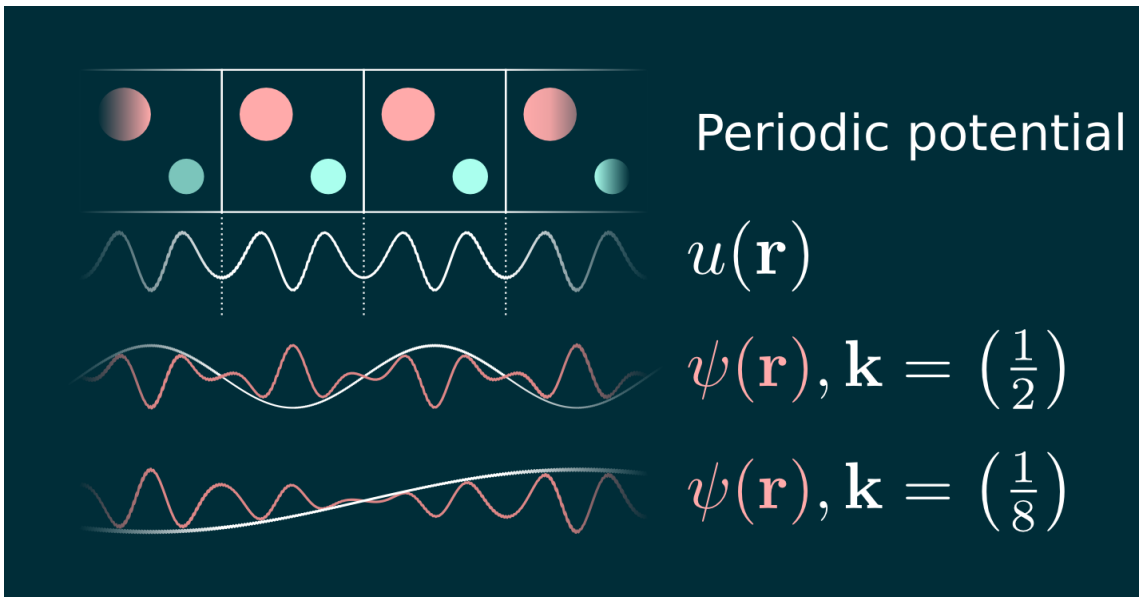

Figure 4.2 – Illustration of Bloch's theorem. A set of single-particle wavefunctions in a periodic system (top row) is the product of a periodic function $u(\mathbf{r})$ (second row, indicated as a 1-D function with dotted periodic boundaries) and plane waves corresponding to the full reciprocal lattice. Two 1-D Brillouin zone wave vectors $e^{i\mathbf{kr}}$ are illustrated (white lines, bottom two rows) with the resulting wavefunctions $\psi_{\mathbf{k}} = u(\mathbf{r}) \cdot e^{i\mathbf{kr}}$ (pink lines).

the modelling region consists of multiple crystallographic unit cells and contains some local imperfection; the relatively large dimensions of the supercell limit the effect of the nonphysical periodic interactions between the sites of interest.

According to Bloch's theorem, the wavefunction of a particle in a periodic potential has the useful property that all the ground-state eigenvectors consist of a combination of

(a) one shared function $u(\mathbf{r})$ with the periodicity of the Bravais lattice, and

(b) a plane wave, $e^{i\mathbf{kr}}$.

This is illustrated in Fig. 4.2.

ASSUMPTION The many-electron system in a crystalline material is adequately described as a set of Bloch waves. The resulting wavefunction for an electron occupying band n with wave vector $\mathbf{k}$ is

$$\phi_{n,\mathbf{k}} = u_n(\mathbf{r}) \cdot e^{i\mathbf{kr}}. \tag{4.18}$$

Bloch's theorem is exact, and the limitations of this approach lie in the previous assumptions (independent electron wavefunctions on an infinite lattice.)

The *reciprocal lattice* is the set of all wave vectors $\mathbf{K}$ such that

$$e^{i\mathbf{K}(\mathbf{r}+\mathbf{R})} = e^{i\mathbf{Kr}}, \tag{4.19}$$

forming a set of plane waves related to the Bravais lattice. As such, while the electronic wave vector $\mathbf{k}$ can be any vector in reciprocal space, we only need to sample the vectors (or $\mathbf{k}$-*points*) in a single unit cell. Conventionally the region used is the smallest repeating unit cell about the origin of the reciprocal lattice, known as the *Brillouin zone*.

With the wavefunctions expressed as Bloch waves, crystals can be studied with the HF method and DFT by finding the periodic function which minimises the total energy in a normalised sum over all $\mathbf{k}$-point vectors. In practice, a finite set of $\mathbf{k}$-points is used for approximate integration

over the Brillouin zone. The selection of a suitable set of **k**-points for inexpensive, accurate electronic structure calculations is an important problem. The most popular approach is the Monkhorst-Pack method of equally-spaced grids of points in reciprocal space.[26] A significant advantage of this method is that it leads to a simple means of systematically improving the calculation by increasing the density of this grid. The convergence of calculated properties with **k**-point grid density is system-dependent, and the appropriate density should be determined when studying any new system. In general, small unit cells and metallic systems require more **k**-points. In this work we adopt the formalism of Moreno and Soler, in which the grid density is characterised by a "cutoff" length corresponding to the dimensions of a hypothetical supercell which is sampled by a single **k**-point.[27] One key decision is whether to include the origin in reciprocal space (the Γ point); as a high-symmetry site the Γ point always represents some kind of local extreme in the band structure, and its inclusion may lead to slower convergence compared with an off-Γ grid. However, the electronic structure at Γ is generally of interest for the same reasons, and often includes the CBM and/or VBM. In high-symmetry systems it is possible to substantially reduce the number of **k**-points required by accounting for equivalent reciprocal-space sites in a weighted sum. Even in low-symmetry crystal structures, time-reversal symmetry may be used to reduce the cost by up to a factor of 2 (provided that it is not broken by magnetic effects).

Gaussian broadening is typically applied to the calculated electronic occupation levels at each step of the SCF calculation. This helps to stabilise the iterative procedure. Typically, small amounts of broadening of the order 0.01 eV are applied for calculations of insulating and semiconducting materials, while broadening of the order 0.1 eV is required for metallic systems.

4.3.3 Core electrons

The inner or *core* electron shells about a nucleus only interact weakly with the outer *valence* shells, which are involved in bonding. The number of electrons in an electronic structure calculation, and hence the computational cost, is reduced by replacing these core electrons with an effective potential or *pseudopotential* which emulates a screened nucleus. The implementation details of this can be quite complex; the generation of high-quality pseudopotentials is critical for such calculations and it is necessary to select an appropriate number of valence shells for the chemical problem at hand. The majority of DFT calculations in this project were "all-electron", side-stepping this issue. However, some calculations were performed with the projector augmented wave (PAW) method as implemented in the Vienna Ab Initio Simulations Package (VASP).[28;29] This approach combines pseudopotentials with a plane-wave basis set for efficient computations. VASP is distributed with a selection of *norm-conserving* and *ultrasoft* pseudopotentials. Ultrasoft pseudopotentials do not formally maintain the correct charge density but, if carefully constructed, can produce the same quality of results as norm-conserving pseudopotentials while using a smaller basis set.[30]

4.3.4 Structure optimisation

The hypothetical universe governed by any known XC functional or forcefield model has slightly different potential wells from reality. As a result, the equilibrium bond-lengths of a substance cannot simply be drawn from experimental measurements. In computational chemistry it is good practice to always optimise structures: in cluster calculations the positions of the nuclei are arranged to minimise the total energy and forces, while in periodic calculations it is also necessary to adjust the lattice parameters. Most properties of interest will be significantly affected by an imposed non-equilibrium structure; for example, the electronic structure of CZTS is very sensitive to the positions of the S ions which can lead to poor prediction of E_g even where the lattice parameters are well-converged.[31;32]

Highly symmetric systems have a limited number of degrees of freedom and it can be efficient to optimise them by fitting a relationship between these variables and the total energy — an equation of state. However, this is infeasible both for the more complex materials which are routinely encountered in materials science and for all but the simplest molecular systems. A typical *ab initio* study therefore consists of nested loops, illustrated in Fig. 4.3 on the facing page, in which the electronic structure is solved by an iterative method and this energy feeds an iterative geometry-optimisation procedure. For many energy-calculation procedures (including Kohn–Sham DFT with LDA and GGA functionals) the first derivatives in the potential energy surface, i.e. the forces on atoms, are directly available. The preferred geometry optimisation algorithms are therefore iterative quasi-Newtonian and conjugate-gradient methods. These use successive steps to reach the minimum of a repeatedly updated quadratic model of the potential energy surface. The degree of convergence is estimated from the difference between successive steps, with some acceptable threshold set for the total energy and the forces on atoms.

Bibliography

[1] A. Szabo and N. S. Ostlund, *Modern Quantum Chemistry: Introduction to Advanced Electronic Structure Theory*, McGraw-Hill, New York, 1st edn., 1989.

[2] J. G. Lee, *Computational Materials Science: An Introduction*, CRC Press, 2012.

[3] P. Atkins and J. de Paula, *Atkins' Physical Chemistry*, Oxford University Press, Oxford, 8th edn., 2006.

[4] C. J. Cramer, *Essentials of Computational Chemistry: Theories and Models*, John Wiley & Sons, Chichester, 2nd edn., 2004.

[5] E. Schrödinger, *Phys. Rev.*, 1926, **28**, 1049–1070.

[6] E. Schrödinger, *Annalen der Physik*, 1926, **384**, 361–376.

[7] D. R. Hartree and W. Hartree, *Proc. R. Soc. London, Ser. A*, 1935, **150**, 9–33.

[8] J. C. Slater, *Phys. Rev.*, 1951, **81**, 385–90.

[9] J. C. Slater, *Phys. Rev.*, 1929, **34**, 1293–1322.

[10] P. Hohenberg and W. Kohn, *Phys. Rev. B*, 1964, **136**, 864–871.

[11] W. Kohn and L. Sham, *Phys. Rev. A*, 1965, **140**, 1133–1138.

[12] J. P. Perdew, *AIP Conf. Proc.*, 2001, **577**, 1–20.

[13] D. M. Ceperley and B. Alder, *Phys. Rev. Lett.*, 1980, **45**, 566–569.

[14] S. H. Vosko, L. Wilk and M. Nusair, *Can. J. Phys.*, 1980, **58**, 1200–1211.

[15] K. Burke, *J. Chem. Phys.*, 2012, **136**, 150901.

[16] J. P. Perdew, K. Burke and M. Ernzerhof, *Phys. Rev. Lett.*, 1996, **77**, 3865–3868.

[17] J. Perdew, A. Ruzsinszky, G. Csonka, O. Vydrov, G. Scuseria, L. Constantin, X. Zhou and K. Burke, *Phys. Rev. Lett.*, 2008, **100**, 136406.

[18] G. Csonka, J. Perdew, A. Ruzsinszky, P. Philipsen, S. Lebègue, J. Paier, O. Vydrov and J. Ángyán, *Phys. Rev. B*, 2009, **79**, 155107.

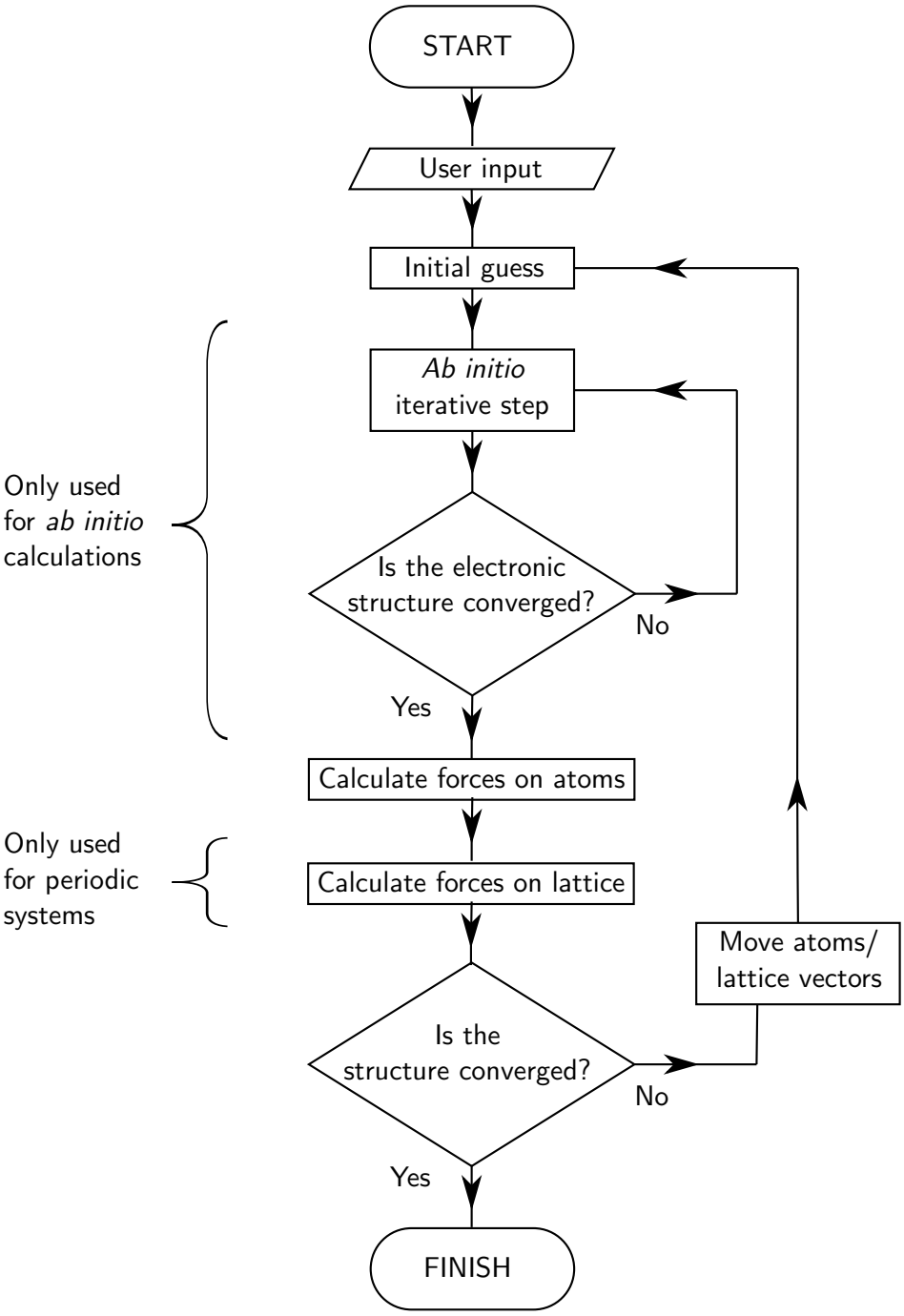

Figure 4.3 – Illustration of the nested iterative methods in a typical computational chemistry work-flow.

[19] M. De la Pierre, R. Orlando, L. Maschio, K. Doll, P. Ugliengo and R. Dovesi, *J. Comput. Chem.*, 2011, **32**, 1775–84.

[20] C. Adamo and V. Barone, *J. Chem. Phys.*, 1999, **110**, 6158.

[21] A. Becke, *J. Chem. Phys.*, 1993, **98**, 5648–5652.

[22] C. Lee, W. Yang and R. G. Parr, *Phys. Rev. B*, 1988, **37**, 785–789.

[23] J. Heyd, G. E. Scuseria and M. Ernzerhof, *J. Chem. Phys.*, 2003, **118**, 8207–8215.

[24] A. V. Krukau, O. A. Vydrov, A. F. Izmaylov and G. E. Scuseria, *J. Chem. Phys.*, 2006, **125**, 224106.

[25] J. E. Moussa, P. A. Schultz and J. R. Chelikowsky, *J. Chem. Phys.*, 2012, **136**, 204117.

[26] H. Monkhorst and J. Pack, *Phys. Rev. B*, 1976, **13**, 5188–5192.

[27] J. Moreno and J. Soler, *Phys. Rev. B*, 1992, **45**, 13891–13898.

[28] G. Kresse and J. Furthmüller, *Comput. Mater. Sci.*, 1996, **6**, 15–50.

[29] G. Kresse and J. Furthmüller, *Phys. Rev. B*, 1996, **54**, 11169–11186.

[30] G. Kresse and J. Hafner, *J. Phys.: Condens. Matter*, 1994, **6**, 8245–8257.

[31] S. Botti, D. Kammerlander and M. A. L. Marques, *Appl. Phys. Lett.*, 2011, **98**, 241915.

[32] A. J. Jackson, J. M. Skelton, C. H. Hendon, K. T. Butler and A. Walsh, *J. Chem. Phys.*, 2015, **143**, 184101.

Chapter 5

Ab initio thermodynamics

5.1 Chemical thermodynamics

> *Chemical thermodynamics and its connection to electronic structure is too broad and interconnected a field to cite every claim and equation; a selection of reference material for this section is cited as Refs. 1–6.*

In chemistry and chemical engineering, thermodynamics is generally used to predict the behaviour of systems including:

- the relative stability of compounds and phases (and hence the viability of transformations);
- heats of reaction (and hence the heating and cooling duty on transformations);
- activation energies of transformations (and hence their temperature dependence);
- the effects of pressure on transformations.

In this sense a "transformation" may be a phase change, chemical reaction, defect formation etc. A number of derived properties exist with units of energy, known as "thermodynamic potentials". Of these, two are of the most direct interest in chemistry: the change in enthalpy H corresponds to the energy transferred to a system as heat and work, and is vital for a controlled reaction; the Gibbs free energy G determines whether a reaction is actually favourable, as it takes into account the entropic driving force. In practice we also encounter the internal energy U and Helmholtz free energy A; these four potentials are expressed through many relationships, but one of the simplest forms is:

$$H = U + PV \tag{5.1}$$

$$A = U - TS \tag{5.2}$$

$$G = H - TS \tag{5.3}$$

where T and S are the thermodynamic (absolute) temperature and entropy, respectively. (Note that V is always used to denote volume in this work; the clash with its use as "potential" in many descriptions of mechanics is unfortunate.)

The internal energy U is a sum of all the potential and kinetic energy in a system within its own reference frame (e.g. potential due to attraction to the Sun is neglected). Given the existence of vibrations (which periodically exchange a portion of kinetic and potential energy) in virtually all systems, it is more productive to divide this into a baseline energy and a vibrational contribution from the movements of nuclei:

$$U = E_0 + E_{\text{vib}}. \tag{5.4}$$

If we disregard intra-nuclear and gravitational contributions (which fall beyond the remit of conventional chemistry), then E_0 may be taken as a combination of the electrostatic potential energy and the kinetic energy of the unperturbed system; at the ground state this may be calculated by electronic structure methods such as density functional theory (DFT). In turn, the vibrational contributions may be divided into a temperature-dependent term and a temperature-independent zero-point energy (ZPE). The zero-point energy term is related to Heisenberg's uncertainty principle — where a potential well exists in a quantum system, there must be some movement or both the position and momentum would be known exactly. This movement is associated with an energy, and hence there is an additional energy cost associated with forming the potential well. The temperature-dependent term may be given a nominal symbol such as $U'(T)$ but it is less ambiguous to consider it in terms of the constant-volume heat capacity

$$C_V = \left(\frac{\partial U}{\partial T}\right)_V \tag{5.5}$$

and hence

$$U(T) = E_0 + E_{\mathrm{ZPE}} + \int_0^T C_V \mathrm{d}T. \tag{5.6}$$

By also making use of the constant-pressure heat capacity

$$C_P = \left(\frac{\partial H}{\partial T}\right)_P, \tag{5.7}$$

and paying careful attention to reference states and intermediate steps, it is possible to obtain the other thermodynamic potentials through a similar approach. Notably, at zero temperature

$$U^0 = H^0 = A^0 = G^0 = E_0 + E_{\mathrm{ZPE}}. \tag{5.8}$$

It is convenient to work in terms of *specific* (quantity-independent) properties of individual species; for example, the enthalpy H of one mole of i may be denoted $\hat{H}_i$. In the case of the Gibbs free energy, this is particularly significant, and the analogous term is referred to as the *chemical potential* μ_i:

$$\mu_i = \left(\frac{\partial G}{\partial n_i}\right)_{T,P,n_{j\neq i}} \tag{5.9}$$

where G is the Gibbs free energy of the whole system and n is the number of units (typically moles) of i in the system. In principle this includes interactions between i and other materials in the system, although we frequently make the *ideal mixture* assumption and assume that μ_i is independent of the other mixture components.

In general we consider that

$$\mu_i = \hat{H} - T\hat{S}_i = \hat{U} + P\hat{V} - T\hat{S} \tag{5.10}$$

and hence

$$\mu_i = E_0 + E_{\mathrm{ZPE}} + \int_0^T \hat{C}_V \mathrm{d}T + P\hat{V} - T\hat{S}. \tag{5.11}$$

For a gas, constant-pressure conditions are preferable to constant-volume. We work in terms of enthalpy and use Eq. (5.7) to form the free energy expression

$$\mu_{i,\mathrm{gas}} = E_0 + E_{\mathrm{ZPE}} + \int_0^T \hat{C}_p \mathrm{d}T - T\hat{S}. \tag{5.12}$$

Species	T_c / K	P_c / bar	ω
H_2	33.19	13.13	-0.216
N_2	126.2	34.00	0.038
Ar	150.9	48.98	0.000
O_2	154.6	50.43	0.022
H_2S	373.5	89.63	0.094

Table 5.1 – Data for corresponding-states models of some relevant gases.[2]

5.1.1 Equations of state

The ideal gas law $P\hat{V} = RT$ is widely employed in thermodynamics, and the majority of "standard" equations assume its validity. Generally the ideal gas law is considered to be applicable at low pressures and high temperatures; this may be considered more formally by looking at corrected equations of the form

$$P\hat{V} = ZRT. \tag{5.13}$$

The principle of corresponding states links the correction factor Z or "compressibility" to the critical points of compounds, via the reduced temperature and pressure $T_r = \frac{T}{T_c}$ and $P_r = \frac{P}{P_c}$, where a subscript c denotes the critical point. It has been observed that different fluids behave similarly when at equivalent T_r and P_r; this is formalised by Pitzer as

$$Z = Z_0 + \omega Z_1 \tag{5.14}$$

where Z_1 and Z_2 are both functions of T_r and P_r and ω, the 'acentric factor', accounts for complex fluids; it is quite empirical and takes the form

$$\omega = -1 - \log(P_r^{\text{sat}})_{T_r=0.7} \tag{5.15}$$

where $(P_r^{\text{sat}})_{T_r=0.7}$ is the reduced saturation pressure at $T_r = 0.7$. Values for Z_1 and Z_2 have been fitted to correlations and are tabulated in standard textbooks, e.g. Ref. 2 p.99. Table 5.1 shows the key data for a number of relevant gases — note that the critical points are far-removed from typical reaction conditions (putting $Z_0 \sim 1$), while the acentric factors are small (with the exception of hydrogen). This modelling approach reflects the concerns of the chemical industry a few decades ago, and is useful for high-pressure treatment of common gases. However, data for phases such as S_8 is much harder to come by. If it is necessary to investigate properties near the saturation point where significant van der Waals interactions are expected, an improved equation of state might be estimated with *ab initio* calculations.

5.1.2 Thermodynamic ensembles

An important aspect of thermodynamic modelling is the selection of a thermodynamic ensemble. This may be seen as a set of conditions for 'tiling' the model region to represent an infinite system.

The main system of interest in this work is the annealing step in two-step CZTS film formation, in which deposited metal-containing species are heated with a sulfur-containing gas mixture. In this case temperature and pressure are regulated, and additional gas is allowed to enter in order to maintain a pressure. This may be approximated with the **NPT** (constant n, P, T) ensemble – although the gas quantity n is not strictly fixed, in a large vessel with excess sulfur and a small quantity of solid the fluctuations would be very minor, and comparable to a system with a fixed amount of gas and a marginally variable volume.

Some experimental programs have placed solid sulfur in a sealed vessel with the other materials. In this case the pressure is not fixed, but the sulfur quantity is fixed strictly, while the temperature is controlled. This system is better matched by the **canonical** (constant n, V, T) ensemble.

The **grand canonical** (constant μ, V, T) ensemble is widely used in Monte Carlo modelling of reactions at interfaces and surfaces, where the region of study is only a small element of the system; the ensemble effectively permits the exchange of particles between adjacent "cells" of the ensemble as long as the chemical potential μ of the exchanged particles is maintained. This is less applicable for models of specific reaction systems, but is useful for exploring ranges of stoichiometry. It is common to use phase diagrams in which μ is a free parameter for some species, giving a map of the general phase space without specific details of the corresponding temperatures and pressures; this approach has been dominant in the discussion of competing phases and defects in CZTS.[7–9]

5.2 Molecular thermodynamics

The thermochemistry of molecules has historically been described well by statistical mechanics. All the key thermodynamic properties of a system can be obtained from the partition function

$$Q = \sum_i \exp \frac{-\epsilon_i}{k_B T}, \tag{5.16}$$

where each i is a unique state and ϵ_i is the energy of that state. The most concise relationship is that carved on Boltzmann's gravestone,

$$S = k_B \ln W \tag{5.17}$$

where W is the total number of states under consideration. In studies of chemical equilibrium the key equation is

$$A = -k_B T \ln Q \tag{5.18}$$

and hence

$$\mu = -k_B T \left(\frac{\partial \ln Q}{\partial N} \right)_{V,T} \approx -k_B T \ln \frac{q}{N} \tag{5.19}$$

where q is the *molecular* partition function over the states of an individual species and N is the number of molecules of that species.

The total partition function can be treated as a product of partition functions over the contributing sets of (assumed) independent degrees of freedom:

$$q = q_{\text{trans}} q_{\text{rot}} q_{\text{vib}} q_{\text{electr}} \tag{5.20}$$

which corresponds to a sum over energy contributions;

$$E = E_{\text{trans}} + E_{\text{rot}} + E_{\text{vib}} + E_{\text{electr}}. \tag{5.21}$$

DERIVATION OF EQ. (5.19) For N independent molecules with identical partition functions $q_i = q_0$, the system partition function

$$Q = q_1 q_2 q_3 q_4 \cdots = q_0^N.$$

Where the molecules are actually indistinguishable, with partition function q, the system partition function is reduced by a factor of all the equivalent arrangements and hence

$$Q = \frac{q^N}{N!}.$$

Returning to the premise of Eq. (5.19)

$$\mu = -k_B T \left(\frac{\partial \ln Q}{\partial N} \right)_{V,T},$$

we substitute for Q and use Stirling's approximation $\ln x! \approx x \ln x - x$:

$$\begin{aligned}
\mu &= -k_B T \frac{\partial \left(\ln q^N - \ln N! \right)}{\partial N} \\
\mu &= -k_B T \frac{\partial \left(N \ln q - (N \ln N - N) \right)}{\partial N} \\
\mu &= -k_B T \left(\ln q - (\ln N + 1) + 1 \right) \\
\mu &= -k_B T \ln \frac{q}{N}
\end{aligned}$$

5.2.1 Translational contribution

q_{trans} depends on the mass m and the the molar volume $\hat{V}$, which is related to pressure by an equation of state such as the ideal gas law:

$$q_{\text{trans}} = \left(\frac{2\pi m k T}{h^2} \right)^{\frac{3}{2}} \hat{V} \tag{5.22}$$

$$q_{\text{trans}} = \left(\frac{2\pi m k T}{h^2} \right)^{\frac{3}{2}} \left(\frac{RT}{p} \right) \tag{5.23}$$

such that the molecular partition function at standard pressure

$$q(p^{\ominus}) = \left(\frac{2\pi m k T}{h^2} \right)^{\frac{3}{2}} \left(\frac{RT}{p^{\ominus}} \right) q_{\text{rot}} q_{\text{vib}} q_{\text{electr}}. \tag{5.24}$$

A convenient way of calculating the translational energy is to first calculate the thermal de Broglie wavelength, Λ:

$$\Lambda = \sqrt{\frac{2\pi\hbar^2}{m k_B T}} \tag{5.25}$$

$$q_{\text{trans}} = \frac{V}{\Lambda^3}. \tag{5.26}$$

Table 5.2 – Relationship between symmetry group and rotational symmetry number. Reproduced from Ref. 10.

Group	σ	Group	σ	Group	σ	Group	σ
C_1, C_i, C_S, $C_{\infty v}$	1	$D_{\infty h}$	2	T, T_d	12	O_h	24
C_n, C_nv, C_{nh}	n	D_n, D_{nh}, D_{nd}	$2n$	S_n	$\frac{n}{2}$	I_h	60

5.2.2 Rotational contribution

For a linear molecule in the high-temperature limit

$$q_{\text{rot}} = \frac{2Ik_BT}{\sigma\hbar^2}, \tag{5.27}$$

which is sometimes expressed as

$$q_{\text{rot}} = \frac{k_BT}{\sigma B}, \qquad B = \frac{\hbar^2}{2I} \tag{5.28}$$

where σ is a symmetry parameter (the number of equivalent rotational configurations) and I is the (scalar) moment of inertia. The symmetry parameter is related to the point groups of molecules as shown in Table 5.2. For more complex molecules in the high-temperature limit

$$q_{\text{rot}} = \frac{\sqrt{\pi I_a I_b I_c}}{\sigma}\left(\frac{2k_BT}{\hbar^2}\right)^{\frac{3}{2}} \tag{5.29}$$

where I_a, I_b, I_c are the three moments of inertia. In general,

$$\mathbf{I} = (I_a, I_b, I_c) = \sum m_i \mathbf{r}_i{}^2. \tag{5.30}$$

where m_i and $\mathbf{r}_i$ are the mass and Cartesian position of each atom i in the molecule.

(5.31)

5.2.3 Vibrational contribution

In a diatomic molecule, vibrational motion is modelled as a single simple harmonic oscillator, with vibrational frequency ν and energies

$$\epsilon_n = (n+\tfrac{1}{2})\hbar\omega = (n+\tfrac{1}{2})h\nu \tag{5.32}$$

where n is any positive integer. Therefore the partition function

$$q_{\text{vib}} = \exp\left(\frac{-h\nu}{2k_BT}\right)\sum_{n=0}^{\infty}\exp\left(\frac{-nh\nu}{k_BT}\right) = \frac{\exp\left(\frac{-h\nu}{2k_BT}\right)}{1-\exp\left(\frac{-h\nu}{k_BT}\right)}. \tag{5.33}$$

The problem of a poly-atomic molecule is simplified mathematically by reducing the vibrations to a set of normal modes. These are collective movements in which atoms move at the same frequency and the centre of mass remains fixed, forming a complete basis for any other atomic movements. Because of these properties, the above equation can be applied to each mode independently. These are then combined to form an overall partition function:

$$q_{\text{vib}} = \prod_i^{3N-6} q_i. \tag{5.34}$$

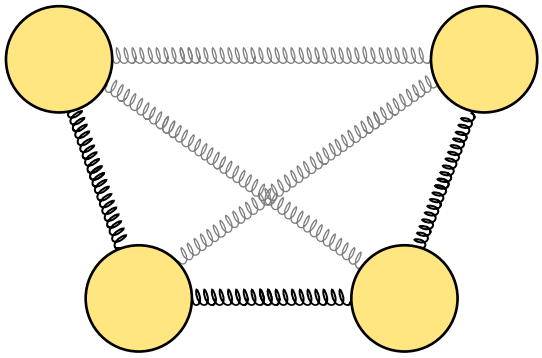

Figure 5.1 – Schematic of S_4 (C_{2v}) modelled as particles connected by springs. Major interactions ("bonds") are indicated with thick black springs, but structure and dynamics are also regulated by weaker long-range interactions (grey springs).

Calculating the frequencies

For small movements about the minimum of a potential energy surface, we take the "harmonic approximation". Suppose we model a molecule as a set of particles connected by springs (Fig. 5.1). The system is described by a set of $3N$ Cartesian coordinates $\mathbf{x}$.

In the Taylor expansion about energy E as a function of the atomic positions $\mathbf{x}$

$$E(\mathbf{x}) = E(\mathbf{x}_0) + [\mathbf{x} - \mathbf{x}_0] \cdot \nabla E + \frac{1}{2}([\mathbf{x} - \mathbf{x}_0]\nabla)^2 E + \ldots \tag{5.35}$$

the first term $E(\mathbf{x}_0)$ is reference energy of the unperturbed system. In the second term ∇E is the derivative of energy with respect to the atomic positions; at equilibrium this is always equal to zero as the equilibrium positions are a local minimum. The first term to describe the dynamics of the system is the second-order group $\frac{1}{2}([\mathbf{x} - \mathbf{x}_0]\nabla)^2 E$. In matrix form

$$([\mathbf{x} - \mathbf{x}_0]\nabla)^2 E = [\mathbf{x} - \mathbf{x}_0]^{\mathrm{T}} \mathbf{H} [\mathbf{x} - \mathbf{x}_0] \tag{5.36}$$

where $\mathbf{H}$ is the "Hessian" matrix

$$\mathbf{H} = \begin{pmatrix} \frac{\partial^2 E}{\partial x_1^2} & \frac{\partial^2 E}{\partial x_1 \partial x_2} & \cdots & \frac{\partial^2 E}{\partial x_1 \partial x_n} \\ \frac{\partial^2 E}{\partial x_2 \partial x_1} & \frac{\partial^2 E}{\partial x_2^2} & \cdots & \frac{\partial^2 E}{\partial x_2 \partial x_n} \\ \vdots & \vdots & \ddots & \vdots \\ \frac{\partial^2 E}{\partial x_n \partial x_1} & \frac{\partial^2 E}{\partial x_n \partial x_2} & \cdots & \frac{\partial^2 E}{\partial x_n^2} \end{pmatrix}. \tag{5.37}$$

Each term represents a harmonic interaction between two coordinates. Hooke's Law gives the relationship between the displacement of a particle from equilibrium and the resulting restoring force:

$$F_i = \frac{\partial E}{\partial x_i} = -k(x_i - x_{i0}) \tag{5.38}$$

and so each term $\frac{\partial^2 E}{\partial x_i \partial x_j}$ in the Hessian gives the change in force along x_i in response to a change in x_j,

$$\frac{\partial^2 E}{\partial x_i \partial x_j} = \frac{\partial}{\partial x_j} F_i = -k_{ij}. \tag{5.39}$$

In the harmonic approximation this is a full description of the system; anharmonic models may incorporate higher-level interaction terms and/or non-linearity. For many atomistic modelling methods, including DFT calculations with some popular XC functionals, instantaneous forces are directly available for each atom. The Hessian is then constructed using one finite displacement δ for each degree of freedom:

$$k_{ij} = F_j(x_i + \delta, x_j) \cdot \delta. \tag{5.40}$$

The size of the displacement must be small enough to avoid significant anharmonic contributions, and large enough to prevent error from "numerical noise".*

The Hessian and $\mathbf{x}$ do not need to use Cartesian coordinates — in fact, it is inefficient to do so. The $3N$ coordinates encode overall rotational and translational degrees of freedom, which have no meaningful effect on the system, as well as the significant harmonic movements. The Hessian can be diagonalised, changing basis to a set of non-interacting harmonic relationships. These are the "normal modes" and their non-interaction allows for the relatively simple statistical mechanical treatment in Section 5.2.3. The eigenvalues of the matrix provide the set of frequencies ω_i while the corresponding eigenvectors may be subjected to group theoretical analysis to identify modes with the appropriate symmetry properties for spectroscopic observations. For molecules, six of these eigenvalues theoretically have values of zero and can be discarded; in practice they will deviate slightly and are used to give an informal estimate of the calculation quality.†

5.3 Solid-state thermodynamics

Returning to Eq. (5.11):

$$\mu_i = E_0 + E_{\mathrm{ZPE}} + \int_0^T \hat{C}_V \mathrm{d}T + P\hat{V} - T\hat{S}.$$

For an incompressible solid, $\left(\frac{\partial \hat{V}}{\partial P}\right)_T = 0$ and $\left(\frac{\partial S}{\partial P}\right)_T = 0$. Equation (5.11) may be used as it is, once $\hat{V}$ and S are known as functions of temperature.

At the moderate pressures associated with thin-film annealing, the energy associated with the PV term is relatively small. For water, $\rho \approx 1000\,\mathrm{kg\,m^{-3}}$ and $\hat{m} \approx 18\,\mathrm{kg\,kmol^{-1}}$ so

$$E_{PV} = P\hat{V} = \frac{P\hat{m}}{\rho} \tag{5.41}$$

$$\frac{E_{PV}}{P} = \frac{18\,\mathrm{kg\,kmol^{-1}}}{1000\,\mathrm{kg\,m^{-3}}} = 0.018P\,\mathrm{J\,kmol^{-1}\,Pa^{-1}} = P \cdot 1.8 \times 10^{-8}\,\mathrm{kJ\,mol^{-1}\,Pa^{-1}}. \tag{5.42}$$

As a result, this term may be safely neglected. In this work it is included, but the corrections due to thermal expansion are neglected; this term is expected to be at least one order of magnitude smaller.

The values to be obtained therefore are the ground state energy E_0, the vibrational zero-point energy E_{ZPE}, the enthalpy correction $\int_0^T \hat{C}_V \mathrm{d}T$ and entropy $S(T)$. In this work these are assumed to be dominated by vibrational contributions. It is possible to examine the energy of a

*There are several common causes of computational errors associated with small changes in values. As well as the convergence settings of the calculation method, error arises from the limited precision of floating-point numbers and the limited accuracy of operations which are approximated iteratively such as square roots. All of these can be controlled, but this may involve significant code re-factoring and/or additional calculation time.

†In calculations on a diatomic molecule there are five zero eigenvalues. The remaining eigenvector should correspond to the stretching mode, which is the only degree of freedom associated with the potential well.

range of electronic and magnetic states, and the thermal occupation of these states can be incorporated as a set of corrections.[11] However, these corrections are typically small in magnitude and require accurate description of excited states; this demands computationally-expensive beyond-DFT methods, as local density functionals tend to drastically underestimate the energy of above-gap states. The contribution of these states is negligible for semiconductors, but may be of comparable magnitude to quasi-harmonic effects in metals.[12]

Crystals are not typically considered to have a significant energy contribution from translational or rotational motion. For a molecule, the contributions from vibrations, translations and rotations are of a similar order of magnitude. In a macroscopic sample such as a crystal, the number of vibrational microstates scales with the number of unit cells (for a 1 mol crystal, this is $N_A \approx 6 \times 10^{23}$) while the number of translational and rotational states remains the same as a single molecule.

The treatment of vibrational states in periodic crystals is similar in principle to that in molecules; however, instead of thermally occupying a series of fixed frequencies, it is necessary to consider the long-range ordering of vibrations over multiple unit cells. The formalism is laid out clearly by Dove[13]:

$$E = \sum_{\mathbf{q},\nu} \hbar\omega \left[\frac{1}{2} + \left(\exp\left(\hbar\omega(\mathbf{q},\nu)/k_B T \right) - 1 \right)^{-1} \right] \tag{5.43}$$

where ν is the index of a vibrational normal mode, and $\mathbf{q}$ is a reciprocal space vector.* The vibrational frequencies are plotted against $\mathbf{q}$ to form a *phonon band structure* or "phonon dispersion" plot.† (Chapter 7 uses these plots extensively; see Fig. 7.5 on page 105 for an example.) "Phonons" are the quantised energy packages which thermally occupy this structure of possible lattice vibrations. The modes may be assigned letter labels, which are derived from the group theoretical description of the mode symmetries. The x-axis typically follows a reciprocal-space path between high-symmetry "special points". The naming convention for these points, following the Cracknell–Davies–Miller–Love convention, uses Greek letters to indicate points within the Brillouin Zone and Latin letters to indicate points at the zone boundary. In practice, a density of states (DOS) is formed which integrates over the Brillouin zone, and thermodynamic properties are obtained by integrating over the DOS rather than summing over all frequencies and $\mathbf{q}$-points. The actual displacements resemble electronic Bloch waves

$$u_{jl}(\mathbf{q},\omega) = u_{j0}(\mathbf{q}) \cdot \exp\left[i(\mathbf{q}\cdot\mathbf{R}_l - \omega t) \right], \tag{5.44}$$

where j indicates an ion in the first unit cell and l is the index of a given unit cell, but unlike the wavefunctions of Bloch's theorem the periodic function u_{j0} is a function of the wave vector.

Two practical methods for calculating the Hessian matrix for solid-state systems are calculations using density-functional perturbation theory (DFPT) and the "frozen-phonon" method, which is also referred to as the "direct" and "supercell" method.[17] In DFPT, a modified version of Kohn–Sham DFT is used to obtain the linear response of a system's electron density to perturbations in its nuclear positions; this is directly related to the force constants between the corresponding atoms. In this work the frozen-phonon approach is employed as implemented in "Phonopy", an open-source code developed by Atsushi Togo.[15] Small finite displacements are used as described above for molecular systems; in order to avoid spurious interactions across the periodic boundary, a supercell is used to increase the distance between periodic images.

*Dove[13] and Ashcroft and Mermin[14] use $\mathbf{k}$ to indicate the reciprocal space vector in lattice vibrations; in this work we follow the preferred notation of Togo and Tanaka[15] and of Yu and Cardona[16] such that $\mathbf{k}$ is reserved for reciprocal space vectors in the electronic structure. This avoids confusion where both a $\mathbf{k}$-point mesh and $\mathbf{q}$-point mesh must be specified.

†The "phonon dispersion" name is related to the behaviour of the acoustic modes, which exhibit a strong frequency dependence on $\mathbf{q}$ and have zero frequency at the origin of reciprocal space, Γ.

Phonopy enables the cost of such calculations to be reduced in high-symmetry systems by analysing the space group with the "Spglib" library, and setting up the minimum number of necessary finite displacements for electronic structure calculations.[18]

Bibliography

[1] S. Stølen and T. Grande, *Chemical Thermodynamics of Materials*, Wiley, Chichester, 2004.

[2] J. Smith, H. Van Ness and M. Abbott, *Introduction to Chemical Engineering Thermodynamics*, McGraw-Hill, New York, 7th edn., 2005.

[3] P. Atkins and J. de Paula, *Atkins' Physical Chemistry*, Oxford University Press, Oxford, 8th edn., 2006.

[4] G. Price, *Thermodynamics of Chemical Processes*, Oxford University Press, Oxford, 1998.

[5] R. P. Stoffel, C. Wessel, M.-W. Lumey and R. Dronskowski, *Angew. Chem., Int. Ed. Engl.*, 2010, **49**, 5242–66.

[6] K. Reuter, C. Stampfl and M. Scheffler, in *Handbook of Materials Modeling, Part A. Methods*, ed. S. Yip, Springer, Berlin, 2005, pp. 149–234.

[7] S. Chen, X. G. Gong, A. Walsh and S.-H. Wei, *Appl. Phys. Lett.*, 2010, **96**, 021902.

[8] S. Chen, J.-H. Yang, X. G. Gong, A. Walsh and S.-H. Wei, *Phys. Rev. B*, 2010, **81**, 245204.

[9] V. Kosyak, N. B. Mortazavi Amiri, A. V. Postnikov and M. A. Scarpulla, *J. Appl. Phys.*, 2013, **114**, 124501.

[10] K. K. Irikura, in *Computational Thermochemistry*, ed. K. K. Irikura and D. J. Frurip, American Chemical Society, Washington DC, 1998, ch. Appendix B, pp. 402–418.

[11] A. Dick, F. Körmann, T. Hickel and J. Neugebauer, *Phys. Rev. B*, 2011, **84**, 125101.

[12] B. Grabowski, L. Ismer, T. Hickel and J. Neugebauer, *Phys. Rev. B*, 2009, **79**, 134106.

[13] M. T. Dove, *Introduction to Lattice Dynamics*, Cambridge University Press, Cambridge, 1993.

[14] N. W. Ashcroft and N. D. Mermin, *Solid-State Physics*, Thomson Learning, 1976.

[15] A. Togo and I. Tanaka, *Scr. Mater.*, 2015, **108**, 1–5.

[16] P. Y. Yu and M. Cardona, *Fundamentals of Semiconductors*, Springer-Verlag Berlin Heidelberg, New York, 3rd edn., 2003.

[17] S. Baroni, S. De Gironcoli, A. Dal Corso and P. Giannozzi, *Rev. Mod. Phys.*, 2001, **73**, 515–562.

[18] A. Togo, *Spglib*, `http://spglib.sourceforge.net/index.html`, [Accessed: 2015-08-25].

Part III

Results and analysis

Chapter 6

Thermochemical modelling of sulfur vapours

The thermochemistry of sulfur vapours is an intriguing problem; sulfur adopts a wide range of possible allotropes. An equilibrium model was developed in the 1970s to consider the effect of intermediate allotropes, and quantum chemistry was applied to study the diversity of allotropes in the late 1980s and early 1990s. The work presented here appears to be unique in combining the two approaches to build a complete picture.

Thermodynamic studies of metal chalcogenides have tended to select a sulfur phase (always α-S, S_2 or S_8) and use this as the reference energy. However, it is quite possible for annealing conditions to span over several appropriate models. The model of sulfur equilibria developed here presents a single relationship for the chemical potential $\mu_S = f(T,P)$, which can be inserted into any relevant phase equilibrium problem. This potential form is employed in the equilibrium models in Chapter 8.

This work was submitted as a full paper in August 2015 and published in the Feb 2016 issue of *Chemical Science*. All vibrational calculations, mathematical modelling and supporting programs were developed by AJJ, as was the majority of the manuscript preparation. The following text in this chapter is reproduced from the published manuscript with minor corrections and changes (e.g. the addition of page references). The reader may prefer the original two-column format; the article is available online with Open Access at `http://dx.doi.org/10.1039/C5SC03088A`.

A universal chemical potential for sulfur vapours†

Adam J. Jackson[a], Davide Tiana[a,‡] and Aron Walsh*[a,b]

The unusual chemistry of sulfur is illustrated by the tendency for catenation. Sulfur forms a range of open and closed S_n species in the gas phase, which has led to speculation on the composition of sulfur vapours as a function of temperature and pressure for over a century. Unlike elemental gases such as O_2 and N_2, there is no widely accepted thermodynamic potential for sulfur. Here we combine a first-principles global structure search for the low energy clusters from S_2 to S_8 with a thermodynamic model for the mixed-allotrope system, including the Gibbs free energy for all gas-phase sulfur on an atomic basis. A strongly pressure-dependent transition from a mixture dominant in S_2 to S_8 is identified. A universal chemical potential function, $\mu_S(T,P)$, is proposed with wide utility in modelling sulfurisation processes including the formation and annealing of metal chalcogenide semiconductors.

6.1 Introduction

Sulfur is an abundant resource exploited by industry on a scale of tens of millions of tonnes per year.[1] While it may be found in its elemental form, the primary industrial source is hydrogen sulfide, a byproduct of the oil and gas industry. The vast majority of industrial sulfur is converted to sulfuric acid or sulfur dioxide before further use; this may explain the surprising shortage of data in the thermochemical literature regarding the vapour phase of elemental sulfur.

Historically, the thermochemistry of sulfur has been studied experimentally and has been understood to be associated with a variable composition for over a century; Lewis and Randall remarked in 1914 that "no other element is known to occur in as many different forms as sulfur" while studying the free energy of a number of these forms.[2] (Carbon now has a higher number of known allotropes but the majority of these are not naturally-occurring.) However, contemporary reference data for sulfur still does not present a complete picture; the NIST-JANAF Thermochemical Tables (1998) give thermochemical data for two solid phases, one liquid phase, the ions S^+ and S^- and eight gas allotropes $S_{1\text{-}8}$.[3] Of these, only S_2 and S_8 are from spectroscopic data. The allotropes $S_{3\text{-}7}$ are assumed to exist and are assigned energies following an interpolation scheme suggested by Rau *et al.* (1966), which also makes use of experimental data for S_6.[4] That paper rules out the significant presence of tautomers, finding little evidence of a tautomer contribution and assuming that they have relatively high energy. The authors generally reserve speculation on the actual structures of the components of their equilibrium model.

In recent years considerable attention has turned to metal chalcogenides; II-VI semiconductors such as ZnS, CdS, PbS are widely studied in many contexts.[5] Copper indium gallium selenides (CIGS) and cadmium telluride (CdTe) are used as the basis for "second-generation" thin-film photovoltaic devices, and have seen a dramatic rise in production. $Cu_2ZnSn(S,Se)_4$ (CZTS)

[a] *Centre for Sustainable Chemical Technologies and Dept. of Chemistry, University of Bath, Claverton Down, Bath BA2 7AY, UK*

[b] *Global E^3 Institute and Department of Materials Science and Engineering, Yonsei University, Seoul 120-749, Korea*

‡ Current: *EPFL Valais Wallis, EPFL LSMO, Rue de l'Industrie 17, Case postale 440, CH-1951 Sion, Switzerland*

† Electronic Supplementary Information (ESI) available: Tabulated free energy and enthalpy data. See DOI: 10.1039/C5SC03088A. Additional data and code available in external repositories with DOIs: 10.5281/zenodo.28536; 10.6084/m9.figshare.151373; 10.6084/m9.figshare.1513833. See Data Access Statement for more information.

and Cu_2SnS_3 (CTS) devices have so far struggled to match these materials in terms of energy conversion efficiencies, but hold significant long-term promise due to their use of highly abundant elements; such availability is a prerequisite for terawatt-scale photovoltaics.[6] As such, thin-film processing in sulfur atmospheres is of considerable interest, as the inherent safety of industrial processing may be improved by eliminating the use of toxic H_2S. In addition to chalcogen annealing, which is used to increase grain size, substitute other elements or directly form chalcogenides from elements, high-quality single-crystal samples may be produced using chemical vapour transport of elemental chalcogens.[7–9] Previous work on the thermodynamics of such processing has tended to assume that sulfur adopts one particular gaseous allotrope (either S_2 or S_8), but the validity of this assumption has not been explored in depth.[10–12] It is undermined however by the model derived by Rau *et al.*, which predicts that no one component makes more than 50% of the gas mixture at temperatures between 800–1000 K.[4]

Mass spectrometry at a relatively mild 105°C has observed a series of charged clusters with the form $(S_{8n})^+$.[13] In the mid 1980s, a number of cyclic allotropes had been identified by crystallisation and X-ray diffraction, but this only covered the range $n = 6$–20.[14] An *ab initio* study was carried out for S_2 through to S_{13} in an early application of the Car-Parrinello simulated annealing method.[15] Energies were calculated using density-functional theory with the local density approximation (LDA). While limited by the inherent difficulties in exploring the entire potential energy surface of the atomic positions, this thorough study generated 21 allotropes, finding a local maximum in the atomisation energy at $n = 8$. A later (1990) paper used coupled-cluster electronic structure calculations to study the proposed tautomers of S_4 in depth, concluding that the planar structure with C_{2v} symmetry is lowest in energy, with a trans (C_{2h}) structure also visible in experimental spectra; a more recent *ab initio* study reached similar conclusions regarding stability while challenging the spectroscopic assignment of the phases.[16;17] The C_{2v} structure was ruled out in the simulated annealing study with LDA, although the authors noted the experimental evidence for its existence.[15] A 2003 review by Steudel *et al.*[18] collects more recent data, including both experimental and theoretical studies of vapour-phase allotropes; this review notes the weakness of the widespread assumption that each size is represented by a single species.[18] The work compares several sets of enthalpies relative to S_8 that have been obtained experimentally; variability is high for the smaller allotropes while there is fairly good agreement for the larger allotropes. Studies are generally carried out at a single temperature, such that the temperature and pressure dependence of the thermochemistry must be derived from statistical mechanics and analysis of vibrational information.

In this study, we develop a set of structures for S_2–S_8, compute their Gibbs free energy from first-principles and with empirical corrections, and solve the temperature-dependent chemical potential to describe the gaseous mixture. The potential function will be important for quantitative investigations of defect formation and phase stability in metal sulfide materials.

6.2 Methods

6.2.1 Density functional theory

Energies and forces of arbitrary clusters of sulfur atoms were computed within Kohn-Sham density-functional theory (DFT).[19] A range of exchange-correlation functionals were used in this work: PBE is a popular and elegant implementation of the Generalised Gradient Approximation (GGA) and PBEsol restores a periodic exchange contribution leading to improved performance for solids;[20;21] B3LYP* is a widely-used "hybrid" functional which combines pre-

*Note that the implementation of B3LYP in FHI-AIMS uses a parameterisation of the local density contribution based on the Random Phase Approximation in order to match values obtained with GAUSSIAN, another quantum chemistry code.[22]

existing gradient corrections with "exact" Hartree-Fock exchange;[23] PBE0 applies similar principles to the parameter-free PBE functional.[24] (While PBE is generally preferred to PBEsol for molecular calculations, PBEsol was included in this study for its compatibility with other all-electron work using this functional.)

Calculations for the evolutionary algorithm search used the Vienna Ab Initio Simulations Package (VASP) with the PBE exchange-correlation functional and a plane-wave basis set with a 500 eV energy cutoff.[25;26] As calculations in VASP employ a periodic boundary condition, orthorhombic bounding boxes were employed with 10 Å of vacuum between each molecule and its periodic images. Electronic structure iteration used only the Γ-point of this large cell.

Further calculations used the Fritz Haber Institute ab initio molecular simulations package (FHI-AIMS) to carry out all-electron DFT calculations with numerically-tabulated basis sets.[27;28] All calculations were open-shell with S_2 adopting its low-energy triplet spin configuration. The recommended "tight" basis set was employed for initial relaxation and study with PBEsol, which extends the minimal set of occupied orbitals with 6 additional functions. This was extended further to the full "tier 2" set of 9 additional functions for calculations with the LDA, PBE0, and B3LYP functionals.

6.2.2 Global structure search

Global structure optimisation was carried out with the USPEX package, which was originally developed for crystalline systems and has been adapted for use with clusters.[29–31] At this stage, molecules larger than S_8 were disregarded, as experimental results anticipate high- and low-temperature limits dominated by S_2 and S_8, respectively. Clusters were generated for $S_{3\text{-}7}$, and refined with an evolutionary algorithm to minimise the ground-state energy until a number of seemingly distinct clusters were identified by inspection. The atomic positions of these clusters were then optimised in FHI-AIMS calculations with PBEsol, using the BFGS algorithm to minimise the atomic forces to less than 10^{-4} eV Å^{-1} and converge energy to within 10^{-6} eV. Point groups were assigned to the structures using Materials Studio version 6.0, a proprietary package developed by Accelrys.

6.2.3 Vibrational frequencies

Vibrational frequencies were calculated within the harmonic approximation by making finite displacements to each atomic position to obtain the local potential wells, and diagonalising the resulting dynamical matrix to obtain the normal modes and their frequencies. This is implemented as a script and diagonalisation routine provided with FHI-AIMS.

Improved vibrational frequencies may be obtained by applying an empirically-derived scale factor to the vibrational eigenvalues computed using DFT; collections of such scale factors have been published for large test-sets of molecules.[32;33] The use of these factors is somewhat problematic when creating a systematic, transferable set of data but offers an opportunity to create the most realistic thermochemical model possible. Given that the calculations in this work involve a more limited subset of atomic interactions, we choose to fit a scaling factor to the experimentally-reported frequencies of S_8 and S_2.

6.2.4 Thermochemistry

Thermochemistry of individual gas species

Thermochemical properties were calculated within the ideal gas, rigid-rotor and harmonic vibration approximations. A set of textbook equations forms the chemical potential μ for

a nonlinear molecule from the ground-state electronic energy E_0 given a set of vibrational energies $\boldsymbol{\epsilon}$, the rotational constant σ, moment of inertia I

$$\mu = E_0 + E_{\text{ZPE}} + \int_0^T C_v + k_B T - TS \tag{6.1}$$

where

$$C_v = C_{v,\text{trans}} + C_{v,\text{vib}} + C_{v,\text{rot}} \tag{6.2}$$

$$\int_0^T C_v \approx \frac{3}{2}k_B + \sum_i \frac{\epsilon_i}{\exp(\epsilon_i/k_B T) - 1} + \frac{3}{2}k_B \tag{6.3}$$

$$\begin{aligned} S &= S_{\text{vib}} + S_{\text{trans}} + S_{\text{rot}} \\ &= \sum_i \left[\frac{\epsilon_i/k_B T}{\exp(\epsilon_i/k_B T) - 1} - \ln\left(1 - \exp(-\epsilon_i/k_B T)\right) \right] \\ &\quad + k_B \left[\ln\left(\frac{2\pi m k_B T}{h^2} \right)^{\frac{3}{2}} \frac{k_B T}{P_{\text{ref}}} p + \frac{5}{2} \right] \\ &\quad + k_B \left[\ln \frac{\sqrt{\pi \prod_i I_i}}{\sigma} \left(\frac{8\pi^2 k_B T}{h^2} \right)^{\frac{3}{2}} + \frac{3}{2} \right]. \end{aligned} \tag{6.4, 6.5}$$

These were applied as implemented in the Atomic Simulation Environment (ASE) Python package.[34] (Note that the expressions for monatomic and linear molecules are slightly different.) The rotational constants σ were assigned from the point groups.

Reference energies

A number of *ab initio* methods have been applied. In order to compare the energies, a reference point is needed. Conventionally the enthalpy of the ground state is zero; however, in this case the ground state phase α-sulfur is relatively expensive to compute. We therefore use the experimental sublimation enthalpy $\Delta H_{\text{sub}} = \frac{1}{8}H_{S_8} - H_{S_\alpha}$ to obtain a reference from the calculated enthalpy of S_8:

$$\Delta H_{S_x} = H_{S_x} - xH_{S_\alpha} \tag{6.6}$$

$$\Delta H_{S_x} = H_{S_x} - x\left(\frac{H_{S_8}}{8} + H_{S_\alpha} - \frac{H_{S_8}}{8} \right) \tag{6.7}$$

$$\Delta H_{S_x} = H_{S_x} - x\left(\frac{H_{S_8}}{8} - \Delta H_{\text{sub}} \right) \tag{6.8}$$

The preferred experimental value for ΔH_{sub} is $100.416/8 = 12.552$ kJ mol^{-1}, from experiments at 298K.[3] Note that the physical system does not in fact sublime at high temperatures, but passes through a molten phase. Nonetheless, it is more practical (and perfectly valid) to retain α-S as the reference state over the whole temperature range studied.

Equilibrium modelling

The following derivation closely follows the approach and notation of Ref. 35, which describes a generalised "non-stoichiometric method" for solving chemical equilibria. This approach is well-established and based on key work in Refs. 36–38.

We attempt to minimise the Gibbs free energy

$$\min G(\mathbf{n}) = \sum_{i=1}^{N} n_i \mu_i \tag{6.9}$$

subject to the mass balance constraint

$$\sum_{i=1}^{N} a_i n_i = b \tag{6.10}$$

where N is the number of unique species i with stoichiometric coefficient a_i, n is the quantity of species i and b is the total number of sulfur atoms. The classic approach for a constrained optimisation is the method of Lagrange multipliers. The Lagrangian is formed

$$\mathscr{L}(\mathbf{n}, \lambda) = \sum_{i=1}^{N} n_i \mu_i + \lambda \left(b - \sum_{i=1}^{N} a_i n_i \right) \tag{6.11}$$

and differentiated to form a set of equations defining the equilibrium state.

$$\left(\frac{\partial \mathscr{L}}{\partial n_i} \right)_{n_{j \neq i}, \lambda} = \mu_i - a_i \lambda \qquad = 0 \tag{6.12}$$

and

$$\left(\frac{\partial \mathscr{L}}{\partial \lambda} \right)_{\mathbf{n}} = b - \sum_{i=1}^{N} a_i n_i \qquad = 0. \tag{6.13}$$

The species chemical potential μ_i calculated as in Section 6.2.4 is a function of both temperature and the partial pressure $p_i = P \frac{n_i}{n_t}$ where P is the total pressure and the total quantity $n_t = \sum_i^N n_i$. The temperature dependence is complex and we are willing to solve the equilibrium at each temperature of interest, so we form a temperature-dependent standard free energy at a reference pressure $P^{\ominus}$, $\mu_i^{\ominus}(T) = \mu_i(T, P^{\ominus})$.

$$\mu_i(T, P, \mathbf{n}) = \mu_i^{\ominus}(T) + RT \ln \left(\frac{p_i}{P^{\ominus}} \right) \tag{6.14}$$

$$= \mu_i^{\ominus}(T) + RT \ln \left(\frac{n_i}{n_t} \frac{P}{P^{\ominus}} \right) \tag{6.15}$$

$$= \mu_i^{\ominus}(T) + RT \ln \left(\frac{P}{P^{\ominus}} \right) + RT \ln \left(\frac{n_i}{n_t} \right) \tag{6.16}$$

From here we drop the parenthetical indication that $\mu_i^{\ominus}$ is a function of temperature, and define the unit of pressure as the reference pressure, such that $P^{\ominus} = 1$. Substituting (6.16) into (6.12), we obtain

$$\mu_i^{\ominus} + RT \ln \left(\frac{n_i}{n_t} P \right) - a_i \lambda = 0 \tag{6.17}$$

$$\ln \left(\frac{n_i}{n_t} P \right) = \frac{a_i \lambda - \mu_i^{\ominus}}{RT} \tag{6.18}$$

and summing over i

$$P = \sum_{i=1}^{N} \exp \left(\frac{a_i \lambda - \mu_i^{\ominus}}{RT} \right). \tag{6.19}$$

The only unknown variable in this expression is λ; rearranging slightly we form a polynomial which is suitable for solving by standard numerical methods. The method employed in this work is the Levenberg-Marquardt least-squares algorithm, as implemented in Scipy.[39;40]

$$\sum_{i=1}^{N} \exp\left(\frac{-\mu_i^{\ominus}}{RT}\right)\left[\exp\left(\frac{\lambda}{RT}\right)\right]^{a_i} - P = 0 \tag{6.20}$$

To recover the composition **n**, we rearrange (6.18):

$$n_i = \frac{n_t}{P}\exp\left(\frac{a_i\lambda}{RT}\right)\exp\left(\frac{-\mu_i^{\ominus}}{RT}\right) \tag{6.21}$$

and substitute into the second equilibrium condition (6.10) to obtain

$$b = \frac{n_t}{P}\sum_{i=1}^{N} a_i \exp\left(\frac{a_i\lambda - \mu_i^{\ominus}}{RT}\right) \tag{6.22}$$

combining (6.21) and (6.22) we eliminate n_t

$$\frac{n_i}{b} = \frac{\exp\left(\frac{a_i\lambda-\mu_i^{\ominus}}{RT}\right)}{\sum_{j=1}^{N} a_j \exp\left(\frac{a_j\lambda-\mu_j^{\ominus}}{RT}\right)} \tag{6.23}$$

and clean up the notation by denoting $\exp\left(\frac{a_i\lambda-\mu_i^{\ominus}}{RT}\right)$ as Ξ_i

$$\frac{n_i}{b} = \frac{\Xi_i}{\sum_{j=1}^{N} a_j\Xi_j}. \tag{6.24}$$

Finally we obtain the normalised chemical potential of sulfur vapour on an atom basis. This turns out to be equal to the Lagrangian multiplier: the molar Gibbs free energy of sulfur atoms in a molecular gas mixture is defined as

$$\hat{G}_S(T,P) = \frac{\sum_{i=1}^{N} n_i\mu_i}{b} = \sum_{i=1}^{N}\frac{n_i}{b}\mu_i \tag{6.25}$$

and (6.24) is substituted in

$$\hat{G}_S(T,P) = \sum_{i=1}^{N}\left[\frac{\mu_i\Xi_i}{\sum_{j=1}^{N} a_j\Xi_j}\right]. \tag{6.26}$$

From (6.12), $\mu_i = a_i\lambda$ and hence

$$\hat{G}_S(T,P) = \frac{\sum_{i=1}^{N} a_i\lambda\Xi_i}{\left(\sum_{j=1}^{N} a_j\Xi_j\right)} = \lambda. \tag{6.27}$$

6.3 Results

6.3.1 Sulfur allotropes

A variety of candidate structures were generated in the evolutionary algorithm study with the PBE functional. The low-energy candidates following geometry optimisation are discussed in this section.

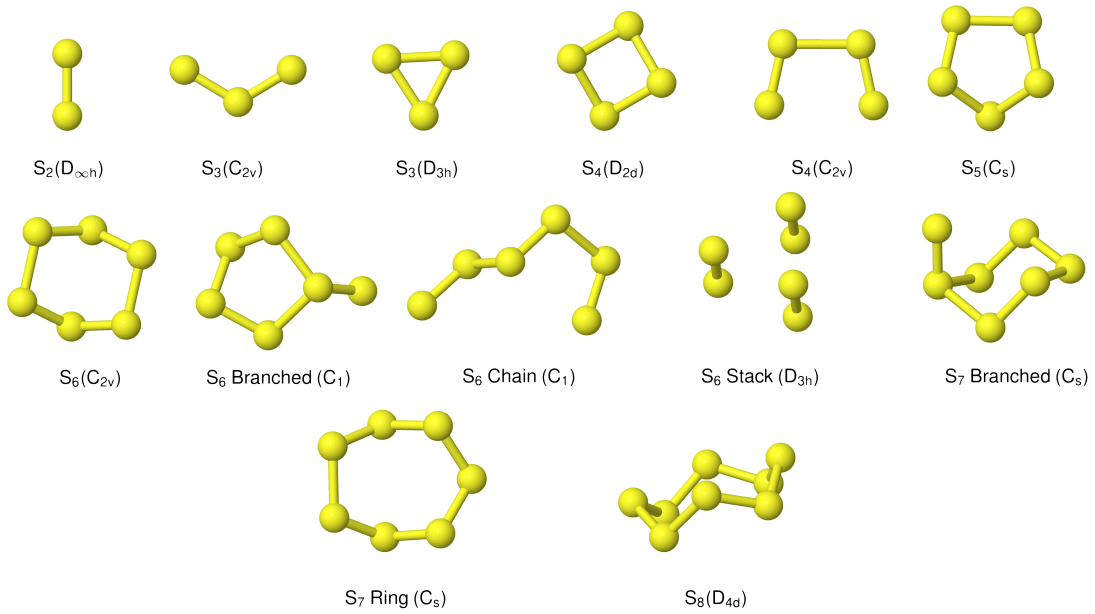

Figure 6.1 – Predicted low-energy sulfur clusters with symmetry assignment

S_2 Diatomic sulfur has the point group $D_{\infty h}$, in common with other homonuclear diatomics. The atoms were initially set 2 Å apart, and relaxed to a bond length of 1.91 Å. Studies with other functionals were relaxed either from this distance or from 2 Å. The resulting bond lengths are given in Table 6.1.

Table 6.1 – Calculated and experimental bond length r in S_2. Experimental value is NIST/JANAF-recommended distance.[3]

DFT functional	r / Å
PBE	1.911
PBEsol	1.903
LDA	1.895
PBE0	1.884
Experiment	1.889

S_3 The evolutionary algorithm process eliminated all but a C_{2v} non-linear chain for S_3. This corresponds to "thiozone", which has a well-characterised structure by rotational spectroscopy (bond length 1.917(1) Å and angle 117.36(6)°; the values from optimisation with PBE0 in this study are 1.901 Å and 118.2°).[41] We have also considered the simple triangular allotrope, which is ∼ 0.5 eV higher in ground-state energy.

S_4 A range of branched and cyclic structures were generated in the evolutionary algorithm. The structures included in the equilibrium modelling are shown in Fig. 6.1. The lowest-energy structure identified was the 'eclipsed' C_{2v} chain; this is in agreement with the high-level theoretical studies in Refs. 16;17. These studies identified a 'trans' C_{2h} structure as being likely to exist; there is some spectroscopic evidence for the viability of this isomer as well as a branched chain, but we were not able to reproduce stable structures corresponding to these allotropes through geometry optimisation.[42;43] Various cyclic and tetrahedral candidate structures yielded a relatively flat puckered ring with D_{2d} symmetry.

S_5 Although a wide range of branched and chain structures were generated, the main candidate is the 5-membered ring with C_s symmetry.

S_6 In addition to a cyclic C_{2v} allotrope, relatively low-energy branched and chain variations were identified. Of considerable interest is also a structure which may be viewed as a stack of two S_3 cycles, or alternatively as a cluster of S_2 diatoms. This appears to be the D_{3h} "prism" structure identified by Wong *et al.*;[44] the characteristic S-S bond lengths from that study were 190.1 and 276.2 pm, while the corresponding average distances from optimisation with the same hybrid XC functional (B3LYP) in this work were 189.0 and 275.7 pm. It is worth stressing that no explicit dispersion terms were included in any of the electronic structure calculations.

S_7 The evolutionary algorithm results rapidly provided the same C_s cyclic structure as that obtained by energy minimisation from a regular polygon. A branched structure, generated early in the progress of the algorithm, was also selected as an interesting alternative to include. This was about 1 eV lower in energy than the other candidates at that stage. Geometry optimisation by force relaxation yielded a compact structure, also with C_s (mirror-plane) symmetry.

S_8 No evolutionary algorithm study was applied for S_8, as its ring structure is quite well-known. The initial geometry was extracted from the crystal structure for the condensed α-S phase used in a previous study,[45] and relaxed to form an isolated D_{4d} ring.

Ground-state energies

An inspection of the ground-state energies from DFT reveals a trend of smoothly decreasing energy per atom with cluster size for the minimum-energy configuration at each size (Fig. 6.2 on the following page). The variation within the clusters included at each size is of the order 10 kJ mol^{-1} atom^{-1}, which is comparable to the energy difference between neighbouring cluster sizes.

6.3.2 Vibrational properties

Vibrational frequencies were calculated for all of the allotropes listed in section 6.3.1; frequencies for S_2 and S_8 are listed in Table 6.2 on page 89.

Empirical corrections

Empirical scale factors were determined by fitting the frequencies to the experimental spectrum for S_8. Note that frequencies are linearly proportional to their corresponding zero-point energies $E_{\mathrm{ZPE}} = \frac{1}{2}h\nu$ and hence this may also be seen as fitting to zero-point energy on a per-mode basis. The factors were calculated for each functional (Table 6.3 on page 89); scaling the frequencies from PBE0 by 96% was found to give the best overall fit, and is employed here as the reference "empirically-corrected" method. The resulting set of frequencies is illustrated in Fig. 6.3 on the next page alongside the uncorrected and experimental values. Using this scale factor also gives good agreement ($<4\,\mathrm{cm}^{-1}$ error) with the stretching frequency of S_2, which was not used in the fit. (Table 6.2 on page 89) Least-squares fitting was carried out with the Levenberg-Marquardt algorithm as implemented in Scipy.[39;40]

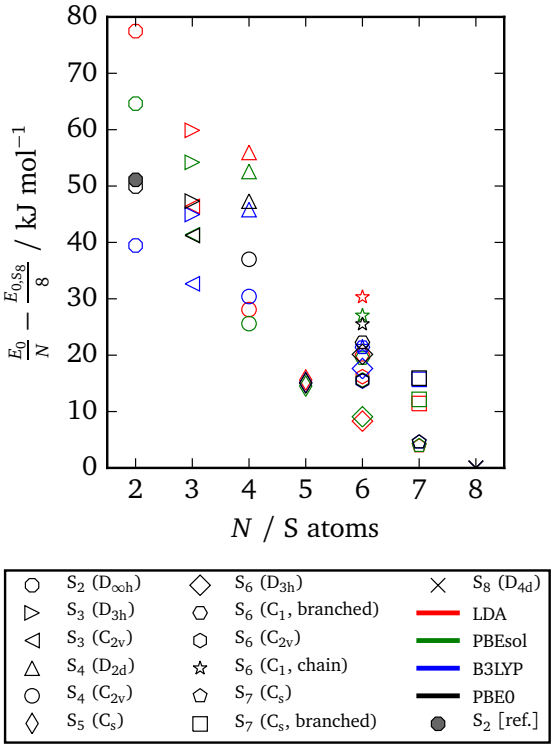

Figure 6.2 – Ground-state energies from DFT of clusters included in study. Energies are relative to the energy for S_8 with each functional, and normalised to the number of atoms. A point is also included from reference data;[3] this is derived from the enthalpies of formation at zero temperature, based on spectroscopic observations and equilibrium studies. While the energies from different exchange-correlation functionals diverge across the series, the S_2 energy from PBE0 calculations agrees closely with this reference data.

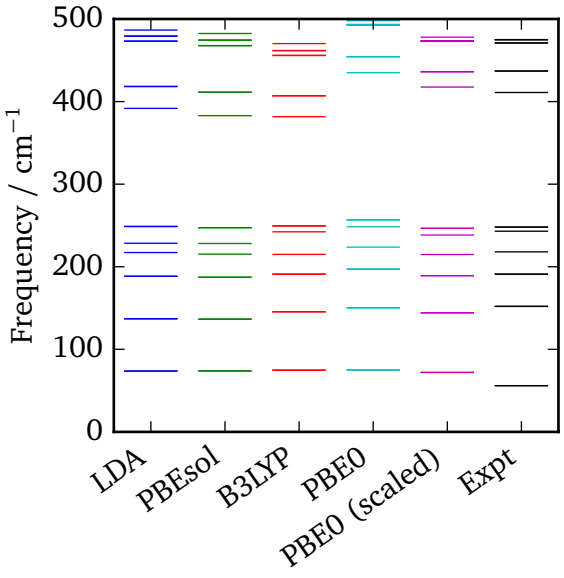

Figure 6.3 – Vibrational frequencies of S_8 calculated with various DFT functionals, compared with recommended experimental values.[3]

Table 6.2 – Calculated and experimental vibrational frequencies for S_2 and S_8.[3] All frequencies in cm^{-1}.

	LDA	PBEsol	PBE0	PBE0 (scaled)	B3LYP	Expt
S_2	716	713	751	721	714	724
S_8	73	73	74	71	74	56
	73	73	75	72	74	56
	136	136	150	144	145	152
	136	136	150	144	145	152
	188	187	197	189	191	191
	188	187	197	189	191	191
	217	215	223	214	214	218
	228	228	248	238	242	243
	248	247	256	246	249	248
	248	247	256	246	249	248
	391	382	434	417	381	411
	418	411	454	436	407	437
	418	411	454	436	407	437
	473	467	492	472	455	471
	473	467	492	472	455	471
	479	474	493	473	461	475
	479	474	493	473	461	475
	486	482	497	477	470	475

Table 6.3 – Optimal scale factors for exchange-correlation functionals, fitting to ground-state frequencies of S_8.[3] Standard deviations s for the least-squares fit are given over the set of frequencies in units of frequency and their corresponding zero-point energies per sulfur atom.

Functional	scale factor	s / cm^{-1}	s / eV (ZPE)
LDA	1.0085	11.57	0.00072
PBEsol	1.0201	12.39	0.00077
PBE0	0.9596	6.41	0.00040
B3LYP	1.0332	11.05	0.00068

6.3.3 Equilibrium model

Equilibrium compositions and free energies were computed as a function of temperature and pressure for all the data sets computed (Fig. 6.4 on the next page). There is significant disagreement between the predictions of the local exchange-correlation functionals LDA and PBEsol and the predicted composition from the hybrid functional PBE0, both before and after frequency scaling. While the "lower-level" calculations predict a diverse mixture of phases, hybrid DFT strongly supports the dominance of S_8 and S_2, at low and high temperatures respectively. In all cases, this simplicity is strongest at low total pressure. The other phases which are present in any significant quantity are the cyclic allotropes where $N = 4$–7, in the range 600–1000 K.

The corresponding free energies are also plotted in Fig. 6.5 on page 92; we note that agreement between the methods is much stronger at low temperatures where the mixture is dominated by larger molecules. This may be an artefact of aligning the free energies of the S_8 atoms; divergence in the energies of the smaller molecules leads to the disagreement at high temperatures. The other trend of note is the presence of a sharp bend in the μ–T curve, particularly at low pressure, corresponding to the presence of S_2 molecules. The point of onset depends on the data source, but the curve for PBE0 with empirical corrections closely tracks the minimum of the two curves from reference data. This represents a challenge to the formation of a simple parameterised model function, as it suggests the presence of a spike in the second derivative. Popular parameterisations of thermochemical properties, such as those in the NIST "WebBook", employ multiple temperature regions. This is usually viewed as a limitation, as it introduces non-physical discontinuities; with care, they could be aligned to an apparently physical discontinuity in the function. Taking the PBE0 results with empirical corrections as our preferred model, the free energy of the mixture is plotted with the chemical potentials of its component species on an atomic basis (Fig. 6.6 on page 92).

The depression in free energy due to mixing of allotropes and presence of minor components can be quantified by subtracting the chemical potential of the mixture from the minimum of the chemical potentials of the majority components S_2 and S_8. The resulting plot (Fig. 6.8 on page 95) shows that this has an impact ranging from around 1–4 kJ mol^{-1}, depending on the pressure. This is illustrated as a contour plot in Fig. 6.7 on page 93; within each unshaded region a single-phase model is adequate to within 1 kJ mol^{-1} S atoms.

6.3.4 Parameterisation

For convenience, a parameterised fit has been generated for the chemical potential of S over the T, P range 400–1500 K, –10^7Pa, incorporating an error function "switch" between S_2 and S_8 dominated regions and a Gaussian correction for the free energy depression where there is substantial mixing of phases. In eV per S atom, for T in K, the form of the parameterisation is

$$\mu_S(T,P) = \frac{1}{2}\left[\operatorname{erfc}\left(\frac{T-T_{tr}}{w}\right)\frac{\mu_{S_8}}{8} + \left(\operatorname{erf}\left(\frac{T-T_{tr}}{w}\right)+1\right)\frac{\mu_{S_2}}{2}\right] - a(P)\exp\left(-\frac{\left(T-T_{tr}+b\right)^2}{2c^2}\right) \tag{6.28}$$

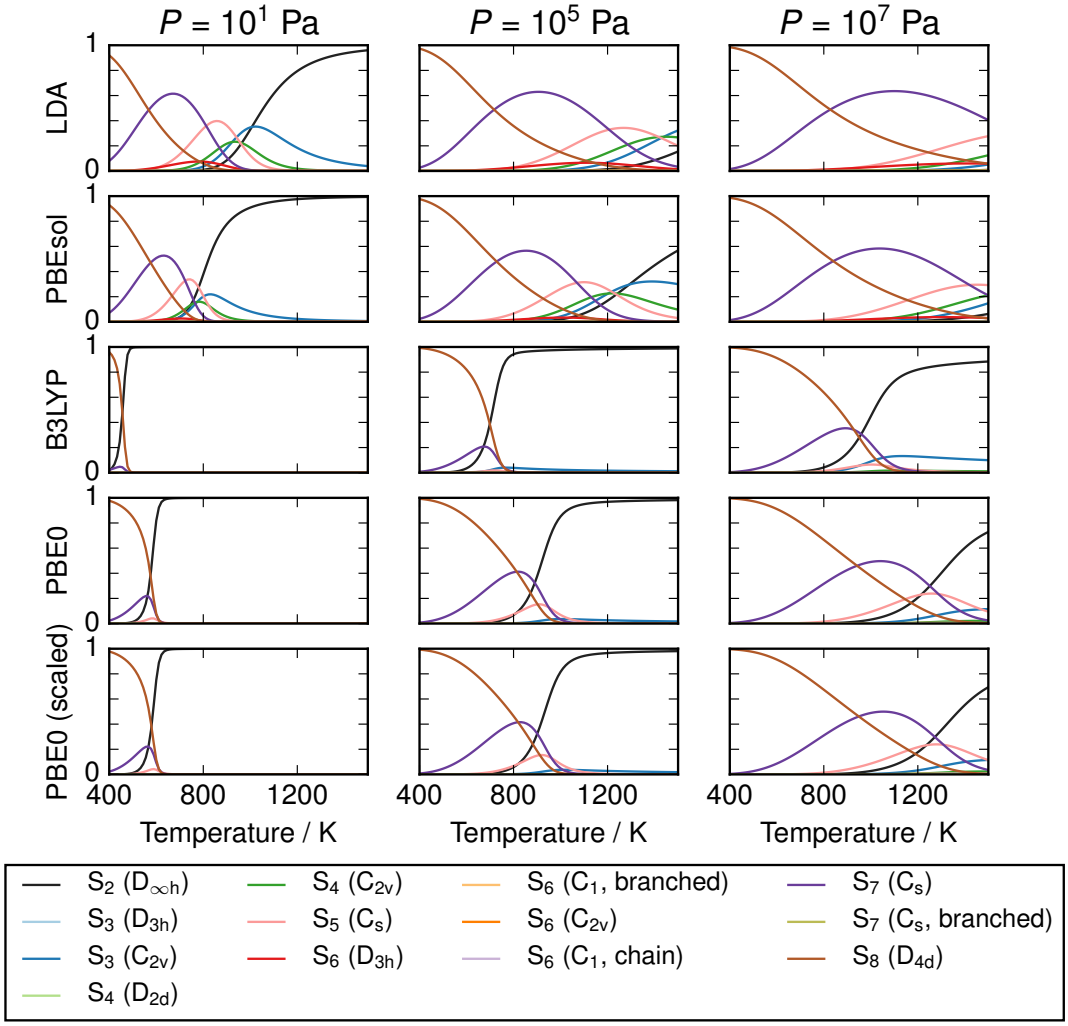

Figure 6.4 – Compositions of modelled S_x mixtures over range of equilibrium temperatures and pressures. Results are presented for density functional theory with one local (LDA), one semi-local (PBEsol) and two hybrid exchange-correlation functional (PBE0 and B3LYP), including empirical corrections for PBE0. Composition is given in units of atom fraction. It is expected that the most accurate results are obtained using PBE0 with scaled frequencies.

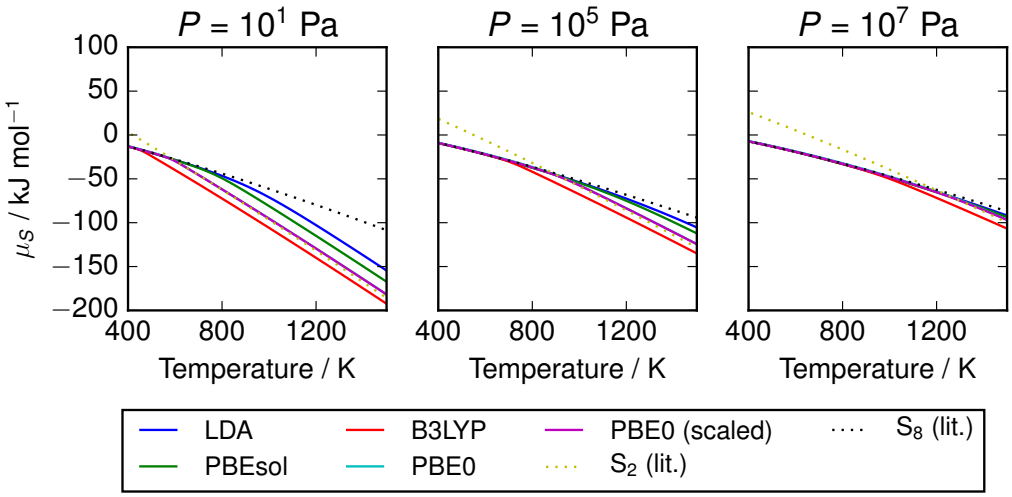

Figure 6.5 – Chemical potential of S vapours per mole of atoms, given at several pressures according to range of calculation methods. Data for S_2 and S_8 are also provided from the thermochemical literature.[3] At low pressures, the free energy diverges by more than 50 kJ mol^{-1} S atoms between the S_2 and S_8 allotropes at high temperatures, while at high pressures there is less variation. Results from hybrid DFT calculations with scaled frequencies closely track the minimal value from the literature, while the local and semi-local exchange correlation functionals diverge from this data due to over-estimation of the formation energy of S_2.

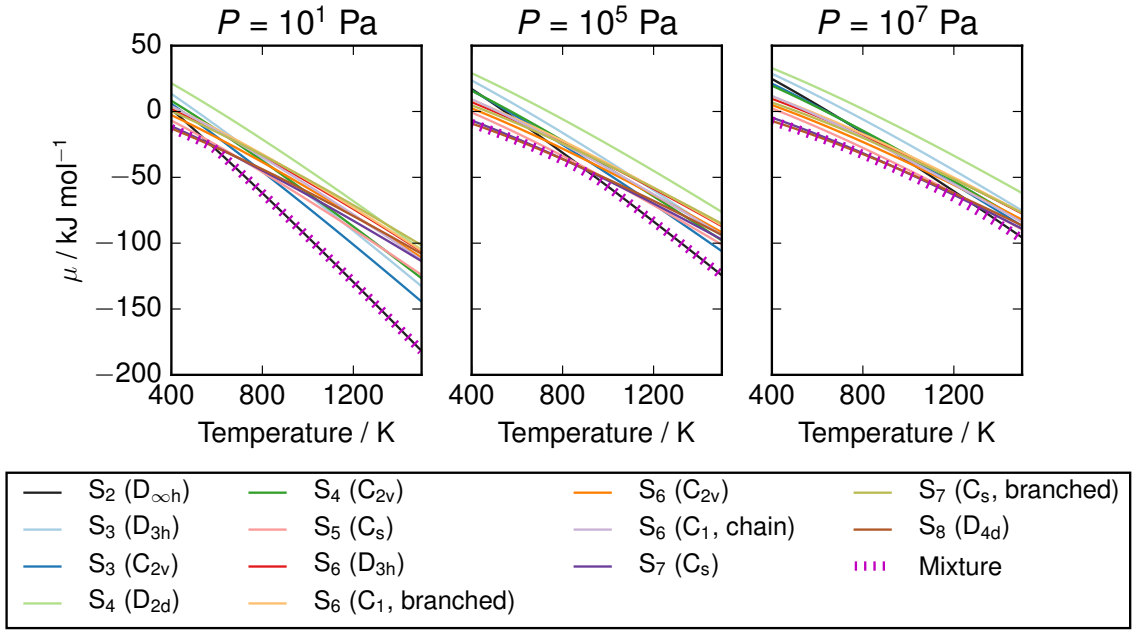

Figure 6.6 – Chemical potential of S vapours over range of T, P, compared with individual allotropes. The equilibrium mixture is lower in energy than any single allotrope, but in most T/P regimes lies close to the chemical potential of S_2 or S_8. Data from vibrational calculations with PBE0 and empirically-corrected frequencies.

Table 6.4 – Gibbs free energy of S vapours, tabulated from calculations with PBE0 and empirical corrections, with reference state (H=0) α-sulfur at 298.15 K. Energies in kJ mol^{-1}, column headers in $\log_{10}$(pressure/Pa). Tables are provided with more values and greater decimal precision in the supplementary information.

T/K	$\log_{10}(p/\mathrm{Pa})$									
	1.00	1.67	2.33	3.00	3.67	4.33	5.00	5.67	6.33	7.00
100	4.73	4.88	5.04	5.20	5.36	5.52	5.68	5.84	6.00	6.16
150	2.29	2.53	2.77	3.01	3.25	3.49	3.72	3.96	4.20	4.44
200	-0.39	-0.07	0.25	0.57	0.89	1.21	1.53	1.85	2.17	2.49
250	-3.27	-2.87	-2.47	-2.08	-1.68	-1.28	-0.88	-0.48	-0.08	0.32
300	-6.34	-5.86	-5.39	-4.91	-4.43	-3.95	-3.47	-2.99	-2.51	-2.03
350	-9.58	-9.02	-8.46	-7.90	-7.34	-6.78	-6.23	-5.67	-5.11	-4.55
400	-12.97	-12.33	-11.69	-11.05	-10.41	-9.77	-9.13	-8.49	-7.85	-7.21
450	-16.50	-15.77	-15.05	-14.33	-13.61	-12.89	-12.17	-11.45	-10.73	-10.01
500	-20.20	-19.37	-18.56	-17.75	-16.94	-16.14	-15.33	-14.53	-13.73	-12.93
550	-24.24	-23.17	-22.22	-21.31	-20.40	-19.51	-18.62	-17.73	-16.85	-15.96
600	-29.74	-27.46	-26.12	-25.03	-24.01	-23.01	-22.03	-21.05	-20.08	-19.11
650	-37.54	-33.52	-30.62	-29.01	-27.78	-26.65	-25.56	-24.49	-23.42	-22.36
700	-45.63	-41.17	-36.83	-33.61	-31.81	-30.45	-29.22	-28.04	-26.87	-25.72
750	-53.78	-49.00	-44.23	-39.63	-36.36	-34.48	-33.03	-31.71	-30.43	-29.18
800	-61.99	-56.89	-51.79	-46.72	-41.99	-38.90	-37.03	-35.51	-34.10	-32.74
850	-70.27	-64.84	-59.43	-54.02	-48.67	-44.06	-41.31	-39.46	-37.88	-36.39
900	-78.59	-72.85	-67.11	-61.38	-55.67	-50.16	-46.04	-43.61	-41.79	-40.15
950	-86.97	-80.91	-74.85	-68.80	-62.75	-56.78	-51.43	-48.04	-45.84	-44.01
1000	-95.39	-89.01	-82.64	-76.26	-69.90	-63.57	-57.48	-52.84	-50.06	-47.98
1050	-103.86	-97.17	-90.47	-83.77	-77.09	-70.43	-63.88	-58.14	-54.50	-52.07
1100	-112.38	-105.36	-98.34	-91.33	-84.32	-77.34	-70.42	-63.91	-59.21	-56.29
1150	-120.94	-113.60	-106.26	-98.93	-91.60	-84.29	-77.03	-70.00	-64.26	-60.68
1200	-129.53	-121.88	-114.22	-106.57	-98.92	-91.29	-83.70	-76.25	-69.65	-65.25
1250	-138.17	-130.19	-122.22	-114.24	-106.28	-98.33	-90.41	-82.60	-75.33	-70.03
1300	-146.84	-138.54	-130.25	-121.96	-113.67	-105.40	-97.16	-89.01	-81.23	-75.04
1350	-155.55	-146.93	-138.32	-129.71	-121.10	-112.51	-103.95	-95.46	-87.25	-80.27
1400	-164.29	-155.36	-146.42	-137.49	-128.57	-119.66	-110.77	-101.95	-93.36	-85.72
1450	-173.06	-163.81	-154.56	-145.31	-136.07	-126.84	-117.63	-108.49	-99.53	-91.33

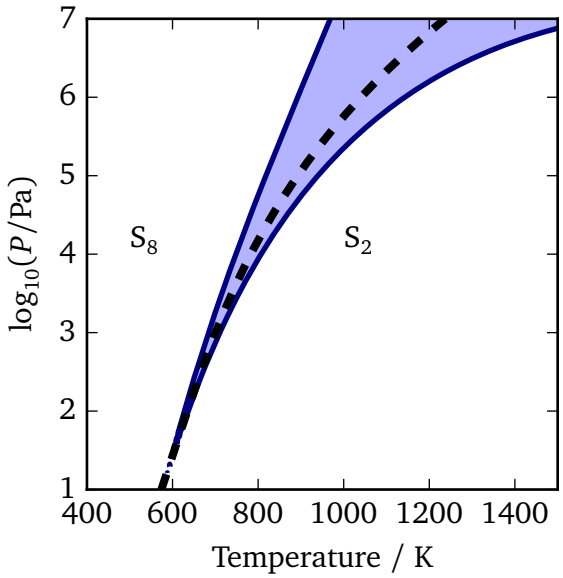

Figure 6.7 – Temperature-pressure map of approximations to free energy of mixture. At dashed line $\frac{1}{2}\mu_{S_2} = \frac{1}{8}\mu_{S_8}$; in shaded region the error in chemical potential μ associated with assuming a single phase S_2 or S_8 exceeds 1 kJ/mol S atoms; in unshaded regions the corresponding single-phase free energy is close to the energy of the mixture.

where

$$\begin{aligned}\mu_{S_8}(T,P) &= 7.620\times10^{-1} - 2.457\times10^{-3}T - 4.012\times10^{-6}T^2 \\ &\quad + 1.808\times10^{-9}T^3 - 3.810\times10^{-13}T^4 + k_B\ln\left(\frac{P}{1\,\text{bar}}\right), \\ \mu_{S_2}(T,P) &= 1.207 - 1.848\times10^{-3}T - 8.566\times10^{-7}T^2 \\ &\quad 4.001\times10^{-10}T^3 - 8.654\times10^{-14}T^4 + k_B\ln\left(\frac{P}{1\,\text{bar}}\right).\end{aligned}$$

T_{tr}, the transition temperature obtained by solving $\frac{1}{2}\mu_{S_2} = \frac{1}{8}\mu_{S_8}$ is approximated by the polynomial

$$T_{tr} = 5.077\times10^2 + 7.272\times10^1\log_{10}P - 8.295(\log_{10}P)^2 + 1.828(\log_{10}P)^3.$$

The height of the Gaussian correction

$$a(P) = 1.414\times10^3 - 2.041\times10^2\log_{10}P + 6.663\times10^1(\log_{10}P)^2,$$

and the more arbitrarily assigned width and offset parameters $b = 10$, $c = 80$, $w = 100$.

It is noted that this parameterisation contains many fitting parameters; however, given its physically-motivated form the resulting function is smooth and well-behaved over the region studied, while the fits to μ_{S_2}, μ_{S_8} and T_{tr} have some value in their own right. The fitting error is plotted in Fig. 6.9 on the facing page, and while somewhat irregular remains below 1 kJ mol^{-1}.

6.4 Conclusions

The chemical potential of sulfur vapours has been studied by solving the thermodynamic equilibrium of 13 gas-phase allotropes, including the dominant components S_2 and S_8. Thermochemical data was obtained from first-principles calculations and corrected with an empirical scaling factor for the vibrational frequencies. The transition between these dominating phases is highly pressure-dependent, and the free energy is further depressed at the transition temperature by the presence of additional phases, especially at elevated pressures. Selection of an inappropriate gas phase can lead to errors of the order 50 kJ mol^{-1} atoms, while the minor phases contribute free energy of the order 1 kJ mol^{-1} atoms. The resulting chemical potential data is made available through tabulated data, a parameterised model with error of the order 0.5 kJ mol^{-1} atoms and through open-source code; the reference energy is compatible with the NIST-Janaf thermochemical tables for the solid α-sulfur phase.[3] This phase is frequently used as a reference state for thermodynamic studies of defects and stability in metal chalcogenides; the application of this gas-phase potential may allow such studies to examine a wide range of reactions involving sulfur vapours, taking into account the equilibrium within the vapour phase. The selection of appropriate chemical potentials is also critical for the development and interpretation of phase diagrams.

6.5 Data Access Statement

The reference implementation of this model, complete with Python 2.7 code to generate all the plots in this paper as well as tabulated data in the form of Table 6.4, is available online at `https://github.com/WMD-Bath/sulfur-model` and a snapshot of the code at the point of submission of this article is hosted by Zenodo and available with the DOI:

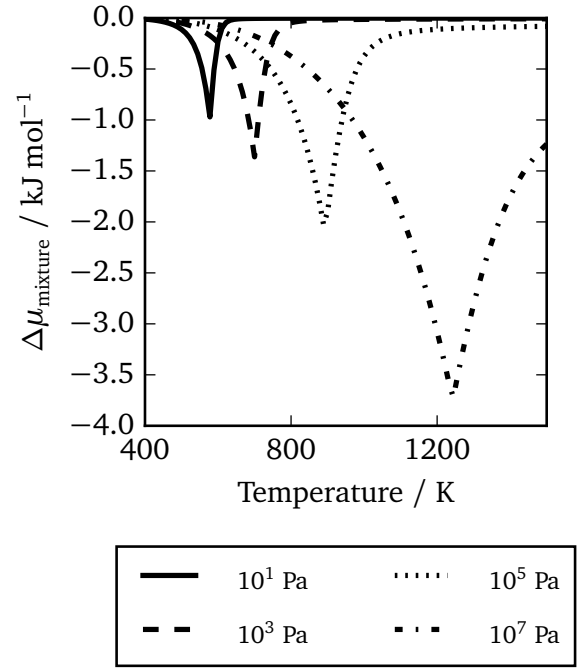

Figure 6.8 – Depression in chemical potential of sulfur vapour μ_S due to mixing and presence of minor allotropes. $\Delta\mu_{\text{mixture}} = \mu_S - \min\left(\frac{\mu_{S_2}}{2}, \frac{\mu_{S_8}}{8}\right)$

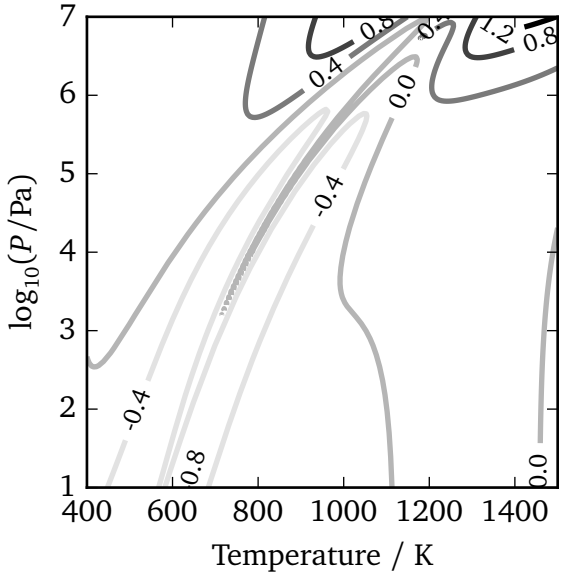

Figure 6.9 – Error of parameterisation in kJ mol^{-1}. Error is reduced to less than 1 kJ mol^{-1}, but is highly non-uniform. Parameterisation is recommended for convenient application over wide T–P ranges; the full equilibrium solution is required to correctly capture fine detail.

10.5281/zenodo.28536. In addition, full tables are provided with this paper in the ESI† for the composition, enthalpy and chemical potential from the calculations with PBE0 and empirical corrections; one set of enthalpy and chemical potential data follows Table 6.4 and uses the enthalpy of α-S as a reference energy (for use with other tabulated data) while the other employs the ground state of S_8 as a reference energy (for use with first-principles calculations.) The code and its dependencies are Free Software, using a range of licenses. Input and output files from DFT calculations with FHI-AIMS have been deposited with Figshare and are available with the DOI: 10.6084/m9.figshare.1513736. A set of data generated during the evolutionary search, consisting of candidate structures and the DFT energies used to rank them, has been deposited with Figshare and is available with the DOI: 10.6084/m9.figshare.1513833.

6.6 Acknowledgements

The authors thank J. M. Skelton and J. M. Frost for useful discussions. USPEX/VASP calculations with PBE were carried out using the University of Bath's High Performance Computing facilities. Hybrid DFT calculations were carried out using ARCHER, the UK's national high-performance computing service, via our membership of the UK's HPC Materials Chemistry Consortium, which is funded by EPSRC (grant no. EP/L000202). A.J.J. is part of the EPSRC Doctoral Training Center in Sustainable Chemical Technologies (grant no. EP/G03768X/1). The contribution of D.T. was supported by ERC Starting Grant 277757.

Bibliography

[1] W. Nehb and K. Vydra, *Sulfur*, 2000, http://doi.wiley.com/10.1002/14356007.

[2] G. N. Lewis and M. Randall, *J. Am. Chem. Soc.*, 1914, **36**, 2468–2475.

[3] M. J. Chase, *J. Phys. Chem. Ref. Data, Monogr.*, 1998, **9**, 1–1951.

[4] H. Rau, T. Kutty and J. Guedes De Carvalho, *J. Chem. Thermodynamics*, 1973, **5**, 833–844.

[5] P. Y. Yu and M. Cardona, *Fundamentals of Semiconductors*, Springer-Verlag Berlin Heidelberg, New York, 3rd edn., 2003.

[6] D. M. Berg, R. Djemour, L. Gütay, G. Zoppi, S. Siebentritt and P. J. Dale, *Thin Solid Films*, 2012, **520**, 6291–6294.

[7] M. Lichtenstriger, H. U. Bölsterli and R. Nitsche, *J. Phys. Chem. Solids*, 1961, **21**, 199–205.

[8] D. Colombara, S. Delsante, G. Borzone, J. Mitchels, K. Molloy, L. Thomas, B. Mendis, C. Cummings, F. Marken and L. Peter, *J. Cryst. Growth*, 2013, **364**, 101–110.

[9] L. A. Burton, D. Colombara, R. D. Abellon, F. C. Grozema, L. M. Peter, T. J. Savenije, G. Dennler and A. Walsh, *Chem. Mater.*, 2013, **25**, 4908–4916.

[10] A. J. Jackson and A. Walsh, *J. Mater. Chem. A*, 2014, **2**, 7829.

[11] V. Kosyak, N. B. Mortazavi Amiri, A. V. Postnikov and M. A. Scarpulla, *J. Appl. Phys.*, 2013, **114**, 124501.

[12] J. J. Scragg, T. Ericson, T. Kubart, M. Edoff and C. Platzer-Björkman, *Chem. Mater.*, 2011, **23**, 4625–4633.

[13] T. P. Martin, *J. Chem. Phys.*, 1984, **81**, 4426.

[14] R. Steudel, in *Studies in Inorganic Chemistry*, Elsevier, Amsterdam, 1984, vol. 5, pp. 3–37.

[15] D. Hohl, R. O. Jones, R. Car and M. Parrinello, *J. Chem. Phys.*, 1988, **89**, 6823.

[16] G. E. Quelch, H. F. Schaefer and C. J. Marsden, *J. Am. Chem. Soc.*, 1990, **112**, 8719–8733.

[17] M. W. Wong and R. Steudel, *Chem. Phys. Lett.*, 2003, **379**, 162–169.

[18] R. Steudel, Y. Stuedel and M. W. Wong, *Top. Curr. Chem.*, 2003, 117–134.

[19] W. Kohn and L. Sham, *Phys. Rev. A*, 1965, **140**, 1133–1138.

[20] J. Perdew, K. Burke and M. Ernzerhof, *Phys. Rev. Lett.*, 1996, **77**, 3865–3868.

[21] J. Perdew, A. Ruzsinszky, G. Csonka, O. Vydrov, G. Scuseria, L. Constantin, X. Zhou and K. Burke, *Phys. Rev. Lett.*, 2008, **100**, 136406.

[22] R. H. Hertwig and W. Koch, *Chem. Phys. Lett.*, 1997, **268**, 345–351.

[23] A. Becke, *J. Chem. Phys.*, 1993, **98**, 5648–5652.

[24] C. Adamo and V. Barone, *J. Chem. Phys.*, 1999, **110**, 6158.

[25] G. Kresse and J. Furthmüller, *Comput. Mater. Sci.*, 1996, **6**, 15–50.

[26] G. Kresse and J. Furthmüller, *Phys. Rev. B*, 1996, **54**, 11169–11186.

[27] V. Blum, R. Gehrke, F. Hanke, P. Havu, V. Havu, X. Ren, K. Reuter and M. Scheffler, *Comput. Phys. Commun.*, 2009, **180**, 2175–2196.

[28] V. Havu, V. Blum, P. Havu and M. Scheffler, *J. Comput. Phys.*, 2009, **228**, 8367–8379.

[29] A. R. Oganov and C. W. Glass, *J. Chem. Phys.*, 2006, **124**, 244704.

[30] A. R. Oganov, A. O. Lyakhov and M. Valle, *Acc. Chem. Res.*, 2011, **44**, 227–237.

[31] A. O. Lyakhov, A. R. Oganov, H. T. Stokes and Q. Zhu, *Comput. Phys. Commun.*, 2013, **184**, 1172–1182.

[32] J. P. Merrick, D. Moran and L. Radom, *J. Phys. Chem. A*, 2007, **111**, 11683–11700.

[33] I. M. Alecu, J. Zheng, Y. Zhao and D. G. Truhlar, *J. Chem. Theory Comput.*, 2010, **6**, 2872–2887.

[34] S. R. Bahn and K. W. Jacobsen, *Comput. Sci. Eng.*, 2002, **4**, 56–66.

[35] W. R. Smith and R. W. Nissen, *Chemical Reaction Equilibrium Analysis: Theory and Algorithms*, John Wiley & Sons, New York, 1982.

[36] S. R. Brinkley, *J. Chem. Phys.*, 1946, **14**, 563.

[37] J. S. R. Brinkley, *J. Chem. Phys.*, 1947, **15**, 107–110.

[38] W. B. White, *J. Chem. Phys.*, 1967, **46**, 4171.

[39] D. W. Marquardt, *J. Soc. Indust. Appl. Math.*, 1963, **11**, 431–441.

[40] *SciPy: Open source scientific tools for Python*, 2001, `http://www.scipy.org/`, [Online; accessed 2015-03-06].

[41] M. C. McCarthy, S. Thorwirth, C. A. Gottlieb and P. Thaddeus, *J. Am. Chem. Soc.*, 2004, **126**, 4096–4097.

[42] M. S. Boumedien, J. Corset and E. Picquenard, *J. Raman Spectrosc.*, 1999, **472**, 463–472.

[43] P. Hassanzadeh and L. Andrews, *J. Phys. Chem.*, 1992, **96**, 6579–6585.

[44] M. W. Wong, Y. Steudel and R. Steudel, *J. Chem. Phys*, 2004, **121**, 5899–5907.

[45] L. A. Burton and A. Walsh, *J. Phys. Chem. C*, 2012, **116**, 24262–24267.

Chapter 7

Lattice dynamics in the Cu-Zn-Sn-S system

In this chapter, calculated data is introduced for 17 crystalline phases in the Cu-Zn-Sn-S system. Some of this data was used in a paper published in 2014.[1] Since then a number of calculations have been revised to improve their accuracy, and new phases were added. The chapter has been written independently of the paper but there are some similarities.

In order to build up a phase diagram, it is necessary to collect a consistent set of thermodynamic data. In this work, each material considered for decomposition reactions and phase diagrams was modelled with all-electron DFT calculations using the PBEsol XC functional, as implemented in FHI-AIMS. PBEsol was selected to provide an appropriate ratio of accuracy to computational cost, given the considerable number of calculations required in this study. In the end, around 1.3 Mcore h of computer time were used in the course of this project across a variety of system architectures.

Initial structures for many phases were drawn from the inorganic crystal structure database (ICSD) operated by FIZ Karlsruhe, through access to the UK Chemical Database service; these are generally derived from X-ray diffraction studies, and the collection codes are provided where appropriate.[2;3] The basic set of parameters and methodology is summarised below. Where different parameters were required, this is noted on a per-material basis.

SUMMARY OF CALCULATION PARAMETERS
Quantum chemistry code FHI-AIMS
Basis set Atom-centred tabulated orbitals, "tight" or better
Exchange-correlation functional PBEsol
k-point cutoff At least 10 Å, larger in many cases
Occupation broadening Gaussian function with width 0.01 eV for semiconductors, 0.1 eV for metals
Structure optimisation procedure Modified BFGS procedure
Structure convergence threshold 0.001 eV $Å^{-1}$ $atom^{-1}$
Vibrational calculation framework Phonopy (supercell method)
Finite displacement size for vibrations 0.01 Å
Supercell dimensions Minimum 10 Å for each lattice vector

Table 7.1 – Summary of materials subjected to structure optimisation and vibrational study. Unit cell size is given in formula units (FU) and lattice vectors; lengths a, b, c are given in Å, angles α, β, γ are given in degrees. Non-typical **k**-point grid densities and extended basis sets are noted for some materials; these are detailed in the corresponding paragraphs of this section.

Formula	Space group	FU / unit cell	Initial						Optimised						Notes
			a	b	c	α	β	γ	a	b	c	α	β	γ	
CZTS	$I\bar{4}$	2	5.434	5.434	10.856	90.00	90.00	90.00	5.383	5.383	6.576	114.15	114.16	89.99	*a*
CZTS	$I\bar{4}2m$	1	6.709	5.454	5.454	90.00	113.99	113.99	6.594	5.374	5.375	89.99	114.08	114.07	*b*
Cu	$Fm\bar{3}m$	4	3.615	3.615	3.615	90.00	90.00	90.00	3.564	3.564	3.564	90.00	90.00	90.00	*c*
Zn	$P6_3/mmc$	2	2.665	2.665	4.947	90.00	90.00	120.00	2.614	2.614	4.775	90.00	90.00	120.00	*c*
Sn	$Fd\bar{3}m$	2	4.589	4.589	4.589	60.00	60.00	60.00	4.624	4.624	4.624	120.00	90.00	120.00	*d*
Sn	$I4_1/amd$	2	3.182	4.419	4.419	97.45	68.90	111.10	4.406	4.406	4.406	97.49	97.49	137.67	*d*
S	$Fddd$	32	14.349	14.237	7.885	74.74	73.21	32.01	13.788	13.283	8.335	75.15	68.51	36.02	*e*
Cu_2S	$P2_1/c$	48	15.246	11.884	13.494	90.00	116.35	90.00	14.870	11.744	13.095	90.00	115.97	90.00	*e*
ZnS	$F\bar{4}3m$	1	3.822	3.822	3.822	60.00	60.00	60.00	3.789	3.789	3.789	59.98	59.98	59.98	*e*
ZnS	$P6_3mc$	2	3.811	3.811	6.234	90.00	90.00	120.00	3.783	3.783	6.209	89.98	90.02	120.00	*f*
SnS	$Pnma$	4	11.184	4.012	4.159	90.00	90.00	90.00	11.083	3.982	4.229	90.00	90.00	90.00	*g*
SnS_2	$P\bar{3}m1$	1	3.605	3.605	5.460	90.00	90.00	120.00	3.649	3.649	6.017	90.00	90.00	120.00	*g,h*
Sn_2S_3	$Pnma$	4	8.878	3.751	14.020	90.00	90.00	90.00	8.785	3.772	13.802	90.00	90.00	90.00	*g*
Cu_2SnS_3	Cc	4	6.710	11.620	6.740	90.00	70.33	90.00	6.597	11.425	6.617	90.01	70.41	90.00	
Cu_2SnS_3	$Imm2$	1	3.920	5.430	6.702	113.90	107.01	90.00	3.852	5.338	6.596	113.91	107.03	90.01	
Cu_3SnS_4	$Pmn2_1$	2	7.426	6.452	6.163	90.00	90.00	90.00	7.457	6.458	6.231	90.00	90.00	90.00	*g*
Cu_4SnS_4	$Pnma$	4	13.558	7.685	6.41	90.00	90.00	90.00	13.284	7.544	6.396	90.04	90.00	90.00	

a. Ref. 4, Reduced from conventional cell to primitive *b.* Primitive cell, low **k**-points *c.* High **k**-points, ext. basis *d.* Primitive cell reconstructed from optimisation with VASP and optimised by curve-fitting; high **k**-points *e.* Loose forces *f.* Irregular **k**-point grid used; 6×6×6 where 6×6×4 corresponds to 10 Å cutoff. Phonons at 10 Å cutoff. *g.* Increased **k**-points *h.* Extra-tight forces; large supercell

7.1 Crystalline phases

7.1.1 Quaternary phases — CZTS

Structure optimisation and phonons were calculated for both the kesterite and stannite structures of CZTS. Initial structures were provided by the authors of Ref. 4. The stannite phase was reduced to the primitive cell using Spglib before optimisation, while the kesterite phase was optimised as a conventional cell before symmetry reduction.[5] A relatively low number of **k**-points was used for the stannite phase, corresponding to a 9 Å cutoff. The phonon band structure and DOS for each is given in Figs. 7.2a and 7.2b. The DOS for each appear to be very similar. LO–TO splitting was not included; another study comparing the lattice dynamics of these phases with the PBE functional included this effect, leading to discontinuities of the order 10 cm^{-1} in the frequencies of some modes at the Γ-point.[6]

CZTS has been extensively studied with Raman spectroscopy, and a full set of 11 frequencies has been assigned under excitation with a 514 nm laser.[7] The high-intensity modes at 287 cm^{-1} and 337 cm^{-1} were assigned as the "A" symmetry modes. Examining the corresponding eigenvectors in the harmonic approximation calculations, these are modes which involve all the sulfur anions but there is no corresponding movement on the cation sub-lattice. This would explain the relatively smooth disappearance of the higher-frequency peak and replacement by a lower-frequency peak when S atoms are substituted for Se.[8] Experiments with thin films have not shown significant shifts in frequencies, suggesting that study of vibrations in the bulk is transferable to device characterisation.[9]

Figure 7.1 illustrates the normal modes of kesterite CZTS, with the frequencies from calculations within the harmonic approximation using PBEsol. The A-modes with calculated frequencies 291 cm^{-1}, 295 cm^{-1} and 317 cm^{-1} take place solely on the anion sub-lattice, and are represented by the movement of S atoms. Their relatively high frequency is explained by the low mass of sulfur; the E-modes computed at 158 cm^{-1} and B-mode at 171 cm^{-1} involve similar movements on the cation sub-lattice.

More sophisticated methods than the harmonic approximation have been applied to CZTS, including the quasi-harmonic approximation (QHA) and the computation of phonon-phonon interactions.[10] However, while these methods may offer slightly more accurate vibrational properties, for the purposes of this thesis we rely on calculations with PBEsol within the harmonic approximation. This is justified as a reliance on "error cancellation"; incorporating higher-order effects would likely lead to some systematic changes in the energies of materials, and in this case the error of reaction energies would increase when mixing harmonic and quasi-harmonic calculations.

7.1.2 Elemental materials

Copper

An initial unit cell for copper was obtained from the ICSD (collection code 64699): an FCC cell with lattice parameter 3.615 Å. A relatively-high **k**-point cutoff of 20 Å was used, corresponding to a 12×12×12 Γ-centred mesh, with the full "tier 2" basis set in FHI-AIMS. This contracted slightly on optimisation with PBEsol to 3.564 Å. The resulting phonon band structure (Fig. 7.3a) agrees well with a study in the literature which compares LDA, PBE and PBEsol phonon dispersion with experimental data from inelastic neutron scattering; in that work the PBEsol-calculated frequencies lie between those of LDA and PBE, close to the experimental values.[11]

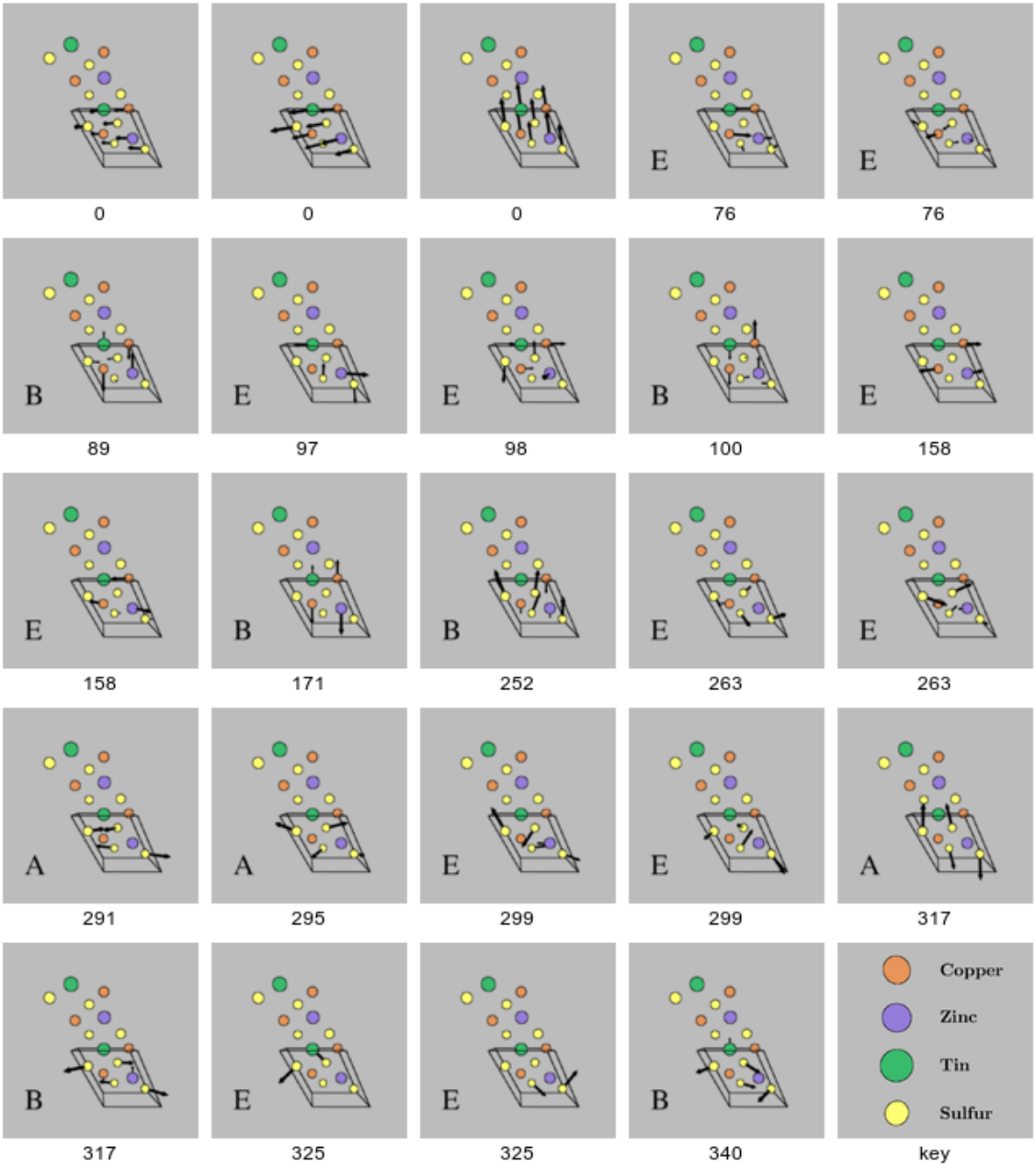

Figure 7.1 – Visualisation of phonon eigenvectors in kesterite CZTS. Frequencies are given in cm^{-1}; the size of arrows is proportional to the magnitude of the eigenvectors. The labels in the bottom-left of each panel are the mode symmetries; these were assigned by Mirjana Dimitrievska according to the $I\bar{4}$ character table. White box shows bounding unit of primitive cell. This figure has previously been published as part of an academic paper.[10] An animated version is available online at `http://dx.doi.org/10.1063/1.4917044.1`.

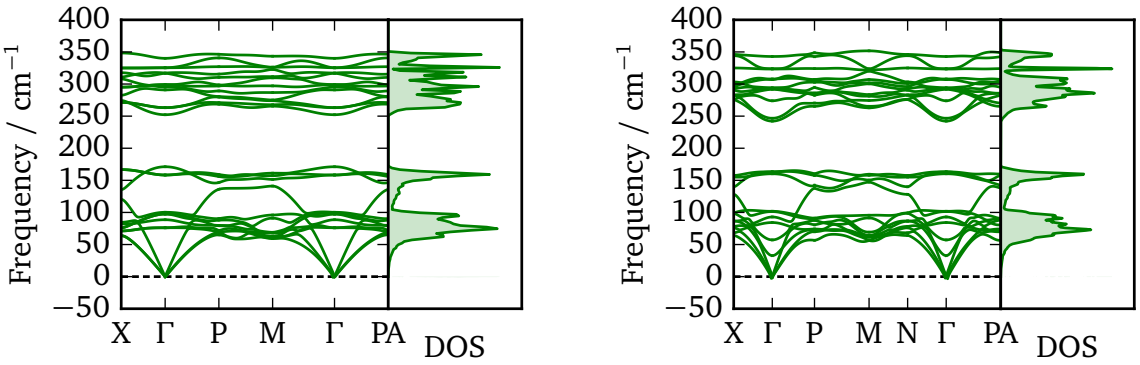

(a) Kesterite **(b)** Stannite

Figure 7.2 – Phonon dispersion with density of states for (a) kesterite ($I\bar{4}$) and (b) stannite ($I\bar{4}2m$) Cu_2ZnSnS_4.

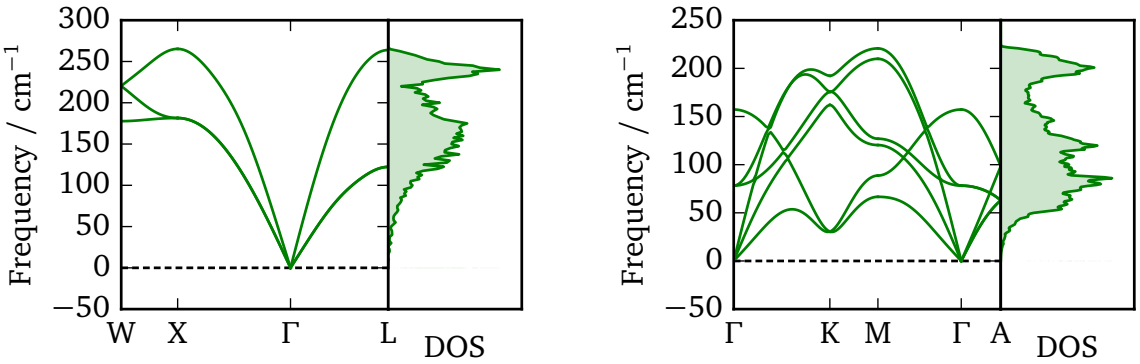

(a) Cu **(b)** Zn

Figure 7.3 – Phonon dispersion with density of states for (a) $Fm\bar{3}m$ metallic Cu and (b) $P6_3/mmc$ metallic Zn.

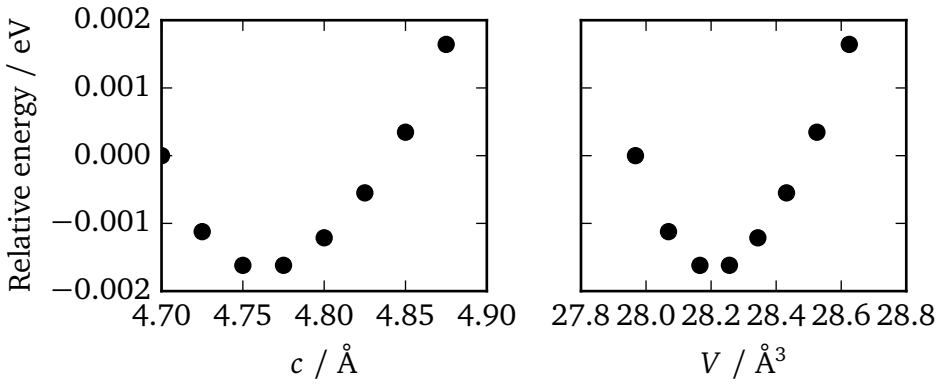

Figure 7.4 – Equation of state curve for Zn metal, showing energy dependence on lattice parameter c and corresponding volumes where other lattice vectors are constrained to be orthogonal to c.

Zinc

The initial structure for zinc, a 2-atom unit cell in a hexagonal close-packed arrangement, was obtained from the ICSD (collection code 64990). Some experimentation with the basis-set, **k**-point mesh density and lattice parameters was needed for smooth convergence; the final parameters were a 24 Å **k**-point cutoff and 2 additional basis functions over the "tight" set. DFT study of Zn is known to be problematic, due to its easily polarisable d shell.[12] An energy-volume (E-V) curve (Fig. 7.4) was generated by fixing the c lattice parameter and constraining relaxation of the a and b parameters to generate a series of structures. The lattice parameters a=2.61408 Å and $b = c$ =4.77500 Å were used to generate a high symmetry unit cell for phonon calculations. The resulting phonon dispersion (Fig. 7.3b) is in close agreement with that produced by neutron measurements at 80 K, with the principle difference being a slight softening in the frequencies at point K (Fig. 7.5).[13]

Tin

Tin has two solid phases: α-Sn or "grey tin" and β-Sn or "white tin". At atmospheric pressure, the transition from α-Sn to β-Sn occurs at temperatures above 13.2 °C, and the melting point lies near 232 °C.[14] This is somewhat problematic when determining reaction energies at realistic conditions, and in practice β-Sn is generally preferred. Liquid Sn has been observed to form part of the CZTS phase equilibrium when working with electroplated metal stacks.[15] Modelling liquids is difficult within DFT, and typically involves molecular dynamics (MD) calculations with a large simulation region. This phase was neglected in this work, but its possible presence must be noted.

Initially, the same optimisation procedure was employed as with other phases; structures were drawn from the ICSD for both α-Sn (collection code 70128) and β-Sn (collection code 40037) and reduced to their 2-atom primitive unit cells. These were optimised with PBEsol using the modified BFGS algorithm implemented in FHI-AIMS, with an extended **k**-point cutoff of 26 Å following convergence testing. An inconsistency emerged between these calculations and the known phases of Sn; the ground-state energy from calculations with PBEsol was 0.0284 eV *lower* for β-Sn, the "high-temperature" phase, than for α-Sn. Previous attempts to determine the difference in ground state energy have included early non-relativistic DFT calculations, extrapolation from heat capacity data, density functional perturbation theory (DFPT) and more recent automatic calculations for materials databases.[16–19]

To investigate this further and rule out any implementation-related artefacts, a new set of calculations was performed with the VASP DFT code. After checking the basis-set and **k**-point convergence, the α-Sn and β-Sn structures were optimised with the LDA, PBE and PBEsol

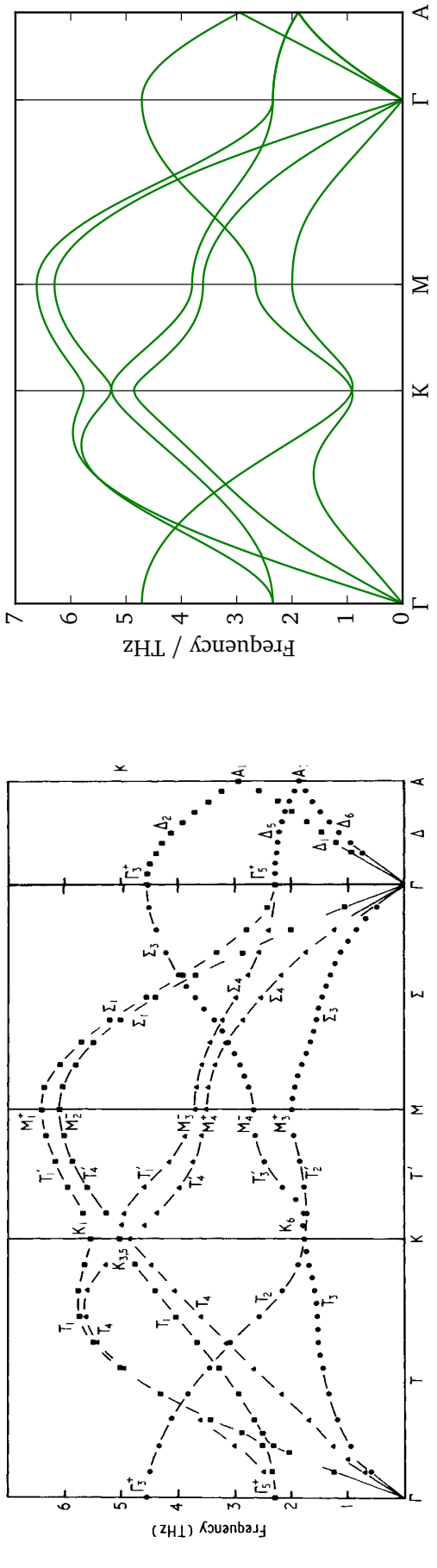

Figure 7.5 – Phonon band structure of Zn (space group $P6_3/mmc$); comparison between data from (a) neutron experiments (digital composite of figures 3 and 5 from original paper);[13] and (b) all-electron DFT calculations with PBEsol. (This is the same data as Fig. 7.3b, re-plotted in THz).

XC functionals. It is worth noting that this optimisation maintained the symmetry of the cells exactly, which is not possible with the FHI-AIMS optimisation tools. The results of these calculations (Table 7.2) confirmed that the ground-state energies are very close, leading to a small formation energy which is quite sensitive to the calculation method. The incorrect ordering in the PBEsol-derived results could be artificially corrected by adjusting the ground-state energy to reproduce the known transition temperature, but we have not done so — in any case, the Cu-Zn-Sn-S phase equilibrium envelope of interest lies at high temperatures where α-Sn is never found.

SUMMARY OF CALCULATION PARAMETERS
Quantum chemistry code VASP
Basis set Plane waves, 500 eV cutoff
Pseudopotentials "Sn_d" ultra-soft pseudopotentials; 14 electrons treated explicitly per Sn atom
Exchange-correlation functional LDA, PBE, PBEsol
k-point cutoff 30 Å,
Occupation broadening Gaussian function with width 0.05 eV for α-Sn, 0.1 eV for β-Sn.
Structure optimisation procedure Conjugate gradient optimisation of internal positions and lattice parameters
Structure convergence threshold 10^{-4} eV Å^{-1} atom^{-1}

Table 7.2 – Ground-state formation energy of β-Sn from various sources. Two values are drawn from high-throughput materials databases the Materials Project[18] and Open Quantum Materials Database.[19]

Data source	$E_{0,\beta\text{-Sn}} - E_{0,\alpha\text{-Sn}}$ / eV
LDA (this work)	−0.018
PBE (this work)	0.041
PBEsol (this work)	−0.027
DFT (LDA assumed)[16]	0.04
C_ν data[16]	0.015
DFPT (LDA assumed)[17]	0.022
PBE (Materials Project, ID mp-84)	0.047
PBE (OQMD, ID 674229)	0.042

For the final set of phonon calculations, high-symmetry cells were used with FHI-AIMS by fitting the lattice parameters to equations of state. Beginning with the VASP-optimised lattice parameters, this further step was taken to ensure that there would be no negative phonon frequencies when replacing pseudopotentials with an all-electron calculation. α-Sn in space group $Fd\bar{3}m$ has a single degree of freedom, and the lattice parameter $a = 6.5364$ Å was adjusted to 6.5391 Å by fitting the unit cell volume and energy to the Murnaghan equation of state

$$E(V) = E(V_0) + k_0 V_0 \left(\left(\frac{V}{V_0} \right)^{1-k_0'} \cdot \frac{1}{k_0'(k_0'-1)} + \frac{V}{k_0' V_0} - \frac{1}{k_0'-1} \right) \tag{7.1}$$

where V_0 is the volume with minimal energy $E(V_0)$ and k_0, k'_0 are fitting parameters. This was carried out across two iterative steps to converge the total energy to within 10^{-4} eV (Fig. 7.6). There are two degrees of freedom for Sn in the $I4_1/amd$ space group, so the β-Sn structure was obtained by fitting a mesh of a and c values to a 2-D quadratic function. The minimum of this function was used to estimate new lattice parameters and the process repeated until the total energy was converged to within 10^{-5} eV (Fig. 7.8).

Lattice dynamics were computed with $3 \times 3 \times 3$ supercells, yielding clean phonon band structures with no imaginary frequencies (Fig. 7.7). The α-Sn dispersion appears similar to existing

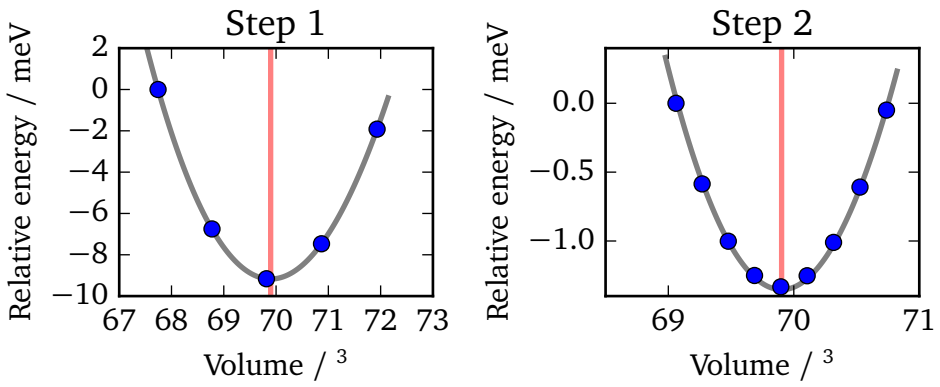

Figure 7.6 – 2-step optimisation of α-Sn lattice by fitting energy–volume relationship of 2-atom primitive cell. Blue points indicate calculated energies; grey line is fit to Murnaghan equation of state; vertical red line indicates volume at energy minimum of fit. Energies are expressed relative to the maximum value in each set of calculations.

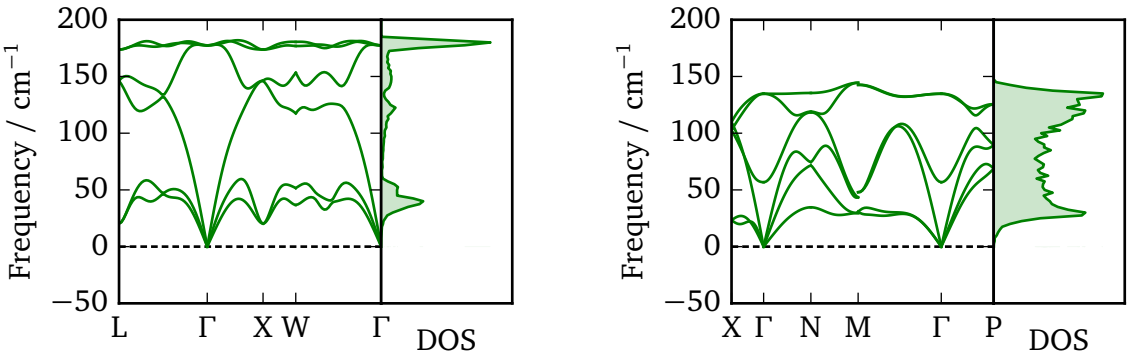

(a) α-Sn **(b)** β-Sn

Figure 7.7 – Phonon dispersion with density of states for (a) α ($Fd\bar{3}m$) and (a) β ($I4_1/amd$) phases of tin.

results from neutron scattering and DFPT; one acoustic mode is a little soft at X and the computed optic modes at Γ lie 20 cm^{-1} below the expected value, but all the other modes at X are within 10 cm^{-1} of experiment.[17;20] The frequencies for β-Sn are in reasonable agreement with published data based on measured elastic constants, inelastic neutron scattering and DFPT, with the Γ-point optic mode around 135 cm^{-1}.[17;21;22]

Sulfur

While sulfur has an extraordinary variety of solid allotropes, orthorhombic α-sulfur is generally taken as the reference state, being stable at standard conditions and historically the subject of much study.[23] A primitive unit cell for α-S, containing 32 atoms, was obtained from previous theoretical work using PBEsol; the full *Fddd* conventional cell contains 256 atoms.[24] The **k**-point spacing corresponded to a 13 Å cutoff and force minimisation was limited to 10^{-2} eV $Å^{-1}$ due to the very slow convergence of this molecular solid. The dispersion plot (Fig. 7.9) reveals very flat bands; this is consistent with a large unit cell, suggesting that local interactions dominate over longer-range behaviour.

As α-S is a molecular solid, there is a risk that the binding energy will be under-estimated by local XC functionals such a PBEsol which do not include long-range corrections. Table 7.3 shows a few properties computed with these results; the heat capacity and relationship with S_2 resemble the experimental values but the formation energy of S_8 is too low. As an alternative, it is possible to use a molecular phase of sulfur as the reference state and calculate the corresponding α-S reference by using experimental formation enthalpies, i.e.

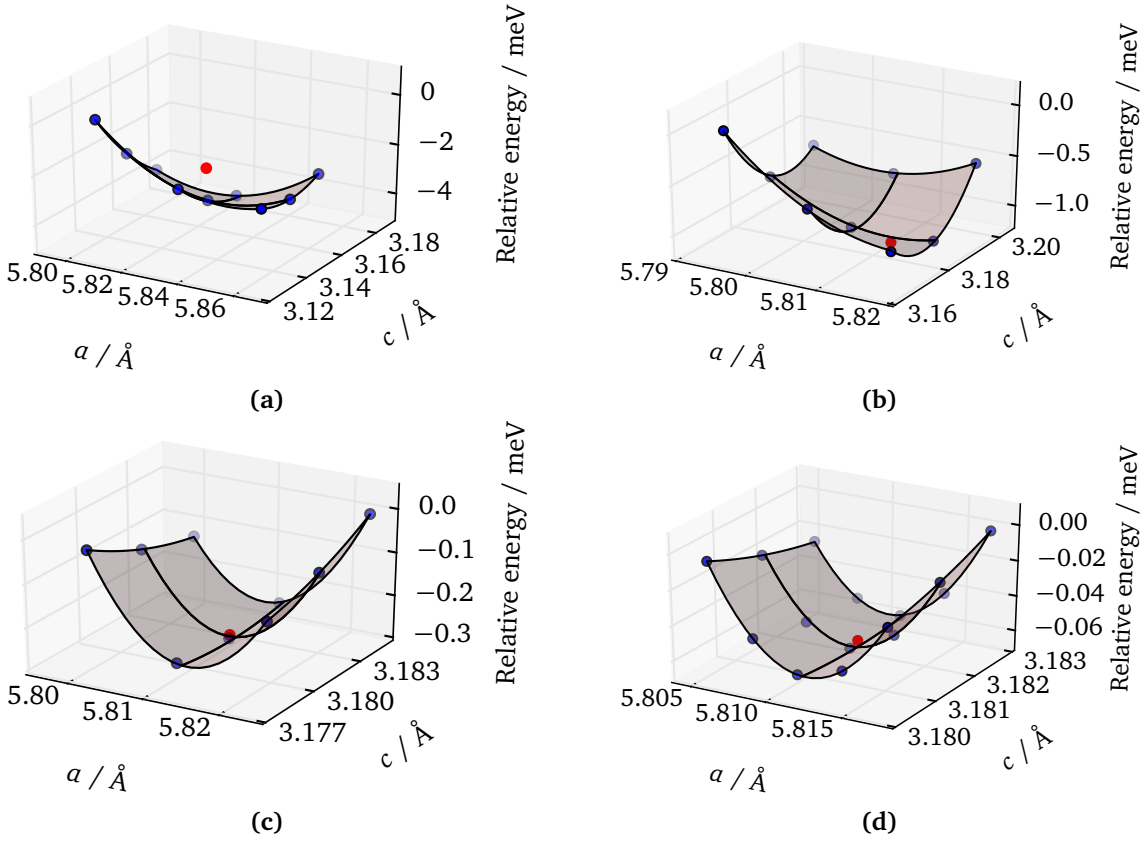

Figure 7.8 – Optimisation of β-Sn lattice parameters. (a)–(d) are steps in which the energy–lattice relationship is fitted to the 2-D quadratic function $E_0 = p_0 + p_1 a + p_2 c + p_3 a^2 + p_4 ac + p_5 c^2$. (a)–(c) use sets of 9 calculations over successively small regions, (d) uses 15 calculations to confirm quadratic nature of c-axis relationship. Blue points indicate calculated energies while the fitted 2-D function is plotted as a grey surface. The lattice parameters at the estimated energy minimum, shown as a red point, are used to initialise the next set of calculations. Energies are displayed relative to the highest value in each calculation set.

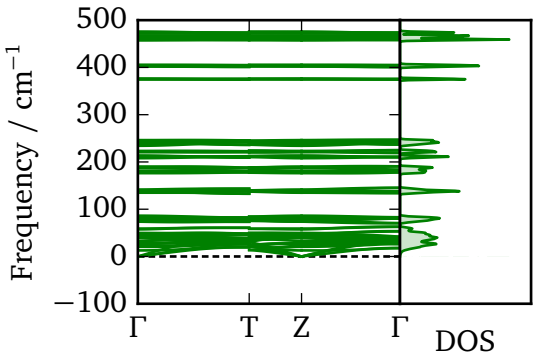

Figure 7.9 – Phonon dispersion with density of states for α-S.

Table 7.3 – Thermochemical values derived from PBEsol study of α-S are compared with reference data.[25] C_p is the constant-pressure heat capacity (the calculated value used here is a constant-volume heat capacity as lattice expansion effects were neglected); enthalpy changes at standard conditions ($\Delta H^{\ominus}$, 298.15 K, 10^5 Pa) and zero temperature (ΔH^0) are given for the formation of gaseous S_8 and S_2 gas molecules from α-S using the same reference data for temperature/ZPE corrections to the computed ground-state energies.

Property	Calculated	Ref. / kJ mol^{-1}
$C_{p,\alpha-S} \times 10^3$K	21.8	22.7
$\Delta H^{\ominus}_{f,S_8}$	18.7	100.4
$\Delta H^{0}_{f,S_8}$	22.8	104.4
$\Delta H^{\ominus}_{f,S_2}$	131.5	128.6
$\Delta H^{0}_{f,S_2}$	131.3	128.3

Table 7.4 – Standard formation enthalpies of binary compounds, computed with different S reference states. The standard formation enthalpy of the compound MS_x is always computed $H^{\ominus}_{MS_x} - xH^{\ominus}_{\alpha\text{-S}} - H^{\ominus}_{M}$. The ground-state energy of α-S is formed as (a) $E^{\text{PBEsol}}_{\alpha\text{-S}}$, (b) $\frac{1}{8}E^{\text{PBEsol}}_{S_8} - \Delta H^{\text{expt}}_{f,S_8}$ and (c) $\frac{1}{2}E^{\text{PBEsol}}_{S_2} - \Delta H^{\text{expt}}_{f,S_2}$. Experimental values are provided for comparison.[14;26] All values are given in kJ mol^{-1}.

Compound	α-S ref.	S_8 ref.	S_2 ref.	Expt.
ZnS	−156.7	−146.0	−158.4	−196(4)
Cu_2S	−43.4	−32.7	−45.0	−79.5
SnS	−94.8	−84.1	−96.4	−100.0

$$H^{\ominus}_{\alpha-S} = -\left(\frac{H^{\ominus}_{S_x}}{x} - H^{\ominus}_{\alpha-S} - \frac{H^{\ominus}_{S_x}}{x}\right) \tag{7.2}$$

$$H^{\ominus}_{\alpha-S} = \frac{H^{\ominus}_{S_x}}{x} - \frac{\Delta H^{\ominus}_{f,S_x}}{x} \tag{7.3}$$

$$H^{\ominus,\text{DFT}}_{\alpha-S} \approx \frac{H^{\ominus,DFT}_{S_x}}{x} - \frac{\Delta H^{\ominus,\text{expt}}_{f,S_x}}{x}. \tag{7.4}$$

Comparing binary formation energies computed with each of these reference states in Table 7.4, the thermochemical models of α-S and S_2 both give more realistic values than S_8, suggesting that this species is more problematic.

The sulfur state used for modelling of reactive annealing is the universal chemical potential developed in Chapter 6, computed using PBE0 with empirical corrections. An argument exists for using the data computed with PBEsol, in order to benefit from error cancellation; however, in this case the PBE0 XC functional with empirically-scaled frequencies gave the most realistic results. Application of the recommended data-set is considered to be equivalent to the use of thermochemical reference data, as in *ab initio* studies of oxidation and oxygen defect formation.[27–29] The reference energies need to be correctly aligned in order to use this data with the PBEsol calculations reported in this section.* While the tabulated data reported in that work was given relative to the enthalpy of α-sulfur, for ease of use with typical formation energy data, the supporting data and accompanying code includes alternative free energy

*In principle, all-electron energies computed with sufficiently high-quality DFT functionals would be interchangeable if they used a standard reference state such as non-interacting electrons. Such a functional has yet to be developed, and in practice DFT calculations depend on the cancellation of errors.

tables relative to S_8. Given the concerns expressed above regarding the use of PBEsol with the S_8 species, an additional set of tables has been generated using S_2 as the reference species.

7.1.3 Binary compounds

Copper sulfide

Copper sulfide with 2:1 stoichiometry is known as "chalcocite". While Cu_2S is easily detected with XRD, it is not generally observed in CZTS films; this is presumably due to the Cu-poor stoichiometry used in the majority of experiments.[30] The low-temperature $P2_1/c$ phase is well-defined with a large 144-atom monoclinic unit cell. Xu *et al.* carried out a computational study of the three Cu_2S phases: low-, high- and cubic-chalcocite.[31] Previously-reported crystallographic structures for chalcocite were derived from X-ray diffraction measurements and in the high-temperature phase some sites are assigned to more than one species. These are meaningless in atomistic or electronic structure calculations, and the computational work attempted to fill this knowledge gap by finding low-energy 2×2×2 supercells containing 144 atoms. Through correspondence with the authors we have obtained their structure for low-chalcocite, which has broadly the same positions as other structures in the literature but with substantial distortions. It was not possible to obtain the higher-energy structures. The difference in formation energy between the different phases is of the order 0.05 eV per formula unit, with phase transitions at 104 °C and 436 °C.[31] Due to the difficulty and cost of calculations with such a large unit cell, the **k**-point cutoff was 10 Å and the force criterion for geometry optimisation was loosened to 10^{-2} eV Å^{-1}.

Zinc sulfide

Zinc sulfide has long been of interest to crystallographers; its low- and high-temperature phases are eponyms for the zincblende and wurtzite crystal structures, respectively. The initial geometry for the zincblende ($F\bar{4}3m$) structure was constructed as a 2-atom primitive cell from the reference lattice parameter 5.4053 Å.[32] The **k**-point cutoff was 10 Å and force criterion for geometry optimisation was 10^{-2} eV Å^{-1}. The symmetry was slightly broken by relaxation and the $R3m$ space group was assumed when applying symmetry-reduction to form a set of supercell displacements; however, the resulting dispersion plot (Fig. 7.10a) uses the high-symmetry **k**-points of an $F\bar{4}3$ primitive cell without issue, while the lack of imaginary modes suggests that the geometry optimisation was sufficient.

An initial structure was obtained for the wurtzite phase (space group $P6_3mc$) from the ICSD (collection code 41489). This high-symmetry structure has no primitive cell, and yields a relatively complex phonon dispersion plot (Fig. 7.10b).

Raman spectroscopy is used to identify ZnS secondary phases in CZTS samples, and the key "fingerprint" is an A-mode frequency shift from 286 cm^{-1} to 290 cm^{-1}.[30] The optic mode at 350 cm^{-1} is also present in CZTS, but can still be used to identify ZnS impurities; exciting the system with a high-frequency laser increases the intensity of this mode in a distinctive way.[33–35]

Tin sulfides: SnS, SnS_2, Sn_2S_3

The stable $Pnma$ phase of SnS was included in the study; the structure was drawn from a recent theoretical study with PBEsol, and optimised to the calculation methods employed here.[24] We note that the initial parameters are within 2% of the experimental lattice parameters, suggesting that PBEsol provides a reasonable description of this material. The same study

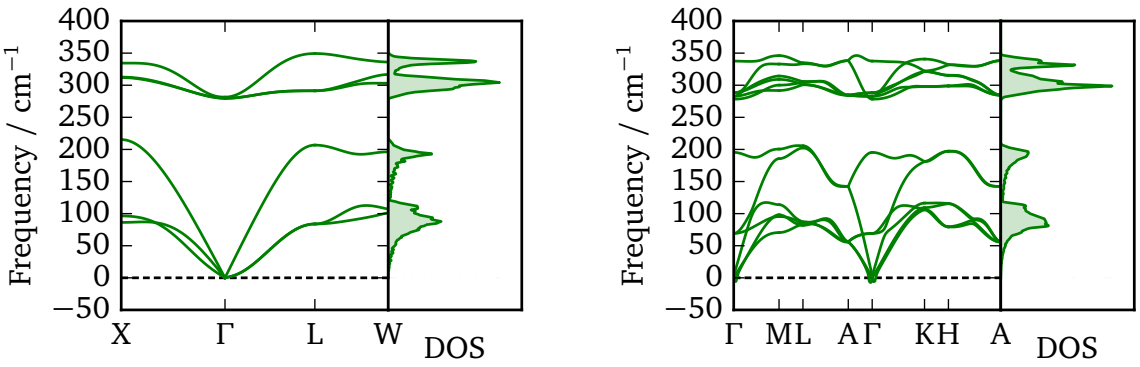

(a) Zincblende **(b)** Wurtzite

Figure 7.10 – Phonon dispersion with density of states for ZnS in (a) zincblende ($F\bar{4}3m$) and (b) wurtzite ($P6_3mc$) phases.

Table 7.5 – Reported phases of copper tin sulfide: stoichiometry; space group; lattice parameters in Å and degrees (at reported precision); availability of atom site assignment; citation number in bibliography.

Stoich.	space group	a	b	c	α	β	γ	positions?	Ref.
Cu_2SnS_3	$I\bar{4}2m$	5.412		10.810	90	90	90		36
Cu_2SnS_3	$F\bar{4}3m$	5.434			90	90	90		36
Cu_2SnS_3	Cc	6.71	11.62	6.74	90	70.33	90	✓	38
Cu_2SnS_3	$Imm2$	11.61	3.92	5.43	90	90	90	✓	38
Cu_3SnS_4	$Pmn2_1$	6.532	7.506	37.762	90	90	90		36
Cu_3SnS_4	$Pmn2_1$	7.667	6.440	6.261	90	90	90	✓	39
Cu_4SnS_4	$Pnma$	13.558	7.685	6.41	90	90	90	✓	40

discredited the existence of bulk-phase zincblende ($F\bar{4}3$) SnS, which is not included. The vibrational properties were obtained using standard parameters (Fig. 7.11a).

The initial structure for SnS_2 was drawn from the ICSD (collection code 100612). Very fine convergence was needed to avoid negative phonon modes; the forces were reduced to less than 10^{-4} eV Å^{-1} and a large (4×4×3) supercell was used to obtain the phonon frequencies. The same procedure was applied for Sn_2S_3 (ICSD collection code 31995, $2 \times 3 \times 1$ supercell).

The Raman spectra of tin sulfides have been studied experimentally and identified within the Cu-Zn-Sn-S system, with signature frequencies for SnS at 160 cm^{-1}, 190 cm^{-1} and 220 cm^{-1} and for SnS_2 at 315 cm^{-1}.[9] However, it has not been a high-priority area of study by kesterite researchers as these phases can be identified by X-ray diffraction.

7.1.4 Ternary compounds

A selection of ternary phases have been identified in the literature and are considered here. A summary of the phases discussed is given in Table 7.5. The detection of ternary phases can be difficult; while changes in the A-mode frequency are effective for detecting ZnS, it may be unchanged in a Sn-rich environment containing Cu_2SnS_3.[30] In practice, researchers can be forced to assume that a Cu-poor composition acts as a safeguard against undetected ternary phases.[8]

The major peaks in the Raman spectrum of monoclinic Cu_2SnS_3 (290 cm^{-1}, 337 cm^{-1} and 352 cm^{-1}) all coincide with or lie close to peaks in kesterite.[36;37] Identification of this phase by Raman spectroscopy requires careful analysis and consideration of peak intensities; the peak at 290 cm^{-1} is distinctive but lies close to the 287 cm^{-1} peak of CZTS. Nonetheless, its absence has been used to rule out the presence of Cu_2SnS_3 in CZTS.[33]

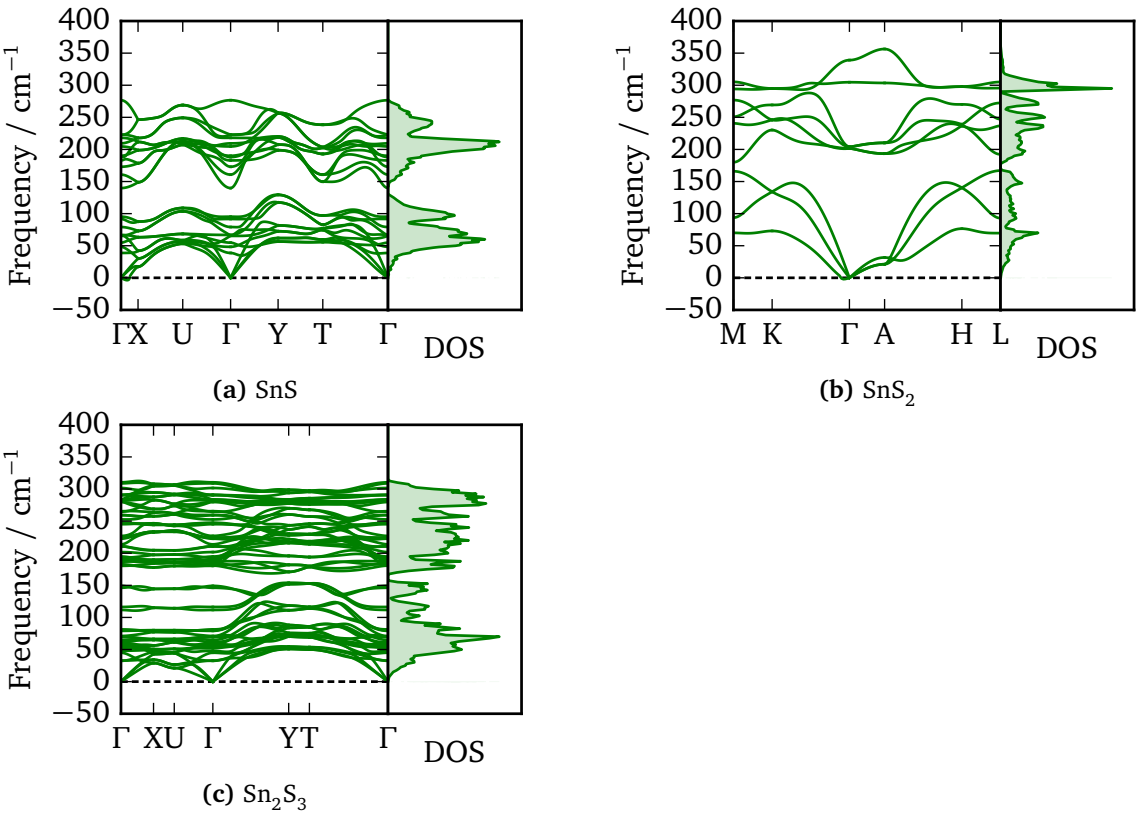

(a) SnS **(b)** SnS_2 **(c)** Sn_2S_3

Figure 7.11 – Phonon dispersion with density of states for (a) SnS (*Pnma*), (b) SnS_2 ($P\bar{3}m1$) and (c) Sn_2S_3 (*Pnma*).

Cu_2SnS_3

The most widely-discussed ternary phases have the composition Cu_2SnS_3. It is associated with a low but non-negligible conductivity, ranging between 0.03–0.5 S cm^{-1} depending on the copper content.[41] This stoichiometry emerges from the decomposition of CZTS to ZnS:

$$Cu_2ZnSnS_4 \rightarrow Cu_2SnS_3 + ZnS$$

The principle challenge in modelling Cu_2SnS_3 with first-principles calculations is the identification of suitable unit cells for periodic calculations. Zhai *et al.*[38] carried out a theoretical study, optimising the structure with the PBE XC functional before studying the optical properties with a screened hybrid functional. The two lowest-energy structures identified in that study are used in this work; the "mo-1" and "mo-2" monoclinic unit cells with *Cc* and *Imm2* symmetry, respectively. The nearest-cation-neighbour environments are similar for both cells, with a 2:1 ratio of Cu_3Sn and Cu_2Sn_2 tetrahedra surrounding S atom sites.

The 24-atom conventional unit cell was used for "mo-1", with a 9 Å **k**-point cutoff, while the "mo-2" structure was optimised as a 6-atom primitive cell with a **k**-point mesh corresponding to a 9.8 Å cutoff (Fig. 7.12).

A collection of semiconductor data describes two phases of Cu_2SnS_3: a disordered cubic phase with $a = 5.445$ Å, which may be related to the tetragonal $P\bar{4}$ structure found by Zhai *et al.*, and a monoclinic phase with $\alpha = 101°$ which does not correspond to any known phase from theoretical calculations.[32;38]

A study of experimental samples with XRD and Raman spectroscopy by Fernandes *et al.* reported tetragonal and cubic phases without assigning atomic positions within the cell.[36]

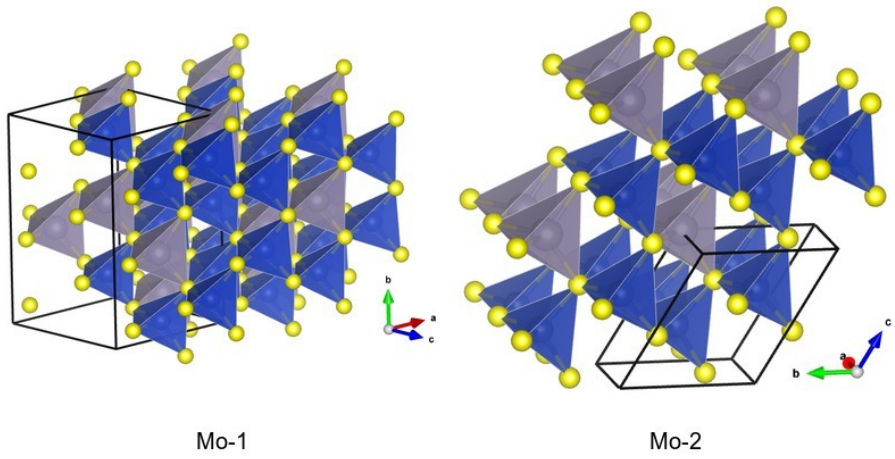

Figure 7.12 – Monoclinic structures 1 (*Cc*) and 2 (*Imm2*), derived from Ref. 38. S atoms are yellow, Cu atoms are blue, Sn atoms are grey. Cations are surrounded by tetrahedra in corresponding colours to clarify alignment.

Cu_3SnS_4

Thin films of Cu_3SnS_4 produced from an aqueous spray were reported by Bouaziz *et al.*, but were only assigned as being some tetragonal phase.[42] Fernandes *et al.* reported a $Pmn2_1$ (orthorhombic) phase of Cu_3SnS_4, obtained by sulfurising sputtered metal stacks at 520 °C.[36] Dzhagan *et al.* subsequently carried out a Raman study of colloidal nanocrystals, complemented by *ab initio* calculations with the PW91 XC functional.[39]

Based on the stoichiometry and lattice parameters one might expect Cu_3SnS_4 to adopt the same crystal structure as Cu_3AsS_4, which has the same space group and is known as "enargite". The chemistry should be different however; As presumably adopts a (+5) oxidation state, which is not known for Sn. For a balanced set of oxidation states, we would expect to either have

$$4S(-2) + Sn(+2) + 3Cu(+2) = 0 \tag{7.5}$$

or

$$4S(-2) + Sn(+4) + 2Cu(+1) + Cu(+2) = 0. \tag{7.6}$$

In the first case, the large Sn atom is in a different state from its usual role in this group of chalcogenides, while in the second case Cu is present in two oxidation states. The presence of Cu(II) in both cases suggests that *ab initio* calculations should not assume a closed shell configuration. In practice, open-shell calculations initialised using Hund's rule, for a structure optimised with the closed-shell configuration, did not lead to any change in energy, adopting the same electronic configuration. Given the uncertain electronic structure of such a compound, the **k**-point cutoff was increased to 15 Å; testing suggested that the forces were well-converged at this point.

It is difficult to reconcile the lattice parameters of Fernandes *et al.*[36] with a structure consisting of tetrahedra as generally assumed for this family of ternary compounds. Figure 7.13a shows the enargite structure; $Pmn2_1$ requires reflective symmetry along the a axis as well as a symmetry operation consisting of translation in a and c and a mirror image in the b direction. Approximating the lattice parameters of Fernandes *et al.* would require a $6 \times 1 \times 1$ supercell in the c direction to maintain a similar tetrahedral construction to enargite. However, using any even-numbered supercell in the c direction would break the $(\frac{1}{2}+x, \bar{y}, \frac{1}{2}+z)$ criterion. We therefore must assume that this structure was either misassigned, or is drastically different from the enargite-like structure which Dzhagan *et al.* were able to match to their own experiments. For this work, an original enargite-like unit cell was formed by drawing the crystal structure of enargite from the ICSD (collection code 75556), substituting the As atom for Sn

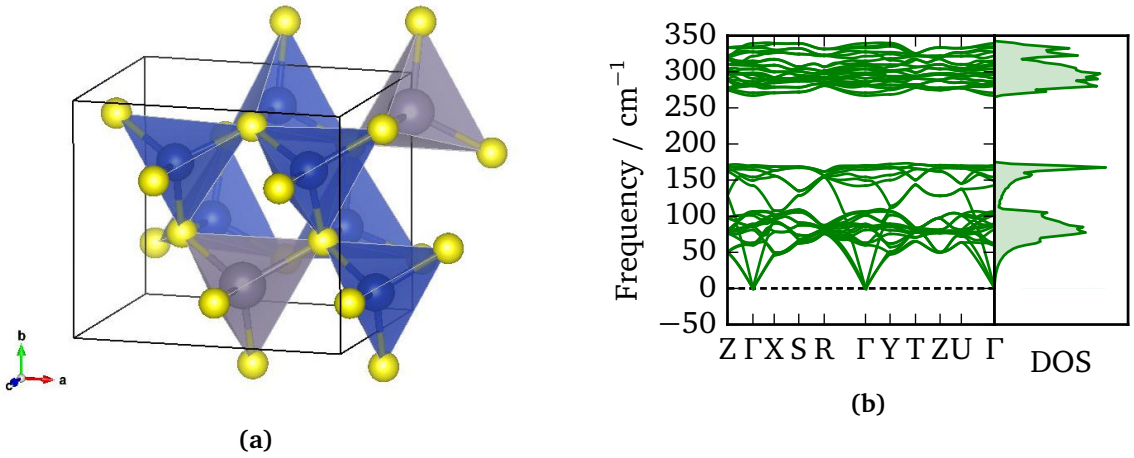

(a) **(b)**

Figure 7.13 – (a) Enargite structure, with space group *Pmn2$_1$*. S-atoms are yellow, Cu atoms are blue; grey atoms represent As in enargite, or Sn in analogous Cu_3SnS_4 phase. (b) Calculated phonon dispersion with density of states for Cu_3SnS_4 (*Pmn2$_1$*) in this structure.

and optimising the lattice vectors and atomic positions. The resulting structure appears to be in a local minimum with no soft modes in the phonon dispersion (Fig. 7.13b). The expected phonon frequencies at 295 cm^{-1}, 318 cm^{-1} and 348 cm^{-1} (or 1–2 cm^{-1} lower, depending on the reference) are among those computed at Γ; further symmetry analysis would be needed to assign them precisely.[36;39]

When calculating formation energies and predicting phase diagrams for the next Chapter, it became apparent that the ground-state energy for Cu_3SnS_4 calculated with PBEsol was abnormally low. In order to compensate for this, a set of structure optimisations was performed with the HSE06 hybrid XC functional; the calculation details are outlined on the current page. The results are given in Table 7.6, and lead to a correction of +0.667 eV FU^{-1} to the ground-state energy of *Pmn2$_1$* Cu_3SnS_4 from PBEsol. The correction is applied to this phase for all the thermodynamic modelling in this thesis.

SUMMARY OF CALCULATION PARAMETERS

Quantum chemistry code VASP

Basis set Plane waves, 500 eV cutoff

Pseudopotentials PBE-optimised pseudopotentials; 11, 12, 4, 6 electrons treated explicitly per Cu, Zn, Sn, S atom respectively

Exchange-correlation functional HSE06

k-point cutoff 25 Å (Cu); 25 Å (Zn); > 15 Å (5 × 5 × 5) (Cu_3SnS_4); 15 Å (Cu_2ZnSnS_4)

Occupation broadening Gaussian function with widths 0.05 eV (Cu, Cu_2ZnSnS_4), 0.1 eV (Zn, Cu_3SnS_4)

Structure optimisation procedure Conjugate gradient optimisation: internal positions and lattice parameters (Cu_3SnS_4, Cu_2ZnSnS_4); lattice parameters only (Cu, Zn)

Structure convergence threshold 5×10^{-3} eV Å^{-1} atom^{-1} (Cu, Zn, Cu_3SnS_4). Cu_2ZnSnS_4 optimisation stopped after 10 steps, at this point total energy convergence appears to be of order 10^{-4} eV which is deemed sufficient.

Cu_4SnS_4

An initial *Pnma* structure for Cu_4SnS_4 was drawn from the work of Anzai and Fukazawa (1986), with lattice parameters corresponding to the reported high-temperature phase, and the geometry was optimised for PBEsol.[40] In their work on $Cu_4Sn_{1-x}Ge_xS_4$ compounds they

Table 7.6 – HSE06 calculation data for Cu_3SnS_4 ($Pmn2_1$) energy correction: energy is given in eV FU^{-1}, where the Cu and Cu_2ZnSnS_4 unit cells contain one formula unit (FU) and the Zn and Cu_3SnS_4 cells contain two; lattice parameters are given with lengths in Å and angles in degrees. Note that the energies use a reference state related to the pseudopotentials employed in these calculations and are not directly compatible with other DFT-calculated energies.

Formula	space group	Energy	a	b	c	α	β	γ
Cu	$Fm\bar{3}m$	−3.648	2.570	2.570	2.570	120	90	120
Zn	$P6_3/mmc$	−1.262	2.671	2.671	4.911	90	90	120
Cu_3SnS_4	$Pmn2_1$	−39.338	7.550	6.542	6.308	90	90	90
Cu_2ZnSnS_4	$I\bar{4}$	−38.584	5.447	5.447	6.668	65.89	65.89	90

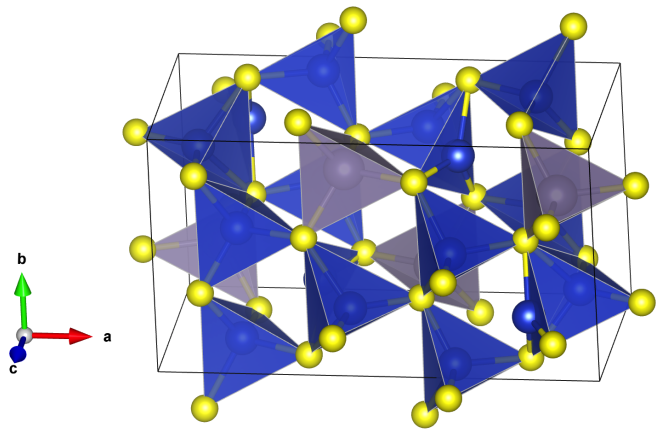

Figure 7.14 – Unit cell of *Pnma* Cu_4SnS_4 derived by Anzau and Fukazawa (1986).[40] Colour scheme as Figs. 7.12 and 7.13a. Reported as a high-temperature structure, Cu cations adopt a mixture of tetrahedral and triangular coordination environments.

explored the impact of temperature on these parameters, finding a significant transition at around 240 K. Further information about this low-temperature phase has proven difficult to find; it is associated with a decreased a parameter and decreased c parameter. An attempt to reproduce this effect *in silico* from the high-temperature structure (Fig. 7.14), by carrying out local geometry optimisation in response to constrained changes in a, did not yield any such phase transition.

The electronic band structure calculated with PBEsol suggests that the *Pnma* phase is conductive, with the valence and conduction bands overlapping about the Γ-point. However, such GGA calculations do tend to under-estimate bandgaps — higher-level calculations in other work (GGA+U with GW) computed a bandgap of 0.84 eV for this material.[41] The same work however experimentally measures an electrical conductivity of $\sim 3\,\mathrm{S\,cm^{-1}}$, placing it in between Cu_2SnS_3 and Cu_2S, and likely to lower the shunt resistance of any device in which it is present in the absorber layer.

7.2 Disorder in CZTS

7.2.1 Literature review — Raman data

Over the last few years the evidence has grown for the presence of substantial cation disorder in typical kesterite samples, as discussed in Section 3.2.2 on page 42. In 2012 Fontané *et al.* identified a Raman peak at 331 cm^{-1}, almost hidden by the main A-mode peak at 337 cm^{-1}.[7] The mode was found to vary in intensity depending on the location of the measurement, and did not match any expected secondary phases, so was assigned to disorder within the

kesterite phase. Scragg *et al.* also observed a peak around this frequency in near-resonant Raman scattering experiments with a low-frequency 785 nm laser,[43] but chose not to use it quantitatively for modelling the disorder due to its low intensity.[43] Instead, the ratio of intensities between A-modes was used as the indicator of disorder while studying the order-disorder transition with temperature, estimating a critical temperature of (533 ± 10) K.

7.2.2 Calculations

It is possible, although computationally expensive, to carry out lattice dynamics calculations using the frozen-phonon approximation for the behaviour of defects. This was demonstrated in a study of oxygen defects in GaN, using the same basic tool-chain as the majority of the work in this thesis (Phonopy, FHI-AIMS, PBEsol).[28] While the computational cost of *ab initio* calculations scales non-linearly with system size, harmonic displacement calculations tend to require similar supercell sizes and so the per-displacement cost is roughly constant (assuming that the convergence properties of systems are similar with respect to **k**-points, basis set etc.). As a result, the computational cost is proportional to the number of displacements needed, which is at most $6N$ and hence rises *linearly*.

Preliminary work was carried out to examine the effect of disorder on the vibrations of kesterite CZTS. A $2 \times 2 \times 1$ supercell of the conventional kesterite unit cell was constructed, and three different cation substitutions were made. These were single nearest-neighbour exchanges of Cu–Zn, Cu–Sn and Zn–Sn. After local optimisation, a set of finite displacements was used to calculate the vibrational properties.

SUMMARY OF CALCULATION PARAMETERS
Quantum chemistry code FHI-AIMS
Basis set Atom-centred tabulated orbitals, 'tight' set
Exchange-correlation functional PBEsol
k-point cutoff 10 Å
Occupation broadening Gaussian function with width 0.01 eV
Structure optimisation procedure Modified BFGS procedure
Structure convergence threshold 0.001 eV Å^{-1} atom^{-1}
Vibrational calculation framework Phonopy (supercell method)
Finite displacement size for vibrations 0.01 Å
Supercell dimensions 10.766 Å, 10.767 Å and 10.727 Å, angles 89.98°, 89.99° and 89.99°.

7.2.3 Analysis and results

The $2 \times 2 \times 1$ supercell contains 64 atoms, giving a set of 192 phonon modes. Due to the low symmetry of defective supercells, 384 displacements were required for the calculation of phonon modes. Plotting the Γ-point frequencies of the lattices with Cu/Zn substitutions (Fig. 7.15a), they form almost continuous bands, compared to the Γ-point frequencies computed from a primitive kesterite cell (Fig. 7.16a on page 119). Much of this can be attributed to the phenomenon of "band-folding", an artefact of increasing the calculation region to a supercell. Consider the simple 2-D square lattice illustrated in Fig. 7.16b; what appears to be a wave with the periodicity of a 2×1 supercell is equivalent to a function with the periodicity of a primitive cell, in combination with a plane wave. The effect can be mimicked for a smaller unit cell by identifying the appropriate points and combining the properties at that wave vector with those at the Γ-point (Fig. 7.16c). In this case, lattice dynamic calculations were carried out for the conventional cell of kesterite CZTS and processed without using symmetry reduction — at the Γ-point, this introduces some folded bands from the conventional expansion of the primitive cell. The vibrational frequencies at **q**-points $(\frac{1}{2}, 0, 0)$, $(0, \frac{1}{2}, 0)$, $(\frac{1}{2}, \frac{1}{2}, 0)$ were

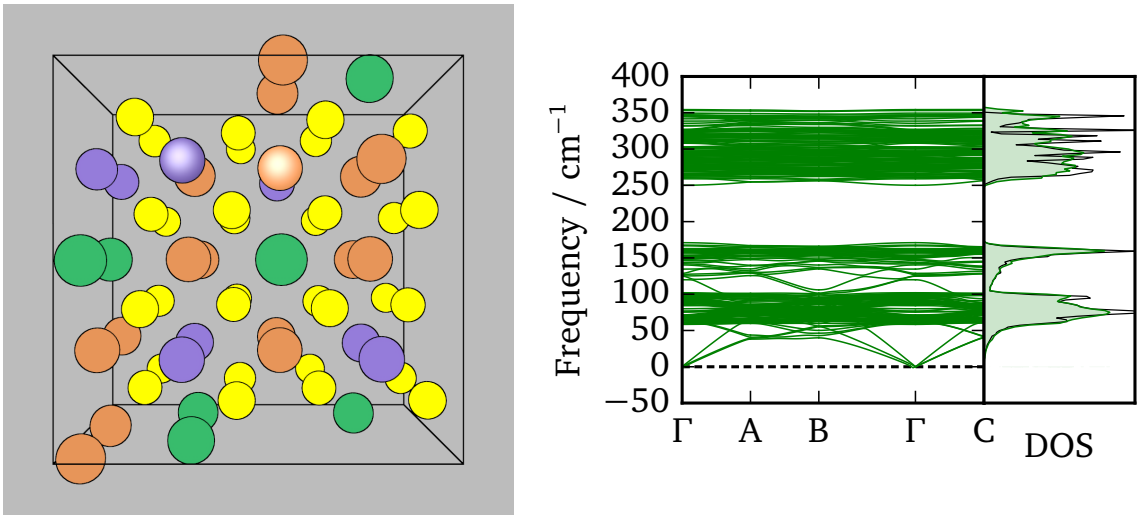

(a) Cu/Zn disordered supercell

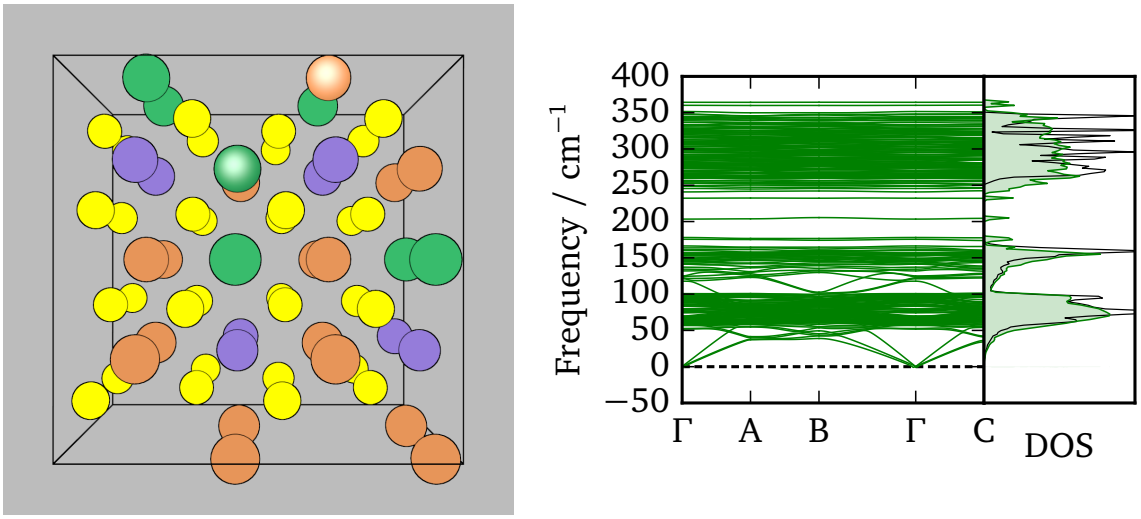

(b) Cu/Sn disordered supercell

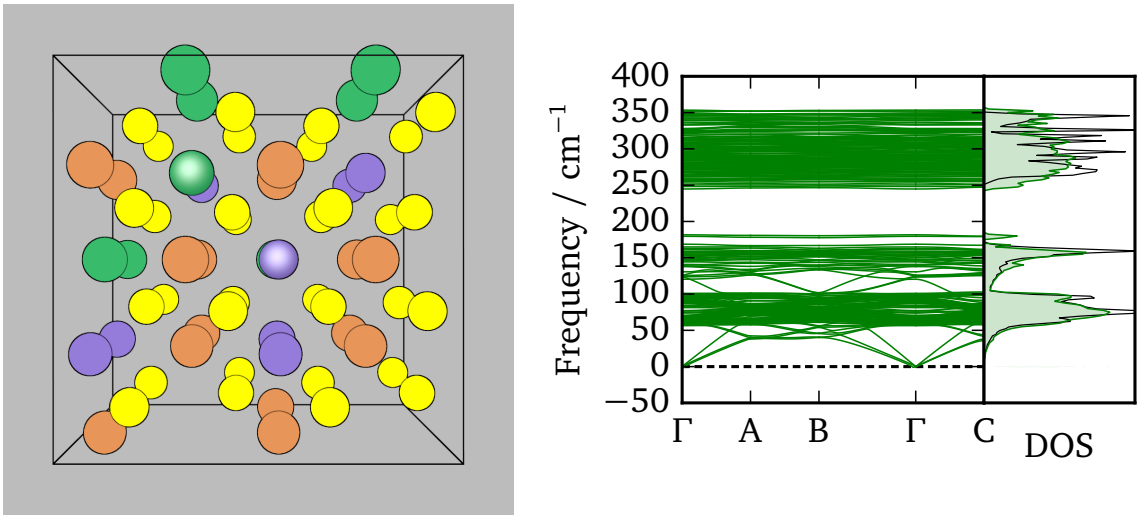

(c) Zn/Sn disordered supercell

Figure 7.15 – Disordered kesterite supercells and corresponding phonon band structures for vibrational calculations with nearest-neighbour exchanges: (a) Cu/Zn; (b) Cu/Sn; (c) Zn/Sn. Colour scheme: Cu; Zn; Sn; S. Atoms which have been exchanged are indicated with specular highlights. The density of states (DOS) of each supercell is shaded in green, while the DOS of pure kesterite is marked with a thin black line. The special points (A, B, C) marked in the phonon band structures are not standard high-symmetry points as the supercells do not formally have any symmetry, and correspond to the **q**-points with reciprocal space vectors $(\frac{1}{2}, 0, 0)$, $(\frac{1}{2}, \frac{1}{2}, 0)$ and $(0, 0, \frac{1}{2})$ respectively.

then added, to simulate the band-folding at the Γ-point of the $(2 \times 2 \times 1)$ supercell. These modes cannot be detected by Raman spectroscopy, and through a side-by-side comparison (Fig. 7.16d) the corresponding modes in the supercell spectrum can be disregarded. A significant density of vibrational states with high frequencies becomes apparent, and in the defective cells the maximum frequencies are increased. There appear to be many vibrational modes in-between the highest Γ-point frequencies of the primitive cell which are not explained by band-folding. This effect may be related to the changes in peak intensities observed in the Raman study of disordered CZTS.[43] It is a limitation of this approach that some detectable modes may be obscured because they happen to have similar frequencies to spurious ones; it would be necessary to study the effect on polarisation and polarisability of all the vibrational modes in order to determine whether some of these modes are detectable by IR or Raman spectroscopy.

It is particularly interesting to compare these results with a recent study of the selenide CZTSe by researchers at Catalonia Institute for Energy Research (IREC). A thin film was prepared with a lateral compositional gradient in order to achieve regions with different kinds of defect. Raman measurements of the different regions show changes in intensity, a little above the main peak at $196\,\mathrm{cm}^{-1}$ and in the high-frequency region, that occur as the zinc composition is moved away from perfect CZTSe. In the Zn-rich case $[2\mathrm{Zn}_{\mathrm{Cu}} + \mathrm{Zn}_{\mathrm{Sn}}]$ defect clusters are expected, while in the Zn-poor case $[\mathrm{Cu}_{\mathrm{Sn}} + \mathrm{Sn}_{\mathrm{Zn}}]$ would dominate. While caution is required when relating the frequencies of the sulfur and selenide systems, it is likely that defects and cation disorder in both systems operate in a similar way to manipulate the peak intensities and broaden the high-frequency response.

Of particular significance are heavily localised modes; these are likely to be related to the defect. Comparing the phonon band structures of the defective cells with ideal kesterite (Fig. 7.2a on page 103), it can be seen that kesterite contains comparatively few "flat" bands with little **q**-point dependence. Such bands might be identified from the phonon band structures of the supercells, but this exercise is challenging as the crossing-over of bands must be correctly identified in order to prevent jumps as the frequencies of bands are re-ordered.

7.3 Conclusions

Ground-state energies and lattice dynamics have been computed within the harmonic approximation for 17 well-defined crystal phases in the Cu-Zn-Sn-S system. Phonon band structures and formation energies have been compared to experimental data where available to ensure a high-quality consistent data set for thermodynamic modelling. Several ternary phases have been studied, but there remains some ambiguity in the structure of phases which have been reported in the literature.

Lattice dynamics have also been computed for three disordered supercells of kesterite CZTS; while some behaviour may be obscured by band-folding, these clearly display an increased density of high-frequency vibrational states. In addition, a "gap band" at around $200\,\mathrm{cm}^{-1}$ is noted in the case of nearest-neigbour Cu–Sn substitution.

Bibliography

[1] A. J. Jackson and A. Walsh, *J. Mater. Chem. A*, 2014, **2**, 7829.

[2] A. Belkly, M. Helderman, V. L. Karen and P. Ulkch, *Acta Crystallogr., Sect. B: Struct. Sci.*, 2002, **58**, 364–369.

[3] D. Fletcher, R. McMeeking and D. Parkin, *J. Chem. Inf. Model.*, 1996, **36**, 746–749.

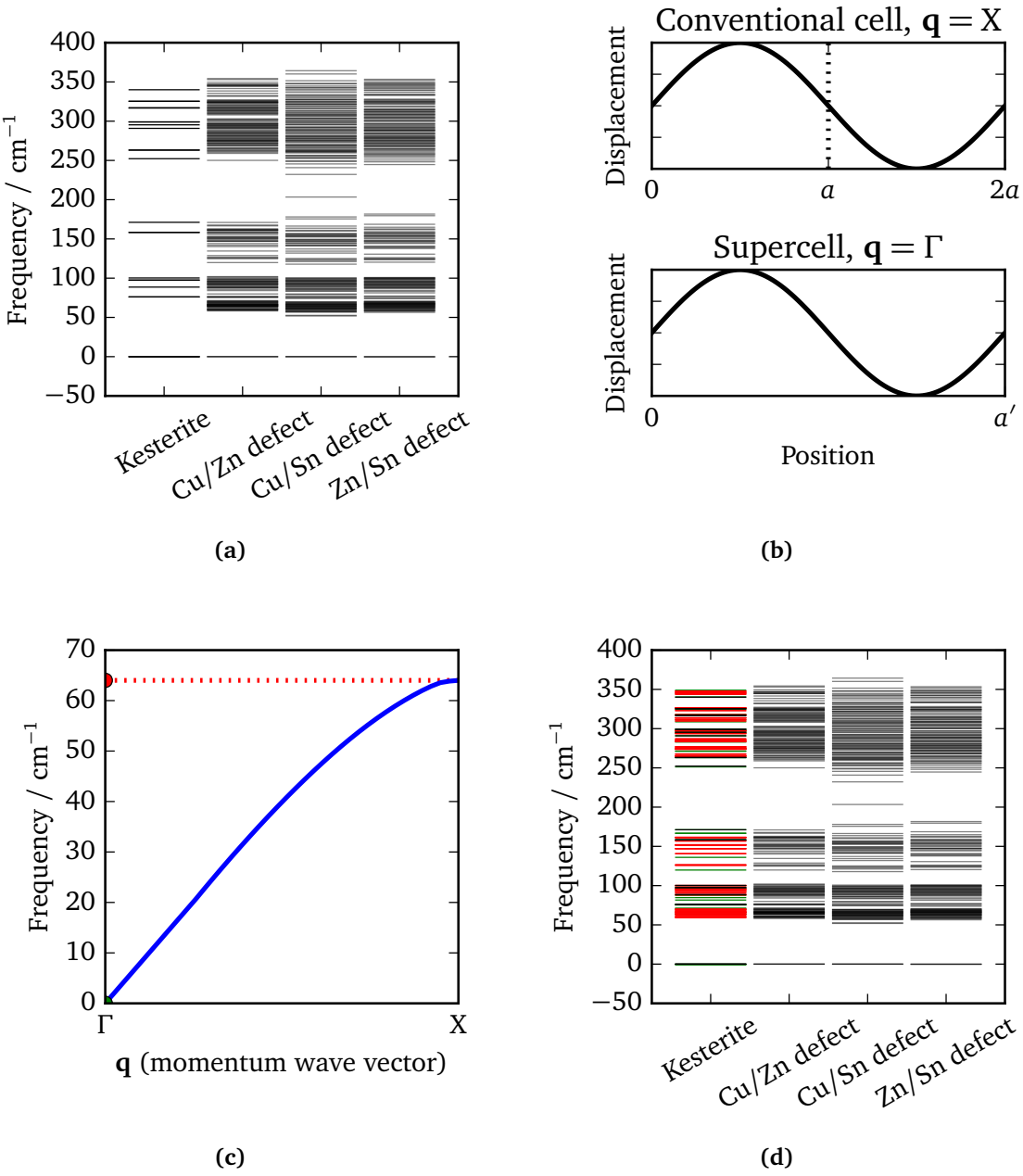

Figure 7.16 – Effect of band-folding on Γ-point vibrational frequencies of supercell. (a) the Γ-point frequencies of the primitive kesterite cell are plotted against the defect supercells. Note that the defective supercells have a large number of dispersed frequency values. (b) Illustration of two identical displacement waves expressed in different unit cells; in a conventional cell with lattice parameter a this displacement has the off-Γ wave vector X (a **q**-point with magnitude 1/2). In a supercell with lattice vector $a' = 2a$, the same displacement behaviour is contained within a single unit cell and therefore is a Γ-point mode. This is potentially misleading, as it has the same physical symmetry properties in both cases and can be assumed to be Raman-inactive without further investigation. (c) The "folded" frequencies associated with a supercell can be calculated by examining the appropriate **q**-points. In this example a harmonic mode of kesterite with zero frequency at the Γ-point is duplicated and appears to have a frequency of 64 cm^{-1}. (d) In order to compensate for this, the frequencies of the conventional cell at the Γ-point (green) and **q**-points $(0.5, 0, 0)$, $(0.5, 0.5, 0)$ and $(0.5, 0.5, 0)$ (red) are overlaid with the actual primitive cell frequencies (black). The defective supercells all show an increased density of dispersed Γ-point states at high frequencies, which is not explained by band-folding.

[4] S. Chen, X. G. Gong, A. Walsh and S.-H. Wei, *Appl. Phys. Lett.*, 2010, **96**, 021902.

[5] A. Togo, *Spglib*, `http://spglib.sourceforge.net/index.html`, [Accessed: 2015-08-25].

[6] A. Khare, B. Himmetoglu, M. Johnson, D. J. Norris, M. Cococcioni and E. S. Aydil, *J. Appl. Phys.*, 2012, **111**, 083707.

[7] X. Fontané, V. Izquierdo-Roca, E. Saucedo, S. Schorr, V. Yukhymchuk, M. Valakh, A. Pérez-Rodríguez and J. Morante, *J. Alloys Compd.*, 2012, **539**, 190–194.

[8] M. Dimitrievska, H. Xie, A. Fairbrother, X. Fontané, G. Gurieva, E. Saucedo, A. Pérez-Rodríguez, S. Schorr and V. Izquierdo-Roca, *Appl. Phys. Lett.*, 2014, **105**, 031913.

[9] P. A. Fernandes, P. M. P. Salomé and A. F. da Cunha, *Thin Solid Films*, 2009, **517**, 2519–2523.

[10] J. M. Skelton, A. J. Jackson, M. Dimitrievska, S. K. Wallace and A. Walsh, *APL Mater.*, 2015, **3**, 041102.

[11] A. Dal Corso, *J. Phys.: Condens. Matter*, 2013, **25**, 145401.

[12] N. Gaston and B. Paulus, *Phys. Rev. B.*, 2007, **76**, 214116.

[13] L. Almqvist and R. Stedman, *J. Phys. F: Met. Phys.*, 1971, **1**, 312.

[14] W. M. Haynes and D. R. Lide, *CRC Handbook of Chemistry and Physics*, Taylor & Francis, 2011.

[15] J. J. Scragg, *Copper Zinc Tin Sulfide Thin Films for Photovoltaics*, Springer-Verlag, Berlin, Heidelberg, 2011.

[16] J. Ihm and M. L. Cohen, *Phys. Rev. B*, 1981, **23**, 1576–1579.

[17] P. Pavone, S. Baroni and S. de Gironcoli, *Phys. Rev. B*, 1998, **57**, 10421–10423.

[18] A. Jain, S. P. Ong, G. Hautier, W. Chen, W. D. Richards, S. Dacek, S. Cholia, D. Gunter, D. Skinner, G. Ceder and K. A. Persson, *APL Mater.*, 2013, **1**, 011002.

[19] J. Saal, S. Kirklin, M. Aykol, B. Meredig and C. Wolverton, *JOM*, 2013, **65**, 1501–1509.

[20] D. Price and J. Rowe, *Solid State Commun.*, 1969, **7**, 1433–1438.

[21] T. Wolfram, G. W. Lehman and R. E. De Wames, *Phys. Rev.*, 1963, **129**, 2483–2489.

[22] J. M. Rowe, *Phys. Rev.*, 1967, **163**, 547–551.

[23] R. Steudel and B. Eckert, *Top. Curr. Chem.*, 2003, 1–79.

[24] L. A. Burton and A. Walsh, *J. Phys. Chem. C*, 2012, **116**, 24262–24267.

[25] M. J. Chase, *J. Phys. Chem. Ref. Data, Monogr.*, 1998, **9**, 1–1951.

[26] P. J. Gardner and P. Pang, *J. Chem. Soc., Faraday Trans. 1*, 1988, **84**, 1879–1887.

[27] K. Reuter and M. Scheffler, *Phys. Rev. Lett.*, 2003, **90**, 046103.

[28] A. J. Jackson and A. Walsh, *Phys. Rev. B*, 2013, **88**, 165201.

[29] B. J. Morgan and G. W. Watson, *J. Phys. Chem. C*, 2010, **114**, 2321–2328.

[30] D. M. Berg and P. J. Dale, in *Copper zinc tin sulphide-based thin film solar cells*, ed. K. Ito, John Wiley & Sons, Chichester, UK, 2015, ch. 5, pp. 107–132.

[31] Q. Xu, B. Huang, Y. Zhao, Y. Yan, R. Noufi and S.-H. Wei, *Appl. Phys. Lett.*, 2012, **100**, 061906.

[32] O. Madelung, *Semiconductors: Data Handbook*, Springer-Verlag, Berlin, 3rd edn., 2004.

[33] X. Fontané, L. Calvo-Barrio, V. Izquierdo-Roca, E. Saucedo, A. Pérez-Rodriguez, J. R. Morante, D. M. Berg, P. J. Dale and S. Siebentritt, *Appl. Phys. Lett.*, 2011, **98**, 181905.

[34] A. Fairbrother, X. Fontané, V. Izquierdo-Roca, M. Espíndola-Rodríguez, S. López-Marino, M. Placidi, L. Calvo-Barrio, A. Pérez-Rodríguez and E. Saucedo, *Sol. Energy Mater. Sol. Cells*, 2013, **112**, 97–105.

[35] S. López-Marino, Y. Sánchez, M. Placidi, A. Fairbrother, M. Espindola-Rodríguez, X. Fontané, V. Izquierdo-Roca, J. López-García, L. Calvo-Barrio, A. Pérez-Rodríguez and E. Saucedo, *Chem. - Eur. J.*, 2013, **19**, 14814–14822.

[36] P. A. Fernandes, P. M. P. Salomé and A. F. da Cunha, *J. Phys. D: Appl. Phys.*, 2010, **43**, 215403.

[37] D. M. Berg, R. Djemour, L. Gütay, S. Siebentritt, P. J. Dale, X. Fontane, V. Izquierdo-Roca and A. Pérez-Rodriguez, *Appl. Phys. Lett.*, 2012, **100**, 192103.

[38] Y.-T. Zhai, S. Chen, J.-H. Yang, H.-J. Xiang, X.-G. Gong, A. Walsh, J. Kang and S.-H. Wei, *Phys. Rev. B*, 2011, **84**, 075213.

[39] V. M. Dzhagan, A. P. Litvinchuk, M. Kruszynska, J. Kolny-Olesiak, M. Y. Valakh and D. R. T. Zahn, *J. Phys. Chem. C*, 2014, **118**, 27554–27558.

[40] S. Anzai and T. Fukazawa, *J. Phys. Soc. Jpn.*, 1986, **55**, 701–702.

[41] P. Zawadzki, L. L. Baranowski, H. Peng, E. S. Toberer, D. S. Ginley, W. Tumas, A. Zakutayev and S. Lany, *Appl. Phys. Lett.*, 2013, **103**, 1–6.

[42] M. Bouaziz, J. Ouerfelli, M. Amlouk and S. Belgacem, *Phys. Status Solidi A*, 2007, **204**, 3354–3360.

[43] J. J. S. Scragg, L. Choubrac, A. Lafond, T. Ericson and C. Platzer-Björkman, *Appl. Phys. Lett.*, 2014, **104**, 041911.

Chapter 8

Equilibrium in the Cu-Zn-Sn-S system

8.1 Formation and decomposition reactions

This section includes work which was published as a full paper in 2014.[1] *Since the publication of that paper, some of the calculations have been revisited with a view to improving convergence. Several additional phases were also introduced to the modelling framework, most notably the ternary phases and the new chemical potential for mixed sulfur vapours.*

8.1.1 Formation reactions

The phase stability of CZTS can be examined with respect to specific decomposition products by computing the Gibbs free energy associated with the relevant reactions. The Gibbs free energy is plotted here for the *formation* of kesterite CZTS from a range of precursors, as a function of both pressure and temperature. Negative formation energies therefore correspond to a region in which CZTS is stable with respect to the precursors, while positive energies are associated with instability.

Two simple cases to consider are typical formation pathways for CZTS: annealing in an inert atmosphere from a set of metal sulfides, and annealing with sulfur gas from a combination of metals. Figures 8.1 and 8.2 show that no significant reverse reaction is obtainable through the selection of an inappropriate annealing temperature. This reflects experimental success in forming CZTS using these precursors; it does not rule out the formation of other phases or give us any information about kinetics. The order of magnitude difference in formation energies reflects the relative stability of the binary phases to their constituent elements. In particular, the "solid-state" formation of CZTS from the binaries typically takes place at molten conditions and proceeds slowly, with annealing times in the order of one week required for high-quality samples. Molten phases and non-harmonic behaviour were not included in this model. Bearing in mind that SnS is reported to melt at 1153 K, results above around 1000 K should be treated with caution.[2]

8.1.2 Decomposition to SnS

Decomposition pathways of CZTS to SnS have been of considerable interest. Weber *et al.* analysed the varying composition of CZTS samples annealed under high vacuum (10^{-2} Pa), observing significant Sn loss at temperatures above 500 °C and some SnS loss at lower temper-

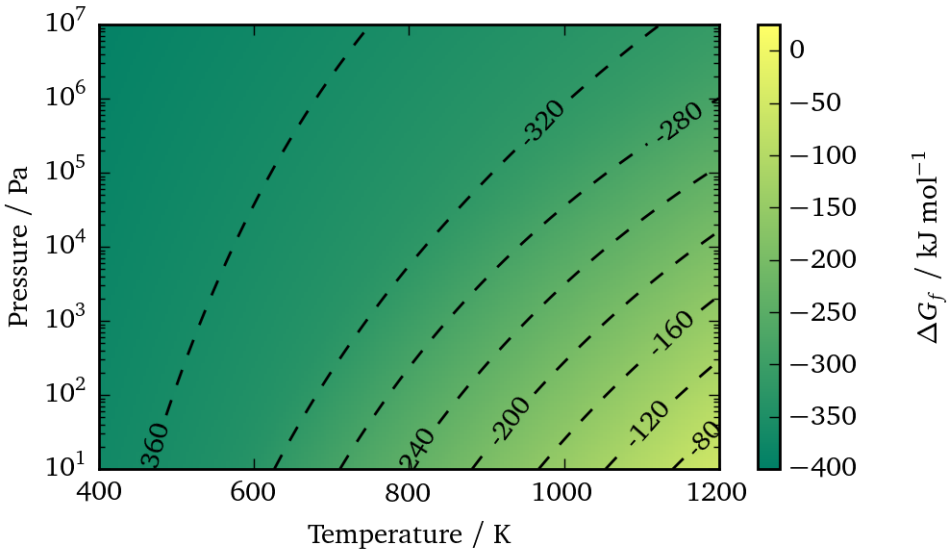

$$2\mathrm{Cu} + \mathrm{Zn} + \mathrm{Sn} + 4\mathrm{S} \leftrightharpoons \mathrm{Cu_2ZnSnS_4}$$

Figure 8.1 – Formation of $I\bar{4}2$ (kesterite) CZTS from elemental precursors including mixed sulfur vapours. Gibbs free energy plotted as function of temperature and pressure; kesterite is stable wherever the temperature is below 1200 K and/or the pressure is greater than 1 Pa.

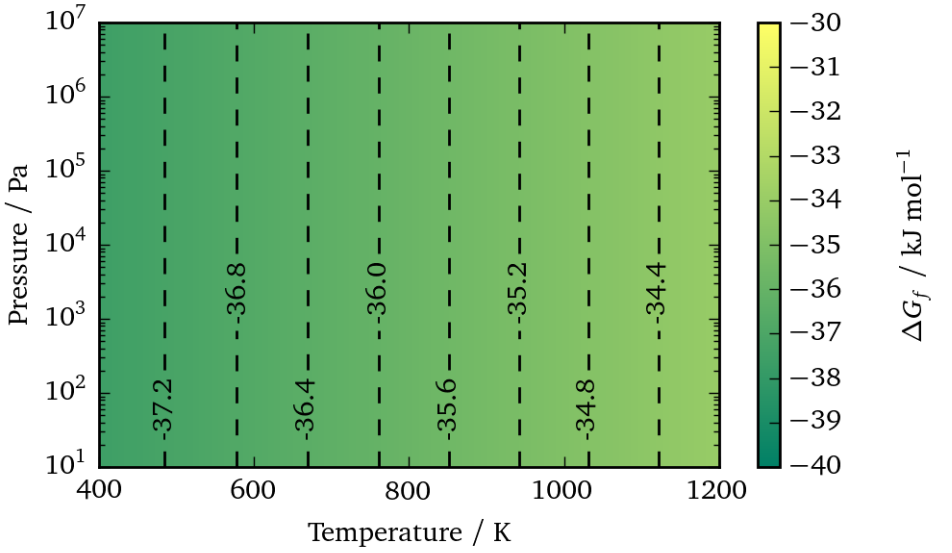

$$\mathrm{Cu_2S} + \mathrm{ZnS} + \mathrm{SnS_2} \leftrightharpoons \mathrm{Cu_2ZnSnS_4}$$

Figure 8.2 – Formation of $I\bar{4}2$ (kesterite) CZTS from $P2_1/c$ Cu_2S, $F\bar{4}3m$ (zincblende) ZnS and $P\bar{3}m1$ SnS_2. Gibbs free energy plotted as function of temperature and pressure; kesterite is stable over all conditions examined.

atures.[3] Three decomposition reactions were suggested which might yield SnS:

$$2Cu_2SnS_{3(s)} \rightarrow Cu_4SnS_{4(s)} + SnS_{(g)} + S_{(g)}; \tag{8.1}$$

$$Cu_4SnS_{4(s)} \rightarrow 2Cu_2S_{(s)} + SnS_{(g)} + S_{(g)}; \tag{8.2}$$

and

$$Cu_2ZnSnS_{4(s)} \rightarrow Cu_2S_{(s)} + ZnS_{(g)} + SnS_{(g)} + S_{(g)}. \tag{8.3}$$

This was followed up by Scragg *et al.*, proposing that Reaction 8.3 be considered a two-step process in which solid SnS is formed and subsequently evaporates to SnS vapour[4]

$$Cu_2ZnSnS_{4(s)} \leftrightharpoons Cu_2S_{(s)} + ZnS_{(s)} + SnS_{(s)} + \frac{1}{2}S_{2(g)} \tag{8.4}$$

and

$$SnS_{(s)} \leftrightharpoons SnS_{(g)}. \tag{8.5}$$

The nature of the solid SnS is not specified, and it may be closer to an adsorbed monolayer than a true crystal, but the key point is that the removal of SnS vapours by a vacuum pump indirectly drives the decomposition, making what may be a finely balanced equilibrium in the solid-state act as a major source of Sn loss. Another experiment exploring this equilibrium formed CZTS by annealing a Cu/Zn stack with sulfur and SnS_2, demonstrating that the system decomposed when annealed further in a vacuum.[5] Scragg *et al.* carried out a series of experiments at low pressure with carefully controlled doses of sulfur, forming a model of the phase stability with an estimated transition region.[4] Using the data from *ab initio* lattice dynamics, the formation reaction corresponding to Eq. (8.4) is modelled in Fig. 8.3, and the estimated transition region from their study is overlaid. The agreement is strong, showing that the methodology in this work is capable of making qualitative predictions and has some ability to make quantitative predictions. The key finding here is that the system is extremely sensitive to pressure at typical annealing temperatures. Many high-quality CZTS samples are produced under high vacuum, but the exact pressure of the vacuum is not always reported. These findings were reported in *J. Mater. Chem. A*, concluding with the following words:[1]

> One issue with rigorous validation of the model is the scarcity of experimental thermodynamic data so far. We suggest that high-temperature near-vacuum experiments need to control and report the annealing pressure carefully if they are to be reproducible and aid understanding of the phase equilibria of multi-component semiconductors such as Cu_2ZnSnS_4.

8.2 Introduction to phase diagrams

> *The author is indebted to Anubhav Jain's comic strip "Materials stability and Nature's bike shop", which builds up the concept of multi-dimensional and open phase diagrams via the convex hull construction in a charming and effective way.*[6] *If the reader is unfamiliar with such diagrams this is a strongly recommended introduction. While the introduction to phase diagrams given here is original and focuses on relevant systems, a broadly similar structure is followed. Other useful references for the understanding of more complex diagrams and alternative constructions are given as Refs. 7;8.*

While it can be informative to study individual equilibrium reactions, phase diagrams are a powerful set of tools for the study of multi-phase equilibria.

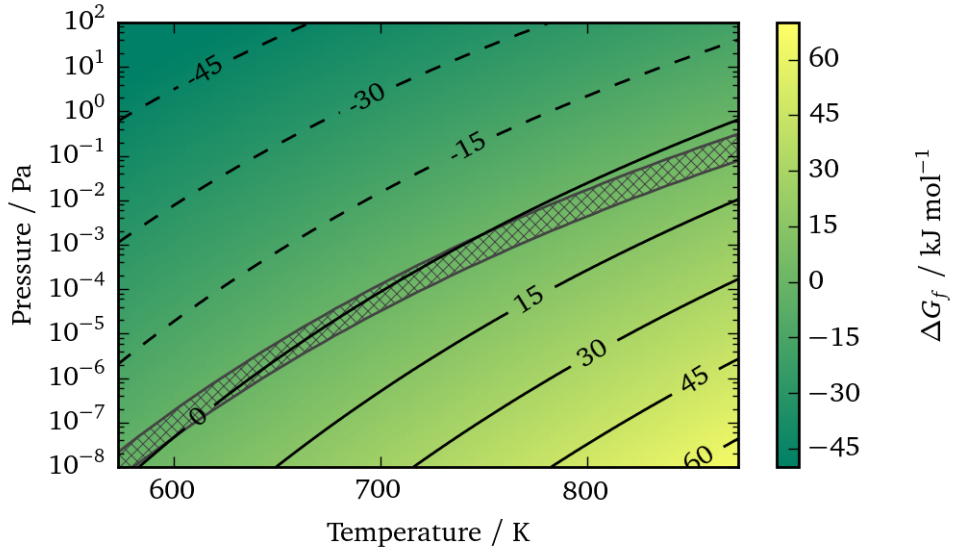

$$Cu_2S + ZnS + SnS + \frac{1}{2}S_2 \leftrightharpoons Cu_2ZnSnS_4$$

Figure 8.3 – Formation of $I\bar{4}2$ (kesterite) CZTS from $P2_1/c$ Cu_2S, $F\bar{4}3m$ (zincblende) ZnS, *Pnma* SnS and S_2 gas. Gibbs free energy plotted as function of temperature and pressure; shaded region is estimated stability line from experimental work and kinetic modelling.[4]

8.2.1 Phase diagram types considered

Two key questions we aim to answer with respect to the Cu-Zn-Sn-S system are

1. Is kesterite CZTS stable?
2. Which side-products can co-exist with CZTS?

In the more general case, this is really one question:

- For a given system and conditions, which phases are present at equilibrium?

Given the nature of reaction equilibria, any phase *can* be present, so we tend to focus on the phases that are *dominant*. Dominance is inherently related to the reaction equilibrium constant K, and hence the Gibbs free energy. For the simple transformation $A \rightleftharpoons B$,

$$\frac{n_A}{n_B} = K = \exp\left(-\frac{\Delta G}{RT}\right) = \exp\left(-\frac{\mu_A - \mu_B}{RT}\right). \tag{8.6}$$

While the picture is complicated by the inclusion of multiple products and stoichiometric terms, it remains the case that the dominance of reaction products increases exponentially with the absolute value of the change in Gibbs free energy. It is therefore convenient to map the phase or combination of phases which minimise the Gibbs free energy at a given set of conditions.

Convex hull

A convex hull plot sets a binary composition against free energy. Figure 8.4 is one such plot, from data produced in a previous study of SnS_x compounds.[9] In this case, ground-state energies from DFT calculations were used as a first-order approximation of the free energy; the phase diagrams presented later in this section will go further by considering thermal

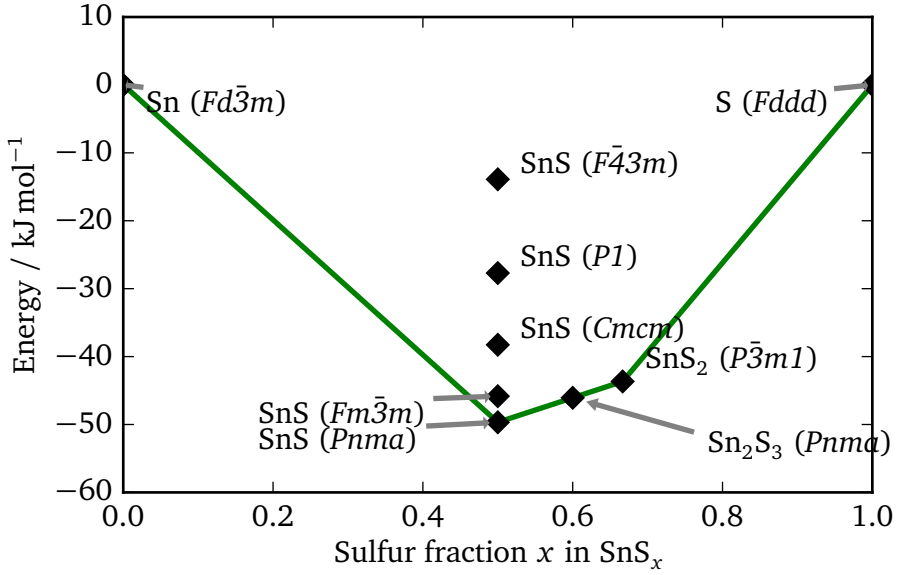

Figure 8.4 – Sn-S convex hull from DFT calculations.[9] Redrawn from original data, following conventional convex hull principles. DFT energies are given as a formation energy per mole of atoms, where the energies of standard states are set to zero.

contributions. The formation energy of any individual phase from standard states is indicated by a large marker, but other spaces on the diagram are also possible to achieve as a mixture of other phases. Points lying on the straight lines represent a linear combination of phases which minimises the free energy at that composition. In Fig. 8.4, two phases are of particular interest. The first is the SnS ($F\bar{4}3m$) phase, which is substantially higher in energy than the other phases with the same composition. This strongly suggests that such a phase would only exist in negligible quantities at equilibrium. Also of interest is the Sn_2S_3 phase, which lies slightly above the tie-line between SnS and SnS_2. In this model, the phase is higher in energy than the linear combination $SnS + SnS_2$ and hence would not be dominant even at the correct 2:3 stoichiometry. However, it lies very close to the line, and so in practice K would be of the order 1 for the reaction $SnS_2 \rightleftharpoons SnS + S$ and the phase is expected to be present in measurable quantities. Given that DFT errors for formation energies are typically in the region of 10 kJ mol^{-1}, the instability of this phase is highly uncertain.[10]

Ternary phase diagrams

The ternary phase diagram Cu-Sn-S (Fig. 8.5) is considered next, using data from this study. The stoichiometry of a ternary system is expressed in two-dimensional space by rejecting two pieces of information:

1. The atom fractions of element A and element B are plotted, requiring that $\frac{n_A}{n_t} + \frac{n_B}{n_t} + \frac{n_C}{n_t} = \frac{n_t}{n_t} = 1$; as a result the total number of atoms in a formula unit n_t is lost from the plot. This is unimportant information and in any case can be recovered by inspection of the point labels.

2. The actual relative formation energies are no longer displayed; instead only points that lie along a convex hull are shown. In general this is the only information of interest, but in special cases such as Sn_2S_3 in the dataset of Fig. 8.4 this may be a misleading picture — there is not a conventional way of showing phases that are "close" in energy.

Ternary phase diagrams are conventionally plotted on triangular axes; this is not strictly required and orthogonal axes may be used. However, they are very convenient to interpret as each set of binary compounds lies along one side.

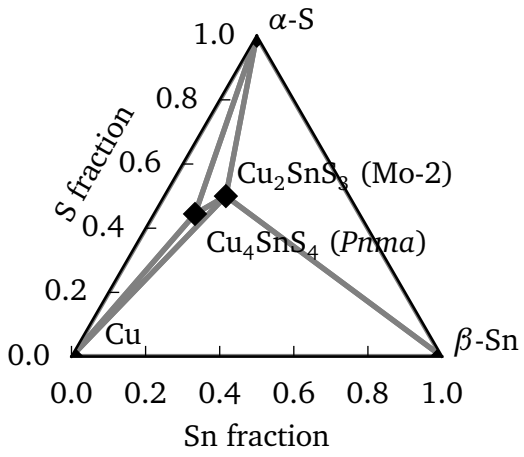

Figure 8.5 – Cu-Sn-S ternary phase diagram; data from this work, based on chemical potentials at standard conditions.

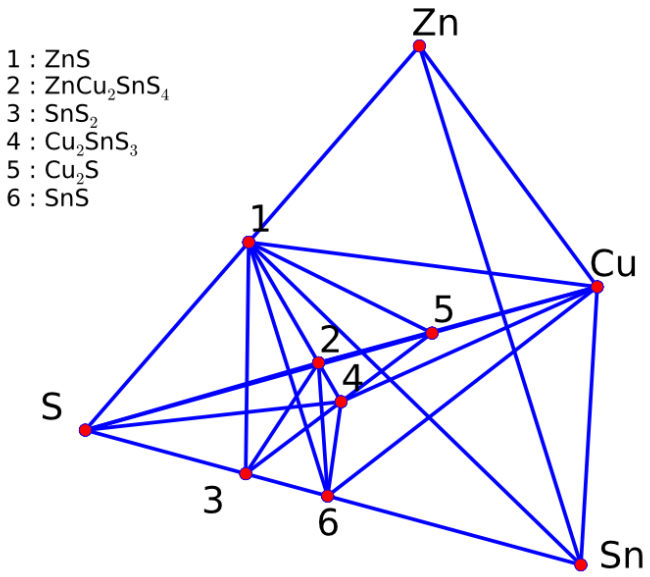

Figure 8.6 – Quaternary Cu-Zn-Sn-S phase diagram at standard conditions from data in this work. Each corner of the tetrahedron represents 100% atomic composition of the corresponding element. Plotted with Python Materials Genomics library. Not all ternary phases are included.

Going beyond three components: grand canonical phase diagrams

Presenting quaternary systems is more problematic. It is possible to extend the ternary phase diagram model, providing another axis for composition. This leads to a three-dimensional object such as Fig. 8.6 which is difficult to interpret when projected onto two-dimensional space.

One solution is to plot a "slice" through the tetrahedron, with axes following certain stoichiometry ratios rather than pure compounds. An example is reproduced from the literature in Fig. 8.7; the experimental quasi-ternary phase diagram of the Cu_2S–ZnS–SnS_2 system. In the case of Cu_2ZnSnS_4this makes for a particularly attractive plot as the kesterite phase sits at the center of a diagram containing known side-products. For a closed system with known reaction pathways this is quite a satisfactory solution. However, there is an obvious deficiency of this diagram with respect to the Cu-Zn-Sn-S system; SnS_2 is presented as an accessible phase, while SnS is nowhere to be seen. In practice, there is every reason to believe that SnS plays an important role in the thermodynamics of the system, as demonstrated in Section 8.1.2.

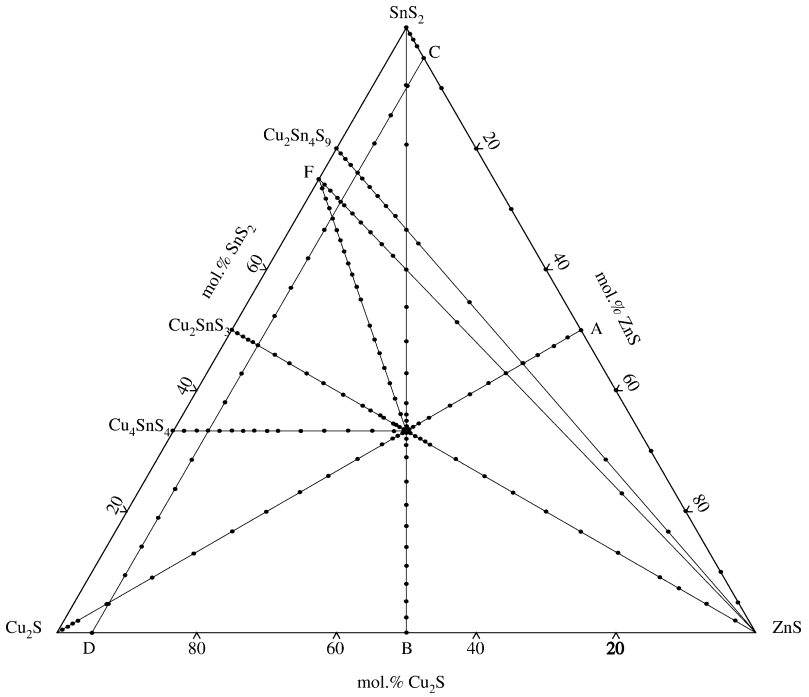

Figure 8.7 – Quaternary phase diagram for CZTS and a subset of competing phases, expressed as Cu_2S–ZnS–SnS_2 quasi-ternary system. Figure reproduced from experimental work by Olekseyuk *et al.*; each black circle represents an experimental sample.[11]

The key point is that the stoichiometry with respect to sulfur is not truly fixed, as sulfur is readily lost to the vapour phase. In a low-pressure system, sulfur vapours are liable to be extracted by the vacuum pump. The vapour phase may be seen as a source or sink of sulfur atoms; the thermodynamic cost of a sulfur atom is its chemical potential

$$\mu_S = \left(\frac{\partial G}{\partial n}\right)_{T,p_S} = f(T, p_S). \tag{8.7}$$

Given that sulfur is usually provided in excess, it is approximated as an infinite source/sink such that adding and removing sulfur from the system does not change the chemical potential μ_S. By allowing the sulfur content of the system to vary, a degree of freedom is introduced to the plot. Such a figure is known as a "grand canonical phase diagram", after the thermodynamic ensemble with similar characteristics. The elemental composition is used as the coordinate system, but additional "open" species are included with variable composition. The dominant phases, shown on the plot, are determined by the fixed chemical potentials of those open phases.

8.2.2 Implementation

Initial prototyping was carried out using the Python Materials Genomics (PYMATGEN) library.[12] In order to overcome some limitations as well as understand the methodology, a new phase diagram solver and plotter was implemented in Python, using the following procedure.

1. Compute the free energy of each phase under consideration, as used in Section 8.1.

2. Convert these to formation energies ΔG relative to their component elements, based on known stoichiometry. This is not strictly required, but reduces the stress on the convex hull solver and reduces the risk of numerical errors.

3. Construct a $3 \times m$ matrix of the format

$$\begin{pmatrix} \frac{n_{1,1}}{n_{1,1}+n_{1,2}+n_{1,3}} & \frac{n_{1,2}}{n_{1,1}+n_{1,2}+n_{1,3}} & \frac{\Delta G_{f,1}}{n_{1,1}+n_{1,2}+n_{1,3}} \\ \frac{n_{2,1}}{n_{2,1}+n_{2,2}+n_{2,3}} & \frac{n_{2,2}}{n_{2,1}+n_{2,2}+n_{2,3}} & \frac{\Delta G_{f,2}}{n_{1,2}+n_{2,2}+n_{2,3}} \\ \vdots & \vdots & \vdots \end{pmatrix}$$

where $n_{i,j}$ is the number of atoms of element j in a single formula unit of i; $j \in \{1,2,3\}$, indices which identify the elements used as plotting axes. The first two colums uniquely define the position of a point on the phase diagram, while the third column provides the corresponding scaled energies. The phases i in this matrix are all of the phases which are *not* open; there must be an unambiguous location for them on the phase diagram. Note that the open elements are also not included in the energy scaling terms.

4. Solve the convex hull of points identified by rows of the matrix. An external library is used for this (QHULL, via a SCIPY interface), implementing the "quickhull" algorithm.[13–15]

5. Remove all points and simplices (i.e. coexistence lines) which lie above a linear combination of the low-energy elemental phases. This step is necessary as the general convex hull solution can include high-energy phases as long as the angles between points are convex.

6. Plot and label the points and simplices on triangular axes. (Plotting used the MATPLOTLIB library with an additional ternary projection developed by Richard Otis.)[16;17]

8.3 Results

The grand canonical phase diagram for the model system at 298 K and under a 10^5 Pa sulfur atmosphere is shown as Fig. 8.8. At standard conditions, SnS_2 is the dominant sulfur phase under a sulfur-rich atmosphere and so this figure closely resembles Fig. 8.7, except that Cu_4SnS_4 is not represented. The other ternary and alloy phases in that diagram were not included in this study.

As the system is brought to annealing-like conditions of 850 K and 10^3 Pa (10 mbar), SnS_2 is reduced to SnS (Fig. 8.9). It is worth noting the simplicity of this observation; in Ref. 18 the authors discuss the formation of SnS in response to vacancies formed by volatile sulfur. In the language of chemical intuition it is argued that the sulfur loss, driven by a vacuum pump, is an oxidation process and that it is easier to form Sn(II) from Sn(IV) than to further oxidise the other metals in response to defect formation. In the phase diagram approach, one simply notes that $\mu_{SnS} + \mu_S < \mu_{SnS_2}$ and disregards tin (IV) sulfide as a viable phase, without considering the underlying causes of the process. The vacuum pump is abstracted away, contributing to the low chemical potential of sulfur.

The volatility of SnS gas is not directly considered in this model, but can be taken into account. The vapour pressure of SnS is a function of temperature and has been fitted to experimental data; for example, at 850 K $p_{SnS} \approx 40$ Pa.[19] The total pressure of the system $P \approx p_S + p_{SnS}$.

In Fig. 8.11, phase diagrams are constructed for a number of T, p combinations. The upper-left conditions correspond to typical "vacuum annealing" conditions, while the lower right conditions correspond to "solid-state" synthesis conditions. The phase diagram is unchanged except for the SnS/SnS_2 phase as discussed. At very high values of μ_S (low p, high T), the corner chalcogenides are reduced to metals, and this is observed for Cu. This temperature region exceeds the recommended region for the harmonic approximation, so the transition temperatures are likely to be unreliable, but it is reassuring that the basic physical phenomenon of smelting is reproduced correctly.

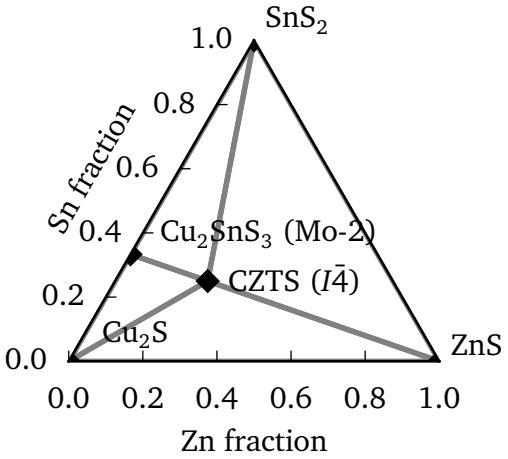

Figure 8.8 – Grand canonical phase diagram of Cu-Zn-Sn-S system at standard conditions (298 K and 10^5 Pa). The system is "open" to sulfur, with a chemical potential corresponding to a sulfur atmosphere at this temperature and pressure.

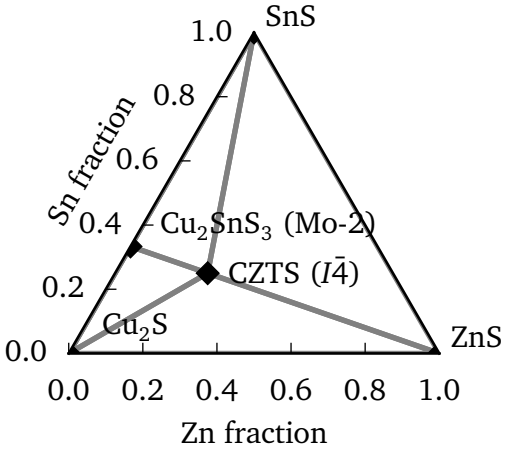

Figure 8.9 – Grand canonical phase diagram of Cu-Zn-Sn-S system at annealing-like conditions (850 K and 10^3 Pa). The system is "open" to sulfur, with a chemical potential corresponding to a sulfur atmosphere at this temperature and pressure.

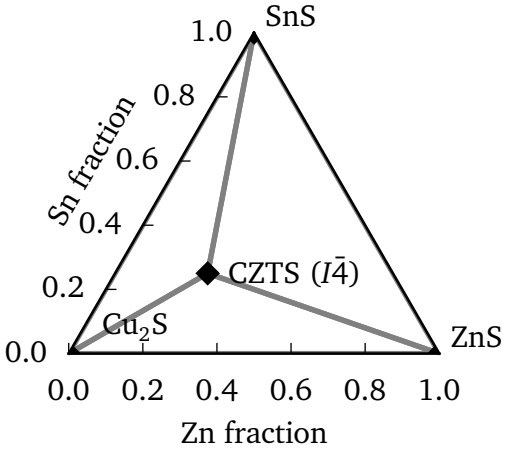

Figure 8.10 – Grand canonical phase diagram of Cu-Zn-Sn-S system at "sweet spot" conditions of 1050 K and 10^2 Pa. The system is "open" to sulfur, with a chemical potential corresponding to a sulfur atmosphere at this temperature and pressure.

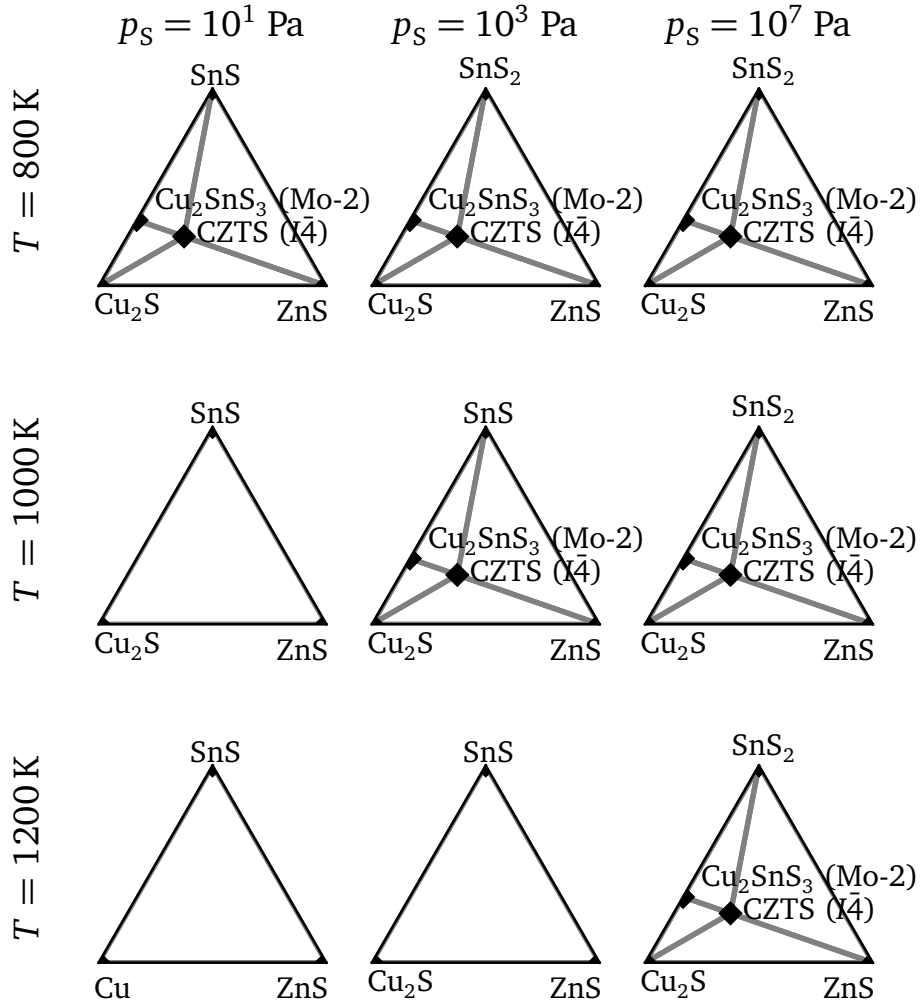

Figure 8.11 – Array of grand canonical phase diagrams corresponding to a range of annealing conditions. For clarity, the axis labels and ticks have been omitted; the plot construction is otherwise identical to that in Figs. 8.8 to 8.10. It should be noted that 1200 K is above the melting point of SnS (1153 K).

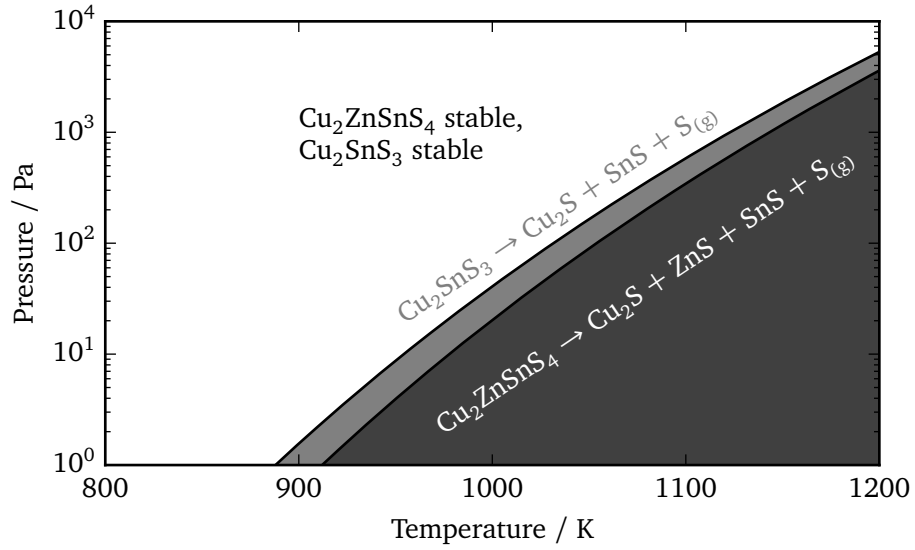

Figure 8.12 – Temperature-dependent phase stability of kesterite Cu_2ZnSnS_4 and monoclinic Cu_2SnS_3 with respect to binary phases and sulfur vapour. The solid lines indicate $\Delta G = 0$ for the reactions indicated on the plot; the ternary decomposition is favourable over the entire shaded area, while the quaternary decomposition is only favourable in the darker shaded area.

The main observation of note is that the stability envelopes for kesterite CZTS and Cu_2SnS_3 are very close. At high temperature and low pressure, both phases can decompose to binary phases and sulfur vapour. However, they do not do this at exactly the same point, and interactive manipulation of the temperature and pressure of the model phase diagrams revealed "sweet spot" conditions in which no ternary phases appear on pseudo-ternary phase diagram, but the quaternary phase remains (Fig. 8.10). By plotting the stability line ($\Delta G = 0$) of each of these decomposition processes, we see that for a given pressure there is a narrow temperature window in which the ternary phases might be eliminated simply by annealing (Fig. 8.12).

8.4 Conclusions

Information about the relative stability of phases in the Cu-Zn-Sn-S system has been computed and studied as a function of temperature and pressure. Both CZTS and Cu_2SnS_3 are found to decompose to form binary compounds when the system is under elevated temperatures and reduced pressures. However, the system is stable both at moderate vacuum annealing conditions ($T = 850\,\mathrm{K}, p_S = 10\,\mathrm{Pa}$) and at the intense conditions associated with formation in a sealed vessel ($T = 1200\,\mathrm{K}, p_S = 10^7\,\mathrm{Pa}$), with the main difference being the oxidation state of any tin sulfide. A "sweet spot" stability envelope has been identified in which ternary phases are unstable but kesterite CZTS is stable; in principle this could be used to form ternary-free CZTS by annealing under these conditions and then quenching the system. The resulting CZTS would be likely to include substantial cation disorder. However, this window is very narrow with a width of around 10 K and a strong pressure-dependence.

CZTS is typically produced with non-ideal stoichiometry in Cu-poor conditions. On the phase diagrams produced, the expected secondary phases corresponding to this stoichiometry are ZnS in the zinc blende phase and either SnS (at low p_S) or SnS_2 (at high p_S).

Bibliography

[1] A. J. Jackson and A. Walsh, *J. Mater. Chem. A*, 2014, **2**, 7829.

[2] O. Madelung, *Semiconductors: Data Handbook*, Springer-Verlag, Berlin, 3rd edn., 2004.

[3] A. Weber, R. Mainz, H. W. Schock and I. I. Experimental, *J. Appl. Phys.*, 2010, **107**, 013516.

[4] J. J. Scragg, T. Ericson, T. Kubart, M. Edoff and C. Platzer-Björkman, *Chem. Mater.*, 2011, **23**, 4625–4633.

[5] A. Redinger, D. M. Berg, P. J. Dale and S. Siebentritt, *J. Am. Chem. Soc.*, 2011, **133**, 3320–3.

[6] A. Jain, *Materials stability and Nature's bike shop*, `http://hackingmaterials.com/2014/05/08/pdcomic/`, 2014, [Accessed: 2015-09-03].

[7] M. Hillert, *Phase Equilibria, Phase Diagrams and Phase Transformations: Their Thermodynamic Basis*, Cambridge University Press, Cambridge, 2nd edn., 2008.

[8] J. W. Gibbs, *Trans. Conn. Acad.*, 1873, **2**, 309–342.

[9] L. A. Burton and A. Walsh, *J. Phys. Chem. C*, 2012, **116**, 24262–24267.

[10] G. Hautier, S. P. Ong, A. Jain, C. J. Moore and G. Ceder, *Phys. Rev. B*, 2012, **85**, 155208.

[11] I. Olekseyuk, I. Dudchak and L. Piskach, *J. Alloys Compd.*, 2004, **368**, 135–143.

[12] S. P. Ong, W. D. Richards, A. Jain, G. Hautier, M. Kocher, S. Cholia, D. Gunter, V. L. Chevrier, K. A. Persson and G. Ceder, *Comput. Mater. Sci.*, 2013, **68**, 314–319.

[13] *Qhull*, 2012, `http://www.qhull.org`, [Online; accessed 2015-09-18].

[14] *SciPy: Open source scientific tools for Python*, 2001, `http://www.scipy.org`, [Online; accessed 2015-03-06].

[15] C. B. Barber, D. P. Dobkin and H. Huhdanpaa, *ACM Trans. Math. Softw.*, 1996, **22**, 469–483.

[16] J. D. Hunter, *Comput. Sci. Eng.*, 2007, **9**, 90–95.

[17] *pycalphad*, 2015, `https://github.com/richardotis/pycalphad`, [Online; accessed 2015-09-03].

[18] D. M. Berg and P. J. Dale, in *Copper zinc tin sulphide-based thin film solar cells*, ed. K. Ito, John Wiley & Sons, Chichester, UK, 2015, ch. 5, pp. 107–132.

[19] V. Piacente, S. Foglia and P. Scardala, *J. Alloys Compd.*, 1991, **177**, 17–30.

Closing remarks

The main focus of this work has been to examine the effect of temperature and pressure on the Cu-Zn-Sn-S system. While progress has been made in the last few years towards identifying and manipulating secondary phases, the pressure of annealing systems remains poorly-characterised. While many researchers are carrying out high-pressure synthesis of CZTS and CTS phases in sealed ampoules, the reports in the literature tend to specify only the quantity of elemental sulfur added to the vessel and the target temperature. The model of sulfur vapours in Chapter 6 shows that the composition of this phase is closely related to the system pressure at typical annealing temperatures, and so the pressure cannot be estimated by simple ideal-gas assumptions. In low-pressure experiments, the substrate typically sits in a graphite box with a sufur source and a lid. The pressure, and hence chemical potential, of sulfur which the substrate is exposed to is determined by the dynamics of this system, which may include sulfur venting through a small hole or by lifting the lid of the graphite box. It is likely that both of these systems can be modelled and understood better, but such a model would require some kind of direct experimental verification. **For accurate control of the system thermodynamics, it must be possible to measure and manipulate the pressure of sulfur vapours.**

Non-stoichiometry and defects in the system play a major role in device performance. The motive of the work in this thesis was the impact of secondary phases on performance, and while this remains a concern the evidence base has grown in the last few years for local inhomogeneities being a major contributor to the V_{OC} deficit. The methodology developed in this work has been focused on pure, ideal phases. It would be possible to extend and adapt this approach to consider parameterised changes in properties as a function of composition; this is done routinely with experimental data in the CALPHAD ("calculation of phase diagrams") field. The use of on-lattice models is likely to be productive in the development of large characteristic supercells, such that the concentration-dependence of defect properties can be explored. **It will be helpful to bring together data from different sources without upsetting the cancellation of errors in *ab initio* calculations.**

With a few caveats, *ab initio* studies are deterministic and it is not necessary to repeat computations. The recent growth in materials databases has the potential to save a lot of computer time (and hence energy), but requires standardisation in methodology. **The analysis programs and key data from this work are made publicly available as Free Software,** but this does not in itself make the model easily accessible.

The depth and breadth of this study was designed in order to make useful predictions with the computational resources available. As greater resources become available, it will be feasible to go beyond the harmonic approximation, and incorporate more elements (e.g. Se, Ge, Ag) into such work. While the work here has largely avoided reliance on calorimetry experiments, it has remained dependent on crystallography. **It is difficult to make progress in the theoretical study of Cu–Sn–S phases when those phases are poorly defined.** Global optimisation methods, such as the evolutionary algorithm used to find sulfur clusters, could play an important role in the more general future of multi-component *ab initio* thermodynamics.